# Chapter 3

# Observational Program: Phase I

The first phase of the observing program was begun in 1996 by Prof. Janes, prior to the Lowell Observatory partnership that allowed Boston University access to the Perkins Telescope. The initial portion of the program was intended to explore what photometric precision was possible, what observing techniques would be needed, and what problems would need to be addressed. Here I will discuss this portion of the program and give some preliminary results.

## 3.1 Observing Program

The observational portion of this thesis was a team effort, involving several people over the course of the project (see acknowledgments). The observations have been taken on two telescopes: the 1.0 m telescope at the Mt. Laguna Observatory (MLO), and the 1.8 m Perkins Telescope at Lowell Observatory. The MLO data were taken in many observing runs between August 1996 and September 1999. The Perkins telescope data were taken between August 1998 and July 2002. The observing runs are summarized in Table 3.1.

| Telescope | Dates (UT) | CCD | Usable Nights | Objects | Filters |
|---|---|---|---|---|---|
| MLO | 1996 Aug 18-24 | Loral | 7 | 1, 2, 4 | BVI |
| MLO | 1996 Oct 8-13 | Loral | 6 | 1, 2, 3, 4 | BVI |
| MLO | 1997 Jan 29 - Feb 2 | Loral | 4 | 3, 4 | V |
| MLO | 1997 Sep 27-30 | Loral | 4 | 1, 2, 4 | UBV |
| MLO | 1997 Oct 29-30 | Loral | 2 | 1 | BV |
| MLO | 1998 Jan 22 | Loral | 1 | 3, 4 | V |
| MLO | 1998 Feb 6 | Loral | 1 | 3 | V |
| MLO | 1998 Jul 24-31 | Loral | 6 | 1, 2, 4 | BVI |
| Perkins | 1998 Aug 3-6 | SITe | 4 | 1, 2 | BV |
| MLO | 1998 Sep 11-14 | Loral | 4 | 1, 2 | V |
| Perkins | 1998 Sep 12-15 | SITe | 2 | 1, 2 | UV |
| MLO | 1998 Oct 13-15 | Loral | 3 | 1, 2, 3, 4 | VR |
| Perkins | 1998 Oct 16-21 | SITe | 6 | 1, 2, 3, 4 | UVR |
| Perkins(Q) | 1998 Oct 29 | SITe | 1 | 1, 4 | V |
| MLO | 1998 Nov 18 | Loral | 1 | 1 | V |
| Perkins(Q) | 1998 Nov 21-23 | Navy | 2 | 1, 2, 3, 4 | VI |
| Perkins(Q) | 1998 Nov 28 | Navy | 1 | 4 | V |
| Perkins(Q) | 1998 Dec 1-7 | Navy | 4 | 1, 3, 4 | V |
| Perkins(Q) | 1999 Jan 5-6 | SITe | 1 | 1, 3, 4 | V |
| Perkins(Q) | 1999 Jan 11 | SITe | 1 | 3, 4 | V |
| Perkins(Q) | 1999 Feb 23 | SITe | 1 | 3, 4 | V |
| Perkins | 1999 Mar 5-10 | SITe | 5 | 3 | V |
| Perkins(Q) | 1999 Mar 30 | SITe | 1 | 3 | V |
| Perkins | 1999 May 17-24 | SITe | 4 | 2 | VRI |
| Perkins(Q) | 1999 Jun 1-3 | SITe | 2 | 2 | V |
| Perkins(Q) | 1999 Jun 24-25 | SITe | 1 | 2 | V |
| Perkins(Q) | 1999 Jul 2-4 | SITe | 2 | 2 | V |
| Perkins | 1999 Jul 13-20 | SITe | 0 | | |
| Perkins(Q) | 1999 Aug 1-2 | SITe | 1 | 1, 2 | V |
| Perkins(Q) | 1999 Aug 26-27 | SITe | 2 | 1, 2, 4 | V |
| Perkins(Q) | 1999 Sep 3 | SITe | 1 | 1, 2, 4 | V |
| Perkins | 1999 Sep 8-14 | SITe | 4 | 1, 2, 4 | V |
| MLO | 1999 Sep 12-15 | Loral | 3 | 1, 2, 4 | VI |
| Perkins(Q) | 1999 Sep 30 | SITe | 1 | 1, 2, 4 | V |
| Perkins | 1999 Oct 11-15 | SITe | 5 | 1, 2, 3, 4 | UBVRI |
| Perkins(Q) | 1999 Oct 21 | SITe | 1 | 1, 2, 3, 4 | V |
| Perkins(Q) | 1999 Oct 29 | SITe | 1 | 1, 2, 3, 4 | V |
| Perkins | 1999 Nov 3-5 | Navy | 1 | 1, 2, 4 | V |
| Perkins | 1999 Nov 11-15 | SITe | 5 | 1, 2, 3, 4 | VI |
| Perkins(Q) | 1999 Nov 21 | SITe | 1 | 1, 3 | V |
| Perkins(Q) | 1999 Dec 1 | SITe | 1 | 3, 4 | V |

Table 3.1: Phase I Observations. "MLO" refers to the 1.0-m Mt. Laguna Observatory telescope. "Perkins" refers to the 1.8-m Perkins Telescope at Lowell Observatory. A Q after the telescope name denotes observations made by the BU Queue observer, as explained in the text. The CCD designations "Loral", "SITe", "Navy", "Loral1", and "Loral2" are explained in the text. The clusters are assigned numbers in order of age: 1 – NGC 7789, 2 – NGC 6819, 3 – M67, 4 – NGC 188. Table is continued on the next page.

| Telescope | Dates (UT) | CCD | Usable Nights | Objects | Filters |
|---|---|---|---|---|---|
| Perkins | 2000 Jan 11-16 | SITe | 6 | 1, 3, 4 | VI |
| Perkins(Q) | 2000 Feb 6 | Navy | 1 | 3 | V |
| Perkins(Q) | 2000 Feb 26 | Navy | 1 | 3 | V |
| Perkins | 2000 Apr 16-25 | Loral1 | 0 | | |
| Perkins(Q) | 2000 May 3 | Loral1 | 1 | 2, 3 | V |
| Perkins(Q) | 2000 May 25-26 | Loral1 | 0 | | |
| Perkins | 2000 Jun 27 - Jul 3 | Loral1 | 1 | 2 | BVI |
| Perkins(Q) | 2000 Jul 11 | Loral1 | 1 | 1, 2 | V |
| Perkins(Q) | 2000 Jul 18 | Loral1 | 1 | 1, 2 | V |
| Perkins(Q) | 2000 Jul 24 | Loral1 | 1 | 2 | V |
| Perkins | 2000 Aug 2-9 | Loral1 | 1 | 1 | BVR |
| Perkins(Q) | 2000 Aug 26 | Loral1 | 1 | 1 | V |
| Perkins(Q) | 2000 Sep 5 | Loral1 | 1 | 1 | V |
| Perkins(Q) | 2000 Sep 12 | Loral1 | 1 | 1, 2, 4 | VI |
| Perkins | 2000 Sep 19-26 | Loral1 | 5 | 1, 2, 4 | UV |
| Perkins(Q) | 2000 Oct 3 | Loral1 | 1 | 1, 4 | V |
| Perkins(Q) | 2000 Oct 12 | Loral1 | 1 | 1, 2 | V |
| Perkins | 2000 Oct 25-30 | Loral1 | 2 | 1, 2, 3, 4 | VR |
| Perkins(Q) | 2000 Nov 9 | Loral1 | 1 | 1, 4 | V |
| Perkins(Q) | 2000 Nov 16-19 | SITe | 3 | 1, 2, 3, 4 | V |
| Perkins(Q) | 2000 Dec 15 | SITe | 1 | 1 | V |
| Perkins(Q) | 2001 Jan 21 | Navy | 1 | 1, 3, 4 | V |
| Perkins(Q) | 2001 Jan 26 | Navy | 1 | 1, 3, 4 | V |
| Perkins(Q) | 2001 Jan 31 | Navy | 1 | 1, 3, 4 | V |
| Perkins(Q) | 2001 Feb 13 | SITe | 1 | 3, 4 | V |
| Perkins | 2001 Feb 24 | Navy | 1 | 3 | VRI |
| Perkins(Q) | 2001 Mar 13 | Loral1 | 1 | 3 | V |
| Perkins(Q) | 2001 Apr 2 | SITe | 1 | 3 | V |
| Perkins(Q) | 2001 Apr 9 | SITe | 1 | 3 | V |
| Perkins(Q) | 2001 Apr 30 | Loral2 | 1 | 2, 3 | V |
| Perkins | 2001 May 23-29 | Loral2 | 2 | 2, 3 | UVI |
| Perkins | 2001 Jul 14-20 | Loral2 | 7 | 1, 2 | UBVRI |
| Perkins(Q) | 2001 Jul 28 | Loral2 | 1 | 1, 2 | VI |
| Perkins | 2001 Aug 22-28 | Loral2 | 7 | 1, 2, 4 | UBV |
| Perkins(Q) | 2001 Sep 11-12 | Loral2 | 2 | 1, 2, 4 | VI |
| Perkins(Q) | 2001 Sep 21 | Loral2 | 1 | 1, 2 | VI |
| Perkins(Q) | 2001 Sep 27 | Loral2 | 1 | 1, 2 | VI |
| Perkins | 2001 Oct 11-16 | Loral2 | 5 | 1, 2, 3, 4 | UBVI |
| Perkins | 2001 Dec 16-22 | Loral2, Navy | 4 | 1, 3, 4 | BVR |
| Perkins | 2002 Feb 15-19 | Loral2 | 3 | 3 | BVR |
| Perkins | 2002 Mar 15-21 | Loral2 | 4 | 3 | BVR |

Table 3.2: Phase I Observations, continued.

### 3.1.1 Mt. Laguna Observatory Observations

The Mt. Laguna Observatory 1.0-m reflecting telescope, jointly operated by San Diego State University and the University of Illinois at Urbana-Champaign, was used during the first phase of observations. The telescope was used with a $2048 \times 2048$ pixel Loral CCD at the f/7.6 Cassegrain focus. (This CCD is designated "Loral" Table 3.1.) The Loral CCD has $15\mu \times 15\mu$ pixels which gives an image scale of $0.41''$ pix$^{-1}$, resulting in a field of view of $14' \times 14'$. The CCD's read noise is 8.5 e$^-$ and gain is 3.185 e$^-$ ADU$^{-1}$. A UBVRI filter set designed to approximate the Johnson/Kron-Cousins UBVRI passbands, given the telescope and CCD response, was used for all the MLO observing.

No unusual procedures were used, except that additional telescope guiding was done by hand. Standard stars were observed when the sky was photometric and as time allowed. Dome flat fields and sky flat fields were both taken through the appropriate filters for each observing run. As many flat fields were taken as possible, although the long read out time of the CCD allowed only 5 - 10 each night. The exposure times for cluster observations depended on the seeing conditions and filter employed Typical the exposure times were 30 s - 3 min, with the B filter requiring longer exposures and the I shorter.

### 3.1.2 Perkins Telescope Observations

Boston University joined in a partnership with Lowell Observatory to use and maintain the 1.8-m Perkins Telescope in 1998. The Perkins Telescope was used with four different CCDs placed at the f/17.5 Cassegrain focus. Several different observing strategies were experimented with while using this telescope.

As at Mt. Laguna Observatory, the exposure times depended on the seeing conditions and the filter employed, but we had the additional factor of different pixel fields of view on the various CCDs (described below). The goal was to expose for as long as possible without saturating too many stars. Typically the exposure times were 1 - 3 min, with the B filter requiring somewhat longer exposures and the I somewhat shorter.

### CCDs

The SITe CCD is a 2048 $pix \times 2048$ $pix$ CCD, with pixels $24\mu$ on each side. The pixel scale is $0.15''$ pix$^{-1}$, giving a $5.12' \times 5.12'$ field of view. The SITe CCD's read noise is 10.5 e$^-$ and its gain is 3.87 e$^-$ ADU$^{-1}$. This CCD was binned $2 \times 2$ on-chip in order to lower the read out time. It is designated "SITe" in Table 3.1.

The USNO 4:1 CCD is a 800 $pix \times 800$ $pix$ CCD, with $15\mu$ pixels. It has a field of view of $5.7' \times 5.7'$, giving $0.43''$ pix$^{-1}$. This CCD's read noise is 11.9 e$^-$ and its gain is 1.53 e$^-$ ADU$^{-1}$. This CCD has substantial vignetting and numerous cosmetic defects, so we did not use it often. This CCD is referred to as "Navy" in Table 3.1.

Two Loral CCDs were used at the Perkins Telescope, which are mechanically identical; they differ only in read noise, gain, and cosmetic defects. Each Loral CCD was 2048 $pix \times$ 2048 $pix$ with $15\mu$ pixels. The pixel scale was $0.094''$ pix$^{-1}$, which resulted in a $3.2' \times 3.2'$ field of view. Both CCDs were binned $2 \times 2$ on-chip during our observations. The first Loral CCD ("Loral1" in Table 3.1) was used from approximately April 2000 to April 2001; it has a read noise of 15.0 e$^-$ and a gain of 5.5 e$^-$ ADU$^{-1}$. The second Loral CCD ("Loral2" in Table 3.1) was used from April 2001 to the present; it has a read noise of 17.0 e$^-$ and a gain of 3.1 e$^-$ ADU$^{-1}$.

### Observing Strategies

The initial observing strategy at the Perkins Telescope was essentially the same as used on the MLO telescope. The object was roughly centered on the CCD, and an auto-guider was used to track a guide star. UBVRI filters approximating the Johnson/Kron-Cousins passbands were employed, usually one per night. Dome flats and 15 - 20 sky flat fields were taken through the same filter each night. Standard star observations were taken when the sky was photometric. This strategy was used for the observing runs from August 1998 through October 1999, with the exception of the May 1999 observing run.

In September 1999, telescope time was granted on the same nights on the MLO tele-

scope, the Perkins telescope, and the 1.2-m Hall Telescope (also at Lowell Observatory). The hope was that virtually simultaneous observations of the same objects would prove useful. However, the weather was uncooperative so only one night was clear at all three telescopes. The observations on this night were performed in the same manner as discussed previously.

Beginning with the May 1999 observing run, and then continuing from November 1999 to October 2001, a new strategy was employed. Once an object was placed in the CCD's field of view, multiple exposures would be taken, each through a different filter. Filter pairs or triplets, such as VI, BVR, VR, BV, BVI, and UVI, were used. Once the sequence had been taken, the telescope would be moved slightly ($6 - 18''$), and then the sequence of exposures would be taken again. Initially, the dithering sequence covered a large grid with some twenty-five positions before a position was repeated; however, this pattern generally took too long to complete. It was scaled down to a five-position "plus" pattern. In all cases, the auto-guider was still used, and standard star measurements were taken in good sky conditions.

Starting in December 2001 and continuing to the present, dithering was discontinued. Instead, an attempt was made to place the same stars on the same pixels of the CCD each night. Exposures were cycled through the BVR filters. Additionally, the telescope was de-focused for our observations of M67 in February and March 2002 in order to increase the number of photons received per image.

### 3.1.3 BU Queue

When Boston University and Lowell Observatory became partners using the Perkins Telescope, the BU Queue program was created. Astronomers at BU and Lowell Observatory who wished semi-regular, usually weekly, observations of certain objects can submit those objects to the Queue, along with appropriate exposure times and filters. Astronomers with objects in the Queue took turns observing on the BU Queue nights. (BU Queue

nights are indicated with a "Q" in Table 3.1.)

The appropriate calibration images, such as bias images and flat fields were also taken, although most Queue objects were observed only through the V filter. Usually only dome flats were taken, which means that the large scale illumination pattern (see below) could not be corrected. Also, short integration flats could not be taken, which prevented the creation of a shutter correction image (see below).

## 3.2 Reduction Process

The data reduction process consists of five main steps:

1. Image processing using IRAF[1].
2. Photometry performed by *SPS*.
3. Coordinate-matching using *astrometry*.
4. Mapping zero point changes across the CCD using *magmap*.
5. Ensemble photometry and bookkeeping performed by *diffmag*.

Many of these programs were written by K. Janes. Stellar Photometry Software (SPS) is documented in Janes & Heasley (1993). The others written by him are *astrometry*, *magmap*, and *diffmag*. I performed the majority of the data reductions using these programs.

### 3.2.1 Basic Data Reduction Using IRAF

The package *noao.imred.ccdred* in IRAF is used to perform basic calibrations, such as overscan subtraction, bias corrections and flat field corrections. The non-standard calibration is the shutter correction, which will be discussed below.

[1]IRAF is distributed by the National Optical Astronomy Observatories, which are operated by the Association of Universities for Research in Astronomy, Inc., under cooperative agreement with the National Science Foundation.

### Overscan, Trim, and Bias

The task *noao.imred.ccdred.ccdproc* is used to subtract the mean of each row of the overscan section from the rest of the image. This task also trims the image to the specified dimensions and subtracts off the bias pattern image. The bias pattern image is created by finding the median pixel of each pixel in a set of bias images taken either that night or over the entire observing run. No dark current correction was made because all the exposures for this program were short.

### SITe/Loral Shutter Correction

The SITe and Loral CCDs as used on the Perkins telescope have a very slow shutter. (The Navy CCD uses a different shutter and does not suffer from this problem.) On short exposures, the six-petal shutter can be seen blocking some of the incoming light from the CCD; an image of the shutter pattern can be seen in Figure 3.1. On a one-second V sky flat, the most obscured part of the CCD has only 96% as many ADUs as the center of the chip. However, regardless of the length of the exposure, the shutter blocks a certain amount of light from the CCD. The overall effect is that of altering the exposure time as a function of position on the image.

I devised a method for creating a shutter correction image and applying it via IRAF to a list of images. The shutter correction image is created by comparing long integration flats to short integration flats of the same filter. A "long integration" flat should be thirty seconds or longer. An image I call the Long Flat is created by combining as many long integration flats from an observing run as is practical. If enough long integration flats exist, taking the median of them is best; if there are few, then averaging is necessary.

The Long Flat is used to flat field all "short integration" flats; that is, those flats that are two seconds or shorter, taken through the same filter. The "processed" short flats, which I will call Interim Images, should clearly show the shutter pattern. Five or six Interim Images is typical with the SITe CCD, but with the Loral's faster readout time, it

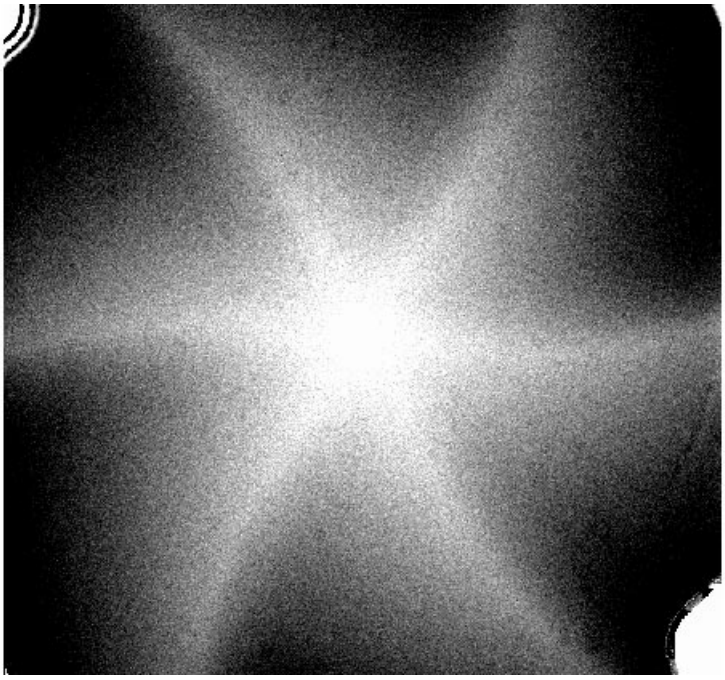

Figure 3.1: An image of the shutter pattern on the SITe and Loral CCDs. The six leaves of the shutter are clearly visible. The bright spots in the upper left and lower right corners are tips of the shutter which do not fully retract and whose images are not removed by calibrations.

is possible to take more short integration flats and thus get more Interim Images.

To use these Interim Images to create a shutter correction, the number of ADUs in the center pixel of the Interim Image is found. A shutter correction image can then be made from each of the Interim Images with the following recipe (image variables are indicated with an accent):

$$\hat{S} = \frac{M - \hat{I}_{flat}}{M} \cdot T, \tag{3.1}$$

where M is the number of ADUs in the center of the Interim Image, $\hat{I}_{flat}$ is the Interim Image, and T is the exposure time of the short integration flat that was made into the Interim Image. $\hat{S}$ is then the shutter correction. This formula scales the "picture" of the shutter according to both the intensity of the Interim Image and the exposure time of the Interim Image.

Once a shutter correction has been made from each of the Interim Images, all of the shutter correction images should be averaged to make a master shutter correction. This master shutter correction should be tested on a few of the (unflatted) short integration flats to check for any errors in the above procedure. Some brief testing has demonstrated that the master shutter correction is independent of filter. However, due to the flat fielding part of the above process, Interim Images and shutter correction images should be created separately for each filter, and then all filters' shutter correction images can be averaged to make the master shutter correction. The shutter pattern also does not seem to change over time, at least on time scales of a few months. However, it is recommended that a master shutter correction image be made for each observing run.

Once the master shutter correction has been made, each image (including the flat fields) can be corrected with the following formula:

$$\hat{I}_{true} = \frac{\hat{I}_{obs}}{T - \hat{S}} \cdot T \tag{3.2}$$

In this case, $\hat{S}$ is the master shutter correction image, $\hat{I}_{obs}$ is the observed image, and $\hat{I}_{true}$ is the corrected image. A longer image will obviously be less affected by the slow shutter, and so longer images have a smaller correction.

Once the master shutter correction image is made, correcting the individual images of the run becomes routine. I have written an IRAF procedure which has been used to correct all of our images.

### Flat Fielding

During each observing run with the MLO telescope, both dome and sky flat fields were usually taken. These were used to make a flat field correction image and an illumination correction image. All the dome flats taken through the same filter were combined into a "master" dome flat. This master dome flat was used as the flat field correction in the *noao.imred.ccdred.ccdproc* task. An example of an MLO V flat is Figure 3.2.

The illumination correction image was created using the sky flat fields. First all of the

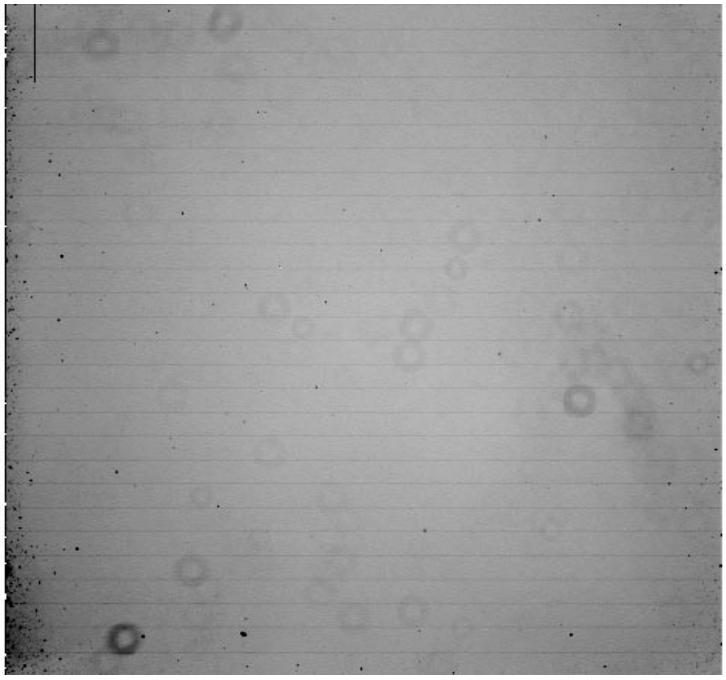

Figure 3.2: A sample MLO flat field, taken through the V filter on UT 1999 Sep 12. The image is scaled from 9260 to 12848 ADUs.

sky flats taken through one filter were combined. This combined imaged was flat field corrected by the master dome flat, then heavily smoothed via *images.imfilter.boxcar* in order to eliminate any small-scale variations. The illumination correction image was created by using the *noao.imred.ccdred.mkillumcor* routine on the smoothed image, specifying a box size of zero.

At the Perkins Telescope, faster read out times of all of the CCDs allowed many more flat fields to be exposed than at MLO. Since the sky flats contain both the pixel-to-pixel variations as well as the large scale illumination pattern, dome flats were usually not necessary. All of the sky flat fields taken through one filter were combined; the sky flats from one night or the entire observing run were combined depending on whether or not there were any night-to-night changes in the CCD setup. The combined image was applied via *ccdred.ccdproc* as the flat field correction. Sample flat fields for the SITe CCD, the Navy CCD, and the first and second Loral CCDs may be seen in Figures 3.3, 3.4, 3.5, and

3.6, respectively.

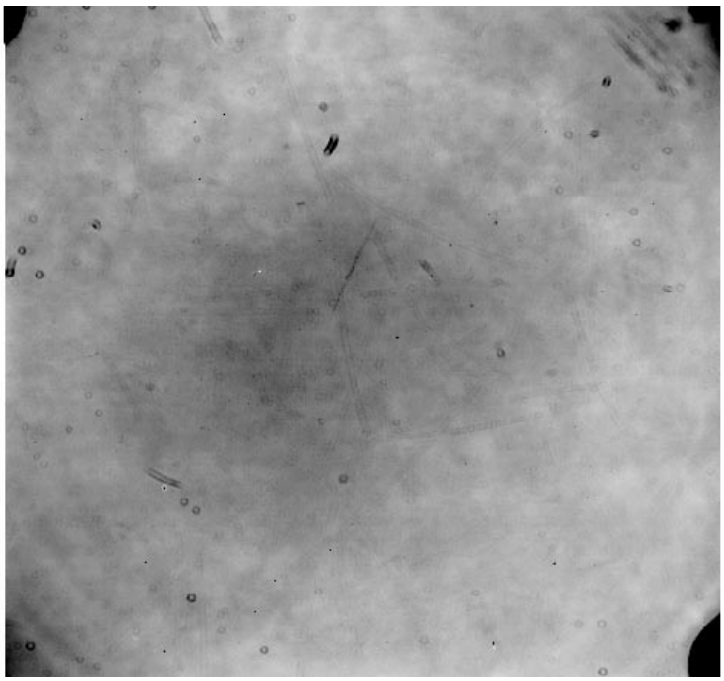

Figure 3.3: A sample Perkins Telescope SITe CCD flat field, taken through the V filter on UT 1999 Sep 12. The image is scaled from 12149 to 15038 ADUs.

### 3.2.2 SPS Photometry

The program Stellar Photometry Software (Janes & Heasley 1993) is used to perform photometry on the images. SPS performs both aperture and PSF-fitting photometry, and once initial parameters are set, it may be run in batch mode.

#### Initial Parameters

First, SPS needs basic information about the CCD and image characteristics. This information includes the gain, read noise, and saturation level of the CCD and the estimated FWHM of the stellar images. SPS also requires the estimated Poisson error due to the sky background and the estimated error contributed due to the flat field correction.

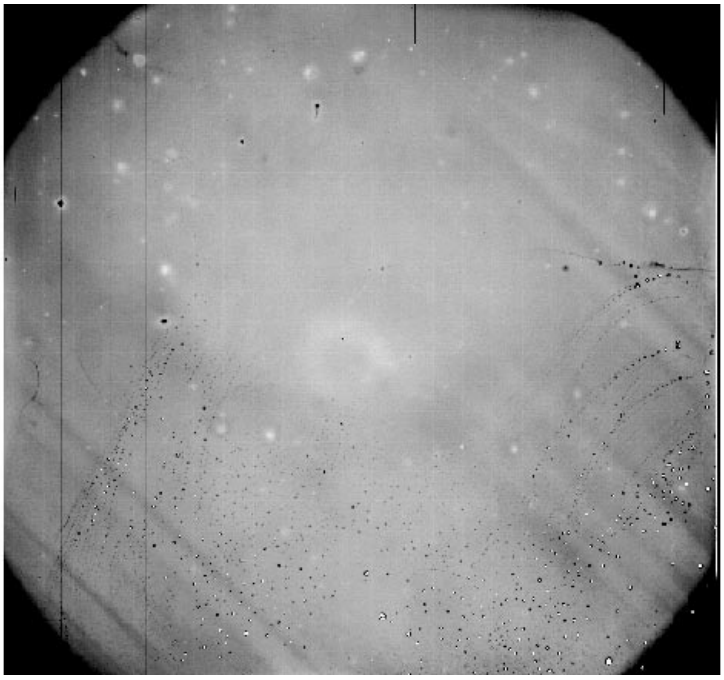

Figure 3.4: A sample Perkins Telescope Navy CCD flat field, taken through the V filter on UT 1998 Nov 22. The image is scaled from 4051 to 7048 ADUs. The white spots are variations in chip sensitivity, not star images.

Finally, the program needs to be told parameters about how to perform the photometry. The PSF diameter is specified: this tells SPS how "big" a PSF to store, in pixels; generally this is chosen to be about four times the FWHM of the stars in the image. The PSF fitting radius chooses how far from the star's center the PSF will be fit; this is usually about the same as the star's FWHM.

The aperture photometry parameters must also be entered. The aperture photometry radius is chosen to be large enough so that only an insignificant proportion of the starlight will fall outside the aperture; this is taken typically to be three times the FWHM. The outer sky radius is used to set the outer edge of the annulus used to determine the sky background value – this value is generally set to be as large as possible, 40 or more pixels. The aperture fitting radius specifies the radius used for aperture photometry. SPS uses the calculated PSF to derive aperture corrections to tie the magnitudes from the PSF or

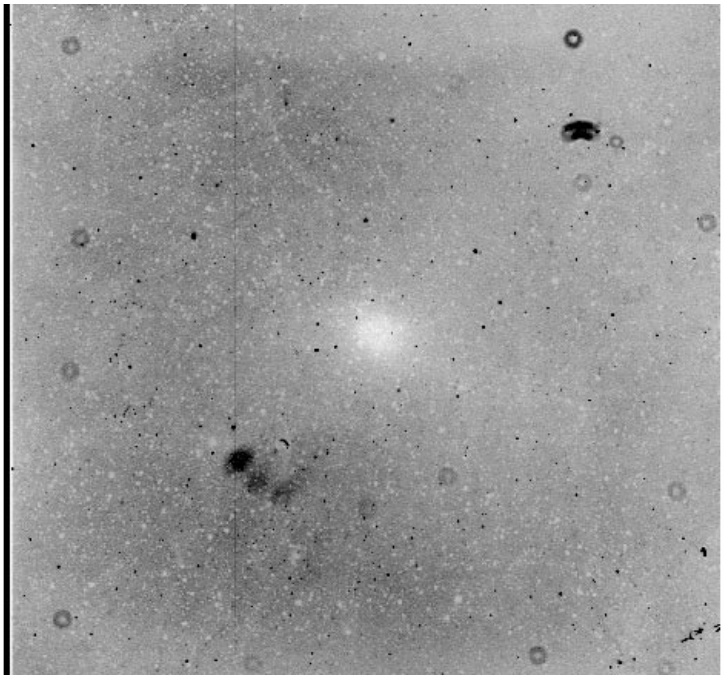

Figure 3.5: A sample Perkins Telescope Loral1 CCD flat field, taken through the V filter on UT 2000 Aug 9. The image is scaled from 1357 to 2250 ADUs.

aperture fitting radii to the same scale as those from the reference radii.

SPS can also bin the images prior to performing photometry. All parameters are entered in their *unbinned* amounts; SPS will bin the parameters accordingly. Table 3.3 lists the parameters generally used for each of the CCDs.

### Photometry Procedure

A routine has been created for performing the photometry, since SPS can do so in a batch process. The general steps are:

1. Find stars in the image.
2. Make the initial PSF.
3. Perform PSF-fitting photometry on all stars.
4. Re-make the PSF.

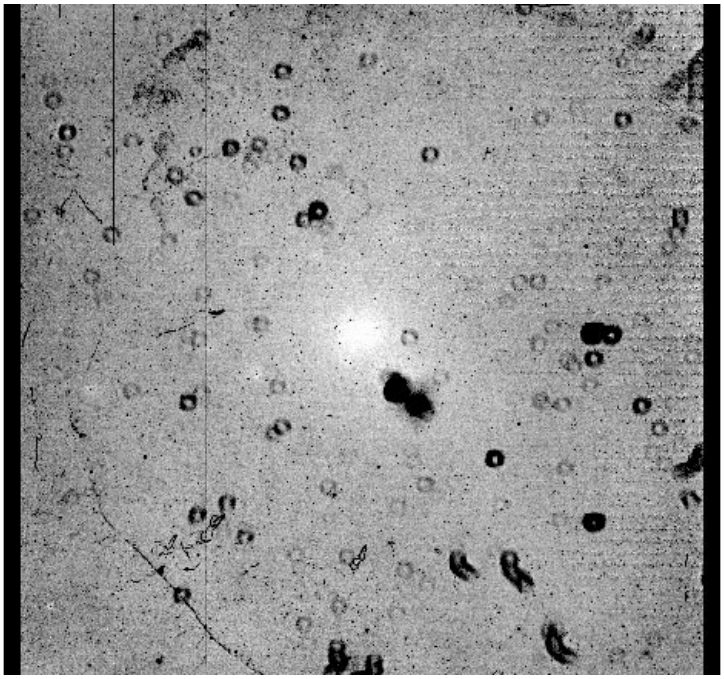

Figure 3.6: A sample Perkins Telescope Loral2 CCD flat field, taken through the V filter on UT 2002 Mar. The image is scaled from 7034 to 7545 ADUs.

| Parameter | Loral | SITe | Navy | Loral1 | Loral2 |
|---|---|---|---|---|---|
| Gain ($e^-$ $ADU^{-1}$) | 3.10 | 3.87 | 1.53 | 5.50 | 3.10 |
| Read noise ($e^-$) | 8.0 | 10.5 | 11.9 | 15.0 | 17.0 |
| Saturation level (ADUs) | 18000.0 | 40000.0 | 13000.0 | 45000.0 | 26000.0 |
| Estimated sky error (ADUs) | 1.0 | 1.0 | 1.0 | 1.0 | 1.0 |
| % flat field error | 0.01 | 0.01 | 0.01 | 0.01 | 0.01 |
| Estimated stellar FWHM (pix) | 6.00 | 8.00 | 4.00 | 10.00 | 10.00 |
| PSF diameter (pix) | 46.00 | 46.00 | 23.00 | 48.00 | 48.00 |
| PSF fitting radius (pix) | 6.00 | 8.00 | 4.00 | 10.0 | 10.0 |
| Aperture photometry radius (pix) | 18.00 | 18.00 | 9.00 | 18.00 | 18.00 |
| Outer sky radius (pix) | 80.00 | 80.00 | 40.00 | 80.00 | 80.00 |
| Aperture fitting radius (pix) | 8.00 | 10.0 | 4.00 | 10.0 | 10.0 |
| Binning | $2 \times 2$ | $2 \times 2$ | none | $2 \times 2$ | $2 \times 2$ |
| Pixel Scale ($''$ $pix^{-1}$) | 0.41 | 0.15 | 0.43 | 0.09 | 0.09 |

Table 3.3: SPS parameters for each CCD. CCDs are designated as in Table 3.1.

5. Look for new stars and perform PSF-fitting photometry on them.

6. Subtract all stars from the frame and fit the sky background.

7. Perform PSF-fitting photometry on all stars.

8. Re-make the PSF.

9. Perform PSF-fitting photometry on all stars.

10. Perform aperture photometry.

As listed above, the first step is to find the stars in the image. Since no PSF has been created, a Gaussian PSF with the FWHM specified in the starting parameters is used. The star-finding procedure calculates the cross-correlation between the PSF and the image for each position in the image. The cross-correlation radius can be adjusted; we typically use a value that is about half the FWHM. The positions with high cross-correlation coefficients are likely star locations.

Next, the PSF is created. SPS performs aperture photometry on the brighter stars, and flags the stars with PSFs similar to the Gaussian. For a rich cluster such as NGC 7789, several hundred stars may be flagged. For a sparse, bright cluster such as M67, nearly all of the stars may be flagged, which is a few dozen.

Once the first-cut of stars for the PSF have been marked, a Gaussian is iteratively fit to the stars' radial brightness profiles. Stars which deviate from the profile more than a pre-set amount are removed from the PSF list. Once fitting has been completed, the non-Gaussian parts of the PSF are stored in a table of residuals. SPS is instructed to discard the PSF stars whose PSF and aperture magnitudes differ by more than a certain limit. Then the Gaussian is re-fit to the remaining stars and a new table of residuals is created. This is the first version of the PSF.

The first draft PSF is then fit to all stars, and preliminary PSF magnitudes are generated. The brightest stars are fit first, and then removed from the image so they do

not contaminate the fainter stars. The PSF is fit to the star images by a nonlinear least-squares fit that has been scaled and shifted to the star's brightness and position. If the removal of neighboring stars changes a star's magnitude significantly, it and all affected stars are re-fit. Consequently, several passes through the stars are made.

Now the PSF is re-made. The list of PSF stars is discarded and SPS searches again for PSF stars as previously, except that the radial profile of the stars must be similar to the radial profile of the first draft PSF and the error limit for acceptable stars is tightened. Still, several hundred stars will be chosen in rich clusters. Again, the PSF is modeled with a Gaussian and table of residuals, and stars deviating too strongly are discarded. The PSF is remade with the best stars.

Now the improved PSF is used to search for any stars that were not initially found. Then any stars that have physically impossible magnitudes or that seem to be duplicates of other stars are rejected. Then PSF photometry is performed on the new stars. This process is repeated a few times.

Once all stars have been found and have preliminary PSF magnitudes, SPS's "resky" routine is used. This routine removes all stars from the images, and then redetermines the sky background from the "empty" image. PSF photometry is then performed on all stars, utilizing the new determination of the sky background.

The PSF is then remade one last time. The old PSF star list is discarded, and new PSF stars are flagged. The PSF is fit, and unsuitable stars are discarded. Then the final PSF is fit. PSF photometry is performed on all stars. Bad stars or duplicate stars are discarded.

In the final portion of the routine, aperture photometry is performed. The reference aperture is used to tie the aperture photometry magnitudes and the PSF-fitting magnitudes to the same system. Using the star positions found during the PSF-fitting routine, the aperture photometry routine synthesizes an aperture around the star; the distance of each of the star's pixels from its center is computed and the stellar flux is summed

at each radius. Then the flux at the radius of the reference aperture is found by least-squares fitting to the adjacent radii in the synthetic aperture. The error in the flux is found by summing the individual pixel errors. The sky level is found from the mode of the distribution of pixel values around the star.

The radial profiles of the stars are used to create a mean radial profile. If any star deviates too strongly from the mean profile, it is removed and the profile is recalculated. The mean profile can be used to scale the magnitudes which were measured using smaller apertures in order to reduce the sky noise to the magnitude scale of the reference radius. This use of the mean profile assumes that the shapes of the stellar profiles are similar throughout the image. However, the calculated PSF itself (which may vary as a quadratic function across an image) is ordinarily used to calculate the stellar profile and to derive the aperture correction.

This whole procedure can be described in a script, which can be submitted to SPS along with a list of images to reduce. If the observing technique was altered (such as observing de-focused images) or a new CCD was used, some experimentation with SPS must be done to determine the optimal parameters. In batch mode, a rich field image can take several minutes to process.

SPS generates a number of output files for each image. The first is a log file, which gives information about the setup parameters given to SPS and about the PSF that was created. A second output file is the list of stars, their pixel coordinates, their PSF magnitudes, their aperture magnitudes, the errors in the magnitudes, the sky background value, and some program flags that indicate the number of neighbors around the star and how the photometry was performed. This output file is used in the next step of the data reduction process: coordinate transformation via *astrometry*. The last output file contains the PSF, so that SPS can be started again at a later date and the same PSF may be used.

### 3.2.3 Astrometric Transformation with *Astrometry*

In order to follow a star's brightness from frame to frame and night to night, each star must be identified on each frame. The program *astrometry* transforms the pixel coordinates of an image into a common coordinate system. *Astrometry*'s input is the list of coordinates and magnitudes output by SPS. A reference image is also specified in *astrometry*; this image sets the common coordinate system. The reference file is the same type of output file from SPS.

*Astrometry* determines the coordinate system transformation by searching for similar triangles in pixel distances between stars. Initial settings in the program tell it what types of triangles to use – the triangles are limited to a small range in shape to limit the range of search space. *Astrometry* also has settings for the maximum and minimum triangle side lengths. Once the program finds similar triangles in the reference image and target image, it checks the magnitudes of the stars involved. If the magnitudes differ by more than a pre-set amount, *astrometry* assumes that it has found similar triangles of different stars and discards the match.

Once *astrometry* finds enough similar triangle matches, the coordinate transformation is determined. Typically, 80 - 90% of the stars have matches between the reference and target images – the unmatched stars may be due to differences in integration times between the reference and target images or differences in the filter. The coordinate transformation includes translation of the coordinate system, stretching of the coordinate system (due to a different CCD pixel scale or different telescope), and rotation of the system. Quadratic terms may be included in the transformation as an option. The coordinate system transformation coefficients are appended to the target image's SPS log file. Then *astrometry* outputs a file of coordinates and magnitudes that is identical to SPS's output file, except that the x and y pixel coordinates are now in the reference coordinate system.

*Astrometry* can also be set to run in a batch mode. Generally, one reference image is chose to transform the coordinates of all the image of the same star cluster. The

list of images to be transformed is given to *astrometry*, which determines the coordinate transformation of each image in turn.

### 3.2.4 Photometric Transformation with *Magmap*

Each image is transformed independently to the standard photometric system as defined by stars in the same field using the program *magmap*. *Magmap* fits the zero point of the magnitude scale as well as a B-V color term. The user specifies whether the fitting is done on the entire image, or if the image should be broken into a grid for each section to be fit separately. A reference magnitude file with standard magnitudes for stars in the cluster through each filter is employed.

For this project, zero point differences only were calculated by least-squares fitting weighted by magnitude. Atmospheric extinction is corrected in this approach.

### 3.2.5 Ensemble Photometry with *Diffmag*

At this stage the data consist of files of magnitudes and positions of all measurable stars in the field, transformed to a common coordinate system and the standard magnitude system. The final step is to perform the ensemble differential photometry. We assume that the sum of the fluxes of a sufficiently large sample of stars in the field will be the same from image to image; any random fluctuations in brightnesses of individual stars in the ensemble should average out to zero. This approach was first employed by Gilliland & Brown (1988).

Each star is compared to an ensemble of neighboring stars whose flux is assumed to be constant. The stars forming the ensemble must satisfy the following conditions: they must be within 500 pixels of the target star; their brightness must be within three magnitudes of the target star; and they must be within 0.75 magnitudes of (B-V) color of the target star. The ensemble must consist of at least eleven stars, and the total flux of the ensemble stars must be at least three times that of the target star. The fluxes from stars brighter than

the target star are discounted to avoid domination by one or two bright stars; if the flux of a star is larger than that from the target star, then the bright star's flux is set equal to the target star. Once a satisfactory ensemble is created, the target star's magnitude change relative to the ensemble is calculated as well as the error in the magnitude difference. The zero point of the star's differential magnitudes is set such that the median differential magnitude is zero. This procedure is repeated for every star on every image.

The differential magnitude of the target star can be written as:

$$D(j,k,p) = m(j,k,p) - \overline{m}(p) - z(j,k,p), \tag{3.3}$$

where $D(j,k,p)$ is the magnitude of star $p$ compared to the ensemble magnitude on frame $j$ of night $k$; $m(j,k,p)$ is the measured magnitude in the standard photometric system of star $p$ on frame $j$ of night $k$; $\overline{m}(p)$ is the mean measured magnitude of star $p$ averaged over all frames; and $z(j,k,p)$ is the zero point measured magnitude of that region occupied by the ensemble on frame $j$ on night $k$ relative to all other frames. We can write $\overline{m}(p)$ exactly as:

$$\overline{m}(p) = \frac{1}{\sum_{k=1}^{N_p} N_{k,p}} \sum_{k=1}^{N_p} \sum_{j=1}^{N_{k,p}} m(j,k,p). \tag{3.4}$$

$N_{k,p}$ is the number of frames on night $k$ for star $p$, and $N_p$ is the number of nights where we observed star $p$.

In Equation 3.3, the zero point magnitude is determined by the ensemble stars, so we can write it as:

$$z(j,k,p) = \frac{1}{E_p} \sum_{e=1}^{E_p} (m(j,k,e) - \overline{m}(e)) \tag{3.5}$$

where $E_p$ is the number of stars in the ensemble for star $p$; $m(j,k,e)$ is the measured magnitude of ensemble star $e$ on frame $j$ of night $k$; $N_{k,e}$ is the number of frames of ensemble star $e$ on night $k$; and $N_e$ is the number of nights on which ensemble star $e$ was observed. The zero point is a function of the star $p$ because a separate ensemble is used for each star.

The result of the differential photometry program consists of three catalogs of differential magnitudes with entries for each star. The first is a catalog of differential magnitudes ($D(j,k,p)$ shown above) and magnitude errors calculated by *diffmag*, which incorporates the photometric errors calculated by SPS, for each star on every frame. The second catalog consists of the means and errors of the differential magnitudes for each night of observations. The last catalog lists the means of the nightly mean differential magnitudes for each observing season and the standard deviation of the means. These catalogs provide the data for the following variability and activity analysis.

*Diffmag* also creates a "check" file with the median absolute value of the differential magnitudes of all stars for each frame which can be used to check for bad data. By using differential ensemble photometry, the average brightness change of each star is forced to average to zero. The expectation is that the typical differential magnitudes of stars will be similar from frame to frame, so the median absolute value of the differential magnitudes of all stars on each frame can be used to check the overall data quality. Most of the median differential magnitudes are smaller than 20 mmag, but the Loral1 CCD median magnitudes are larger than the rest of our data by several hundredths of a magnitude, leading me to discard this data as was mentioned previously. I also removed from our analysis a few individual nights with large median differential magnitudes caused by clouds or occasional instrumental problems.

A sample plot of the check file is shown in Figure 3.7. The x-axis is simply all of the frames taken of NGC 7789, with the first frame taken in 1996 as #1. The y-axis is the median V differential magnitude on each frame. One can immediately see that some data points are significantly offset from the majority of the data. The group of data points labeled "A" are from observing runs on UT 1998 Nov 22, UT 1998 Nov 23, UT 1998 Dec 2, and UT 1998 Dec 6, taken with the Navy CCD. The only cause for the offset of the frames on these nights is the intrinsic noise in the CCD. The data points labeled "B" are from an observing run on UT 2000 Oct 12 using the Loral1 CCD; on this night, the Moon

was full. The data points labeled "C" were taken on UT 2001 Aug 23 using the Loral2 CCD. This night had some possible clouds.

By closely examining the check file and comparing it to the CCDs used, weather conditions, and any other unusual problems, I can eliminate data that have been compromised. For NGC 7789 in the B, V, and I filters, I eliminated all of the data taken with the Loral1 and Navy CCDs. I have also eliminated data taken on a few BU Queue nights. Accordingly, the log of the data remaining for NGC 7789 is given in Table 3.4. A plot to check these remaining data is in Figure 3.8. Some frames on this plot are still offset, but not as severely. Frames 1400 - 1500 constitute a few nights with intermittent clouds, for example.

## 3.3 Phase I Results: NGC 7789 as a Test Case

The primary goal is to search for signs of stellar activity of the stars in the clusters, as indicated by broad-band brightness fluctuations. Since the expected fluctuations are at the limit of the detection level, a method must be devised for distinguishing active stars from inactive stars. I rely on correlated fluctuations in different photometric band-passes. I selected NGC 7789 as a test case for investigating the analytical tools to be applied to all of the clusters. Since it is the youngest cluster in the program, the stars should be the most active.

### 3.3.1 Photometric Errors or Stellar Activity?

The expected real fluctuations for the stars in this program are not very different from the expected photometric errors. It is essential then both to evaluate the actual photometric errors, and to devise some way of testing whether the apparent fluctuations are real.

The SPS program (Janes & Heasley 1993), used in this project to do the stellar photometry, includes a calculation of the magnitude error for each star on each individual image, based on the known statistical characteristics of the image. The error estimate includes the Poisson statistics of the CCD pixels covering the star, error estimates of the

| Telescope | Dates (UT) | CCD | Usable Nights | Objects | Filters |
|---|---|---|---|---|---|
| MLO | 1996 Aug 18-24 | Loral | 7 | 1, 2, 4 | BVI |
| MLO | 1996 Oct 8-13 | Loral | 6 | 1, 2, 3, 4 | BVI |
| MLO | 1997 Sep 27-30 | Loral | 4 | 1, 2, 4 | UBV |
| MLO | 1997 Oct 29-30 | Loral | 2 | 1 | BV |
| MLO | 1998 Jul 24-31 | Loral | 6 | 1, 2, 4 | BVI |
| Perkins | 1998 Aug 3-6 | SITe | 4 | 1, 2 | BV |
| MLO | 1998 Sep 11-14 | Loral | 4 | 1, 2 | V |
| Perkins | 1998 Sep 12-15 | SITe | 2 | 1, 2 | UV |
| MLO | 1998 Oct 13-15 | Loral | 3 | 1, 2, 3, 4 | VR |
| Perkins | 1998 Oct 16-21 | SITe | 6 | 1, 2, 3, 4 | UVR |
| Perkins(Q) | 1998 Oct 29 | SITe | 1 | 1, 4 | V |
| MLO | 1998 Nov 18 | Loral | 1 | 1 | V |
| Perkins(Q) | 1999 Jan 5-6 | SITe | 1 | 1, 3, 4 | V |
| Perkins(Q) | 1999 Aug 1-2 | SITe | 1 | 1, 2 | V |
| Perkins(Q) | 1999 Aug 26-27 | SITe | 2 | 1, 2, 4 | V |
| Perkins | 1999 Sep 8-14 | SITe | 4 | 1, 2, 4 | V |
| MLO | 1999 Sep 12-15 | Loral | 3 | 1, 2, 4 | VI |
| Perkins(Q) | 1999 Sep 30 | SITe | 1 | 1, 2, 4 | V |
| Perkins | 1999 Oct 11-15 | SITe | 5 | 1, 2, 3, 4 | UBVRI |
| Perkins(Q) | 1999 Oct 21 | SITe | 1 | 1, 2, 3, 4 | V |
| Perkins(Q) | 1999 Oct 29 | SITe | 1 | 1, 2, 3, 4 | V |
| Perkins | 1999 Nov 11-15 | SITe | 5 | 1, 2, 3, 4 | VI |
| Perkins(Q) | 1999 Nov 21 | SITe | 1 | 1, 3 | V |
| Perkins | 2000 Jan 11-14 | SITe | 3 | 1, 3, 4 | VI |
| Perkins(Q) | 2000 Nov 16-19 | SITe | 3 | 1, 2, 3, 4 | V |
| Perkins(Q) | 2000 Dec 15 | SITe | 1 | 1 | V |
| Perkins | 2001 Jul 14-20 | Loral2 | 7 | 1, 2 | UBVRI |
| Perkins(Q) | 2001 Jul 28 | Loral2 | 1 | 1, 2 | VI |
| Perkins | 2001 Aug 22-28 | Loral2 | 7 | 1, 2, 4 | UBV |
| Perkins(Q) | 2001 Sep 11-12 | Loral2 | 2 | 1, 2, 4 | VI |
| Perkins(Q) | 2001 Sep 21 | Loral2 | 1 | 1, 2 | VI |
| Perkins(Q) | 2001 Sep 27 | Loral2 | 1 | 1, 2 | VI |
| Perkins | 2001 Oct 11-16 | Loral2 | 5 | 1, 2, 3, 4 | UBVI |
| Perkins | 2001 Dec 16-22 | Loral2 | 4 | 1, 3, 4 | BVR |

Table 3.4: Phase I Observations of NGC 7789. "MLO" refers to the 1.0-m Mt. Laguna Observatory telescope. "Perkins" refers to the 1.8-m Perkins Telescope at Lowell Observatory. A Q after the telescope name denotes observations made by the BU Queue observer, as explained in the text. The CCD designations "Loral", "SITe", and "Loral2" are explained in the text. The clusters are assigned numbers in order of age: 1 - NGC 7789, 2 - NGC 6819, 3 - M67, 4 - NGC 188.

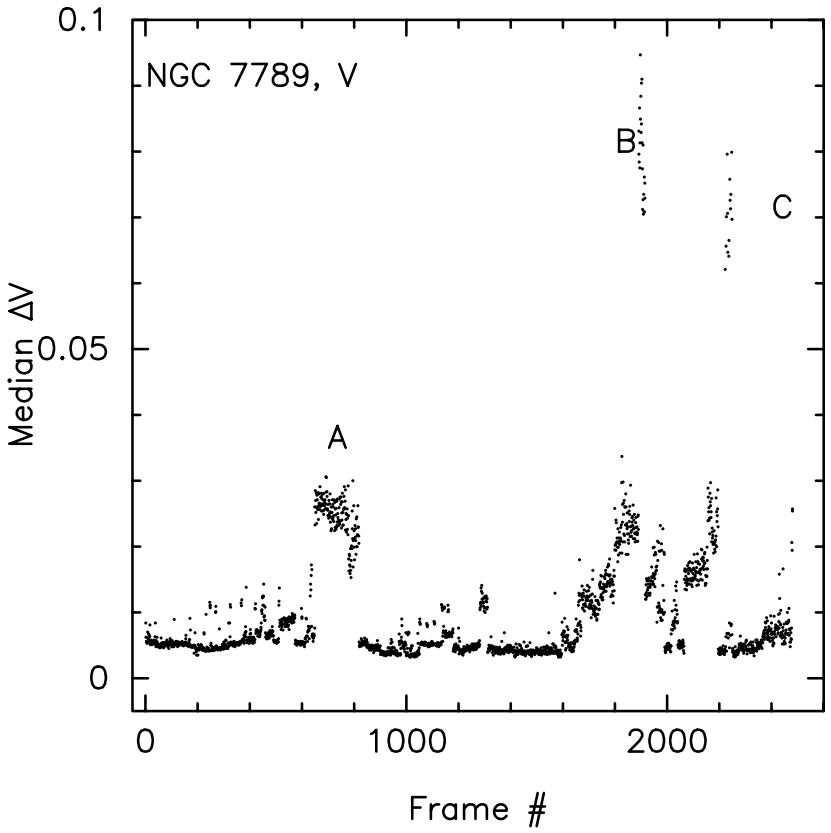


Figure 3.7: Differential ensemble photometry check. The x-axis numbers all the frames taken of NGC 7789. The y-axis is the median V differential magnitude for each frame. The points at A are due to observing runs on UT 1998 Nov 22, UT 1998 Nov 23, UT 1998 Dec 2, and UT 1998 Dec 6. The points at B are from an observing run on UT 2000 Oct 12. The points at C are from an observing run on UT 2001 Aug 23. Please see the text for explanation.

sky background, flat-field error, read-noise error, errors introduced when close companion stars are subtracted from the image and errors in the calculated point-spread function. These are combined to generate a predicted photometric error for that star on that frame ($\sigma_{SPS}$).

SPS does not take into account some known CCD imaging considerations, such as charge-transfer effects, sub-pixel sensitivity variations or non-linearities in the CCD response (except that a saturation level is specified). Fortunately, given the well-sampled star images typical with ground-based telescopes and the differential magnitude approach,

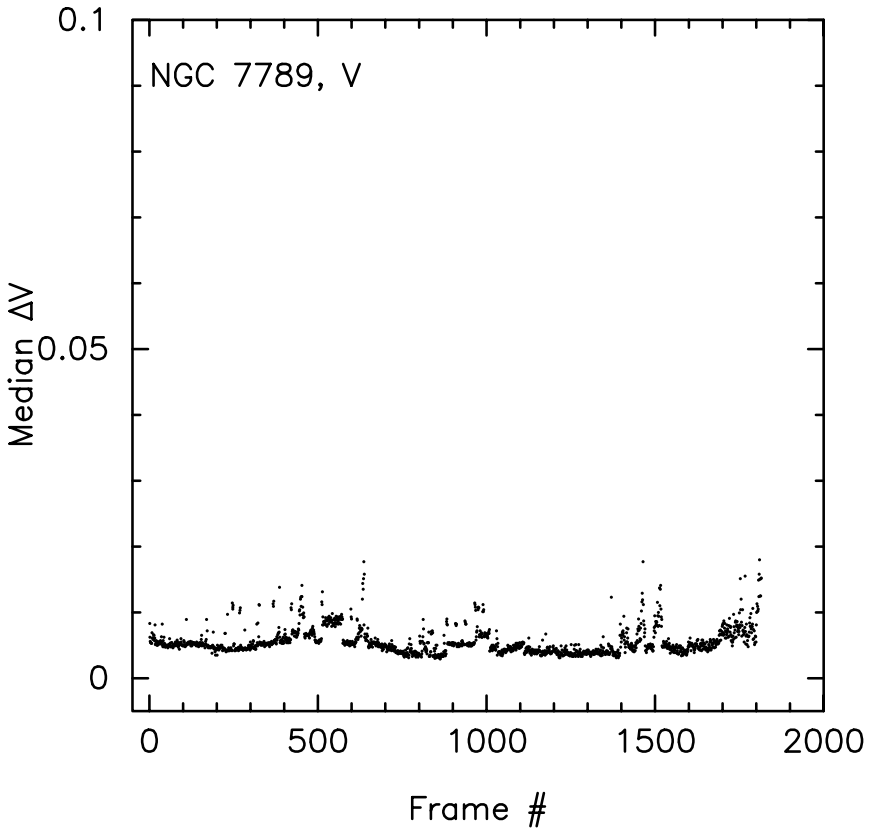


Figure 3.8: Differential ensemble photometry re-check. The x-axis numbers all the frames taken of NGC 7789. The y-axis is the median V differential magnitude for each frame. This plot contains only the data taken on the nights in the log in Table 3.4.

these problems can be ignored.

**Differential Magnitude Errors**

The program written to calculate differential magnitudes (*diffmag*) generates several additional error estimates. The first set of measurements refer to individual frames. First, diffmag adds a correction to $\sigma_{SPS}$ to account for the uncertainty introduced in the differential magnitude process. Since the differential magnitude is based on the difference on a frame between the target star and the ensemble stars, the variance in the brightness of those stars must be taken into account. The ensemble error is based on the mean differential magnitudes and the variance of those means for the ensemble stars, which includes

both measurement errors of the ensemble stars and any intrinsic variability. (Note, however, that the ensemble magnitude used to set the zero point for the target star on that frame is based on the median of the ensemble magnitudes.) The additional ensemble error is added in quadrature to $\sigma_{SPS}$ – I call the resulting error $\sigma_{phot}$. Next, *diffmag* calculates the root-mean-square value of the differential magnitude measurements of a star on all the frames where that star was measured ($\sigma_f$):

$$\sigma_f^2 = \frac{1}{\sum_{k=1}^{N_p} N_{k,p}} \sum_{k=1}^{N_p} \sum_{j=1}^{N_{k,p}} D^2(j,k,p). \tag{3.6}$$

*Diffmag* computes other quantities from the data as well. The nightly mean differential magnitudes are calculated according to

$$\overline{D}_{k,p} = \frac{1}{\sum_{j=1}^{N_p} N_{k,p}} \sum_{j=1}^{N_{k,p}} D(j,k,p). \tag{3.7}$$

Then the standard deviation of the nightly mean differential magnitudes is

$$\sigma^2_{\overline{D}_{k,p}} = \frac{1}{N_{k,p}(N_{k,p}-1)} \sum_{j=1}^{N_{k,p}} \left[D(j,k,p) - \overline{D}_{k,p}\right]^2. \tag{3.8}$$

Using these quantities, *diffmag* calculates the root-mean-square value of the nightly mean differential magnitudes ($\sigma_{rms}$) as well as the nightly standard errors of the mean of the frames on individual nights ($\sigma_{mean}$).

$$\sigma^2_{rms} = \frac{1}{N_p} \sum_{k=1}^{N_p} \overline{D}^2_{k,p}. \tag{3.9}$$

The RMS of the standard deviations of the mean of the nightly mean differential magnitudes is:

$$\sigma^2_{mean} = \frac{1}{N_p} \sum_{k=1}^{N_p} \sigma^2_{\overline{D}_{k,p}}, \tag{3.10}$$

where the quantities are the same as those defined earlier.

Figure 3.9 shows the median values $\sigma_{rms}$, $\sigma_{mean}$, and $\sigma_{phot}$, taken in half-magnitude bins, versus magnitude for all stars. The brightest four bins contain a couple dozen stars each, but the bins for the fainter stars contain a couple hundred stars each. ($\sigma_f$ is not

shown, see next paragraph.) Similar statistical quantities are calculated for the annual mean differential magnitudes.

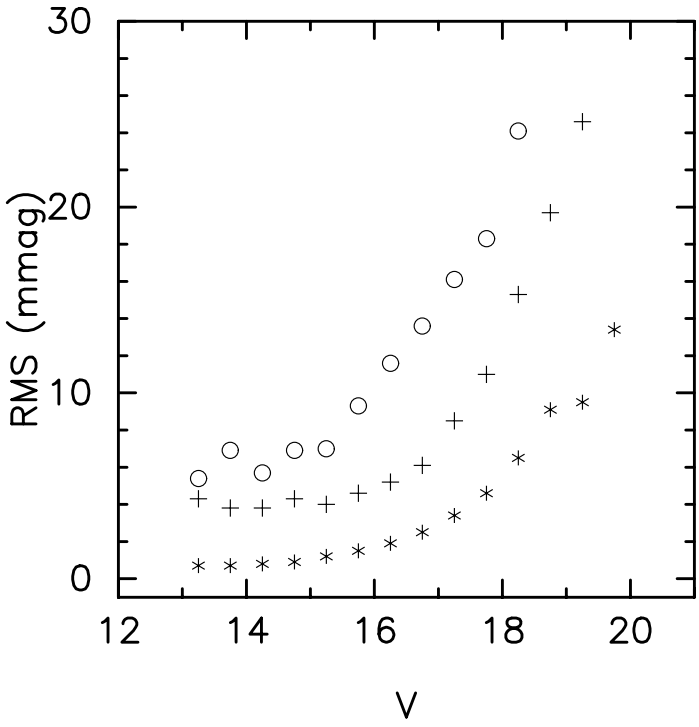


Figure 3.9: V magnitude versus the median value of $\sigma_{mean}$, $\sigma_{rms}$, and $\sigma_{phot}$ for NGC 7789 stars, taken in half-magnitude bins. The circles are $\sigma_{phot}$, the crosses are $\sigma_{rms}$ and the asterisks are $\sigma_{mean}$. The offset between $\sigma_{rms}$ and $\sigma_{mean}$ for V $< 16$ is used to determine the ensemble error, which is approximately 3 mmag for NGC 7789.

If all sources of measurement error have been accounted for and if a star is perfectly constant in magnitude, then simple error propagation rules should fix the relationships among these various error quantities. To test this, diffmag calculates the ratio of the RMS value of $\sigma_f$ to the RMS value of $\sigma_{phot}$ on all frames. For inactive stars, whose errors are adequately represented by the photometric errors, the error ratio should be one. Using our V data as an example, Figure 3.10 shows how the median value of $\sigma_f/\sigma_{phot}$, taken in half-magnitude bins, varies with magnitude. For $13.5 < V < 18$, the ratio is very close to unity, which indicates that diffmag is not systematically underestimating the photometric errors. Fainter than $V \sim 18$, the ratio grows slowly; either as a result of some type of

photometric noise, such as sky noise, or as an indication of a physical process in these stars.

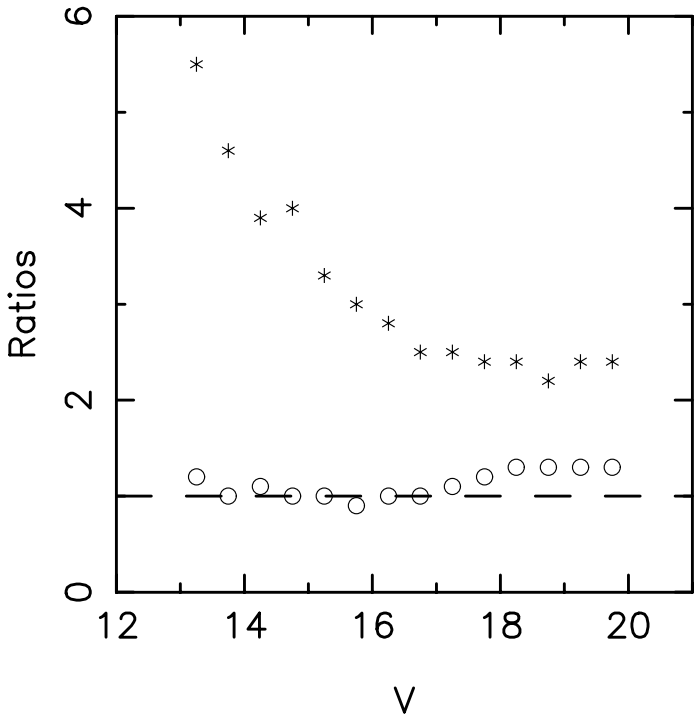


Figure 3.10: Plot of the ratios $\sigma_f/\sigma_{phot}$ and $\sigma_{rms}/\sigma_{mean}$ for the standard data analysis, taken in half-magnitude bins. The circles are $\sigma_f/\sigma_{phot}$ and the asterisks are $\sigma_{rms}/\sigma_{mean}$. The ratio $\sigma_f/\sigma_{phot}$ is approximately unity, which indicates that SPS and *diffmag* are adequately estimating the photometric errors on a frame-by-frame basis. The ratio $\sigma_{rms}/\sigma_{mean}$ is larger than unity, which indicates that the stars are varying between nights of observations, but not within single nights of observations.

For the null case of an unvarying star, $\sigma_{rms}$ and $\sigma_{mean}$ should be identical. Figure 3.10 shows the median value of the ratio $\sigma_{rms}/\sigma_{mean}$ by magnitude. The ratio is $\sim$4 - 6 at brighter magnitudes and decreases as the stars become fainter. Figure 3.9 shows $\sigma_{rms}$ and $\sigma_{mean}$ plotted by magnitude. Within single nights, the differential magnitudes for individual bright stars do not vary by more than $\sim$4 - 5 mmag, but between the nights the magnitudes are different. $\sigma_{rms}$ is approximately 3 mmag greater than $\sigma_{mean}$ for stars brighter than $V \sim 16$.

To understand th offset between $\sigma_{rms}$ and $\sigma_{mean}$, the errors in the differential magnitudes must be closely examined. When Equations 3.3, 3.4 and 3.5 (the differential magnitude per star per frame, the mean magnitude of the star and the zeropoint magnitude per frame) are combined, the differential magnitude for star $p$ on frame $j$ of night $k$ becomes:

$$D(j,k,p) = m(j,k,p) - \frac{1}{\sum_{k=1}^{N_p} N_{k,p}} \sum_{k=1}^{N_p} \sum_{j=1}^{N_{k,p}} m(j,k,p)$$
$$-\frac{1}{E_p} \sum_{e=1}^{E_p} \left( m(j,k,e) - \frac{1}{\sum_{k=1}^{N_e} N_{k,e}} \sum_{k=1}^{N_e} \sum_{j=1}^{N_{k,e}} m(j,k,e) \right) \tag{3.11}$$

The second and last terms are constant in this implementation of the analysis, and in any case are very small.

The variance in $D(j,k,p)$ is due to the photometric errors in the measured magnitudes as well as the variance in the zero point:

$$\sigma(D(j,k,p)) = \left[\sigma^2(m(j,k,p)) + \sigma^2(z(j,k,p))\right]^{\frac{1}{2}}. \tag{3.12}$$

The variance in the zero point is computed in $diffmag$. In calculating the error of the nightly mean differential magnitudes, the terms in Equation 3.12, which originate primarily from random photometric errors, will tend toward small values as the number of frames increases. (However, they probably cannot be reduced to an arbitrarily low level because there may be some small systematic error present.) Examination of Figure 3.9 shows that the errors are not fully accounted for, since $\sigma_{rms}$ is offset above $\sigma_{mean}$. I have named this offset the ensemble error, which is the result of intrinsic variability of the ensemble stars and possible calibration errors. Previously the offset was determined to be 3 mmag. In NGC 7789, stars brighter than V $\sim$ 16 have sufficiently low photometric errors that the ensemble error is significant; for fainter stars, the photometric errors dominate the error budget.

It is important to note that this is a worst-case analysis. If, in fact, the individual stars are actually variable, then the offset between $\sigma_{rms}$ and $\sigma_{mean}$ would result from that

variability. By forcing a fixed ensemble error, only the really large amplitude variables, those with amplitudes larger than the ensemble error, will be uncovered.

Could this "ensemble error" be due to some problem with the statistical calculations? I tested this by randomizing the data taken through the V filter. The nightly mean differential magnitudes were re-distributed randomly among the stars. Each star received the same number of nightly mean differential magnitudes as it originally had. This simulates a scenario where all of the stars vary randomly during all nights of observations. When $\sigma_{rms}$ and $\sigma_{mean}$ were calculated for the randomized data, the values are identical, as seen in Figure 3.11. Either the stars vary, or some unknown calibration problem must be resolved. When variable stars are identified in the subsequent analysis, they must vary significantly compared to both the ensemble error as well as the photometric errors.

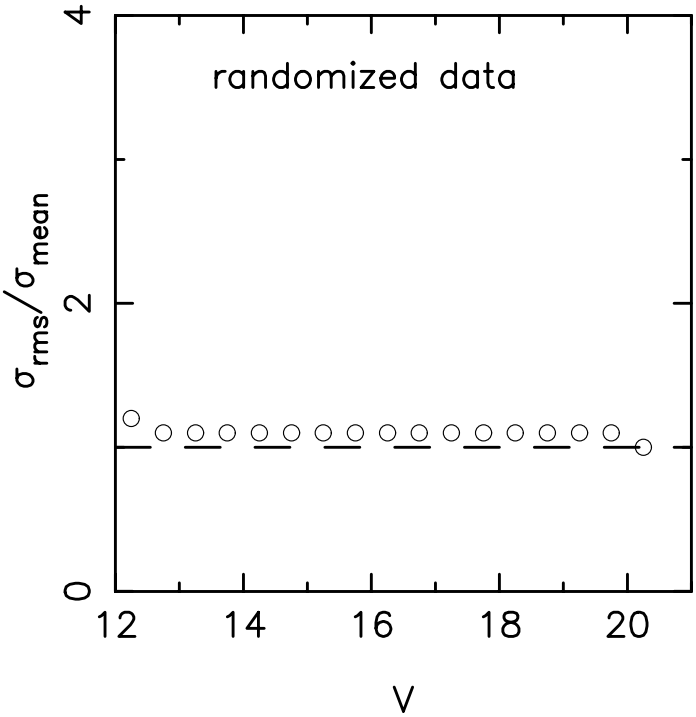


Figure 3.11: Plot of the ratio $\sigma_{rms}/\sigma_{mean}$ for the randomized data, taken in half-magnitude bins. The ratio is unity, unlike the ratio in Figure 3.10. In the randomized data, the stars vary as much within a single night as they do between nights of observations.

### Comparison of Simultaneous Observations on Two Telescopes

To test the consistency of the photometric analysis, NGC 7789 was observed simultaneously by two telescopes on UT 1999 Sep 13. At the Perkins Telescope, the sky conditions went from clear to partly cloudy during the observations. The observations made with the Perkins Telescope were at one position in the center of the cluster. At MLO, the sky was clear, and the telescope was pointed close to the center of the cluster, then offset, and then re-pointed approximately to the cluster center. The MLO observations extended a few hours before and after the Perkins observations. Table 3.5 lists the observations and their fractional Julian dates. In this discussion, all of the Perkins data will be referred to as "Perkins". The MLO data first taken when centered on the cluster are designated "MLO1", when offset from the cluster center "MLO2", and when re-centered on the cluster "MLO3". The MLO data are referred to collectively as the MLO data.

| Data Description | Fraction of Day | Data Designation |
|---|---|---|
| Perkins data | 0.28947 - 0.48324 | "Perkins" |
| MLO data, centered | 0.23345 - 0.31080 | "MLO1" |
| MLO data, offset | 0.33745 - 0.41650 | "MLO2" |
| MLO data, re-centered | 0.43215 - 0.51428 | "MLO3" |

Table 3.5: NGC 7789 observations on UT 1999 Sep 13. The fraction of day is the fraction of the Julian date when the observations were begun and finished. The Perkins data were centered on the cluster. The MLO2 data were offset from the cluster center. The MLO1, MLO2, and MLO3 data sets are collectively referred to as "MLO" during this discussion.

Only stars that were observed in each of the four data sets (Perkins, MLO1, MLO2, and MLO3) are compared. Over the single night these observations were taken, the vast majority of these stars should not vary. To ensure this, I considered only stars with $12 < V < 16$, corresponding to spectral types earlier than the Sun and thus have little or no stellar activity. Only 169 stars fall in this magnitude range. If the photometry is calibrated correctly, the mean differential magnitudes for each star should be the same in all four data sets.

Figure 3.12 shows histograms of the mean magnitudes for the stars in each dataset.

| Data Designation | Mean (mmag) | Median (mmag) | Std. Dev. (mmag) |
|---|---|---|---|
| Perkins | 0.0 | 0.1 | 5.5 |
| MLO | 0.3 | 0.8 | 4.8 |
| MLO1 | 0.4 | 0.8 | 5.2 |
| MLO2 | 0.2 | 0.7 | 5.2 |
| MLO3 | 0.4 | 0.6 | 5.6 |
| (Perkins - MLO)/$\sqrt{2}$ | -0.2 | -0.6 | 4.7 |
| (Perkins - MLO1)/$\sqrt{2}$ | -0.2 | -0.3 | 4.8 |
| (Perkins - MLO2)/$\sqrt{2}$ | -0.1 | -0.6 | 5.1 |
| (Perkins - MLO3)/$\sqrt{2}$ | -0.3 | -0.4 | 4.9 |
| (MLO1 - MLO2)/$\sqrt{2}$ | 0.1 | -0.1 | 2.9 |
| (MLO1 - MLO3)/$\sqrt{2}$ | -0.1 | -0.1 | 3.1 |

Table 3.6: Statistical properties of data sets from the MLO and Perkins telescopes on UT 1999 Sep 13. The distributions are plotted in Figures 3.12 and 3.13.

The means, medians, and standard deviations of the mean magnitudes for each dataset are listed in Table 3.6. The means of the mean magnitudes for each dataset are very similar ($\sim$0.3 mmag); the zero points of the magnitude scale are the same for each dataset, despite the different telescope and CCD camera. The medians fall within a range of $\pm$ 0.8 mmag. The standard deviations of each dataset agree well at approximately 5 mmag. Figure 3.13 shows the mean magnitudes for the stars in each dataset plotted versus the mean magnitudes each star had in the other datasets.

Panels a, b, and c of Figure 3.13 show the Perkins dataset plotted versus the MLO datasets. The magnitudes seem to be scattered randomly about the origin with no correlation. Panel d in Figure 3.13 shows the Perkins mean magnitudes versus the MLO mean magnitudes. Again, the points are randomly scattered about the origin. Finally, panels e and f show the MLO1 dataset plotted versus the MLO2 and MLO3 datasets. In these plots, a positive correlation can be seen between the datasets. In the comparisons with the Perkins dataset, the stars display no variability above the 5 mmag level of the scatter; however, we specifically chose these stars to be non-variable. Nevertheless, in the MLO1 vs. MLO2 and MLO1 vs. MLO3 plots, the positive correlation hints at possible variability

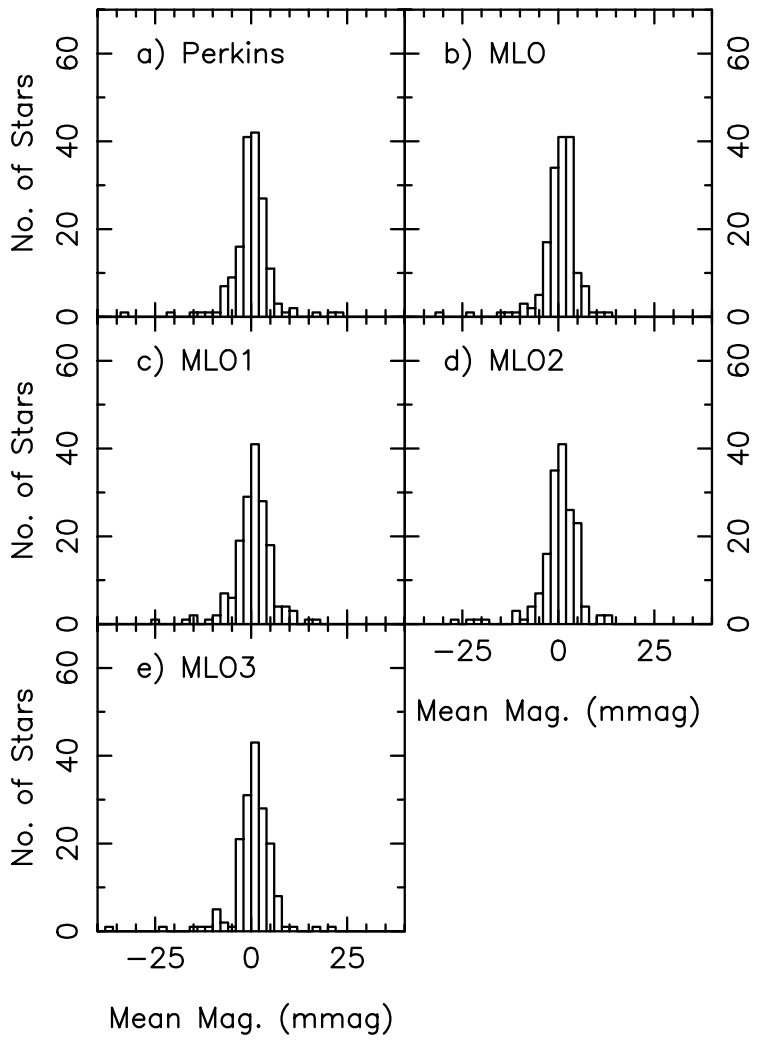


Figure 3.12: Histograms of mean differential magnitudes for the datasets listed. The "Perkins" dataset is all the observations taken at the Perkins telescope on UT 1999 Sep 13. The "MLO" dataset is all the observations taken at the Mt. Laguna Observatory 1 m telescope on that date. The "MLO1" dataset is the observations taken when the telescope pointed at the center of the cluster at the beginning of the night at Mt. Laguna. The "MLO2" data is the observations taken when the telescope was pointed at a position offset from the cluster center, and the "MLO3" data set is the observations taken when the telescope was re-pointed at the cluster center at the end of the night. Table 3.6 lists statistical quantities for the distributions.

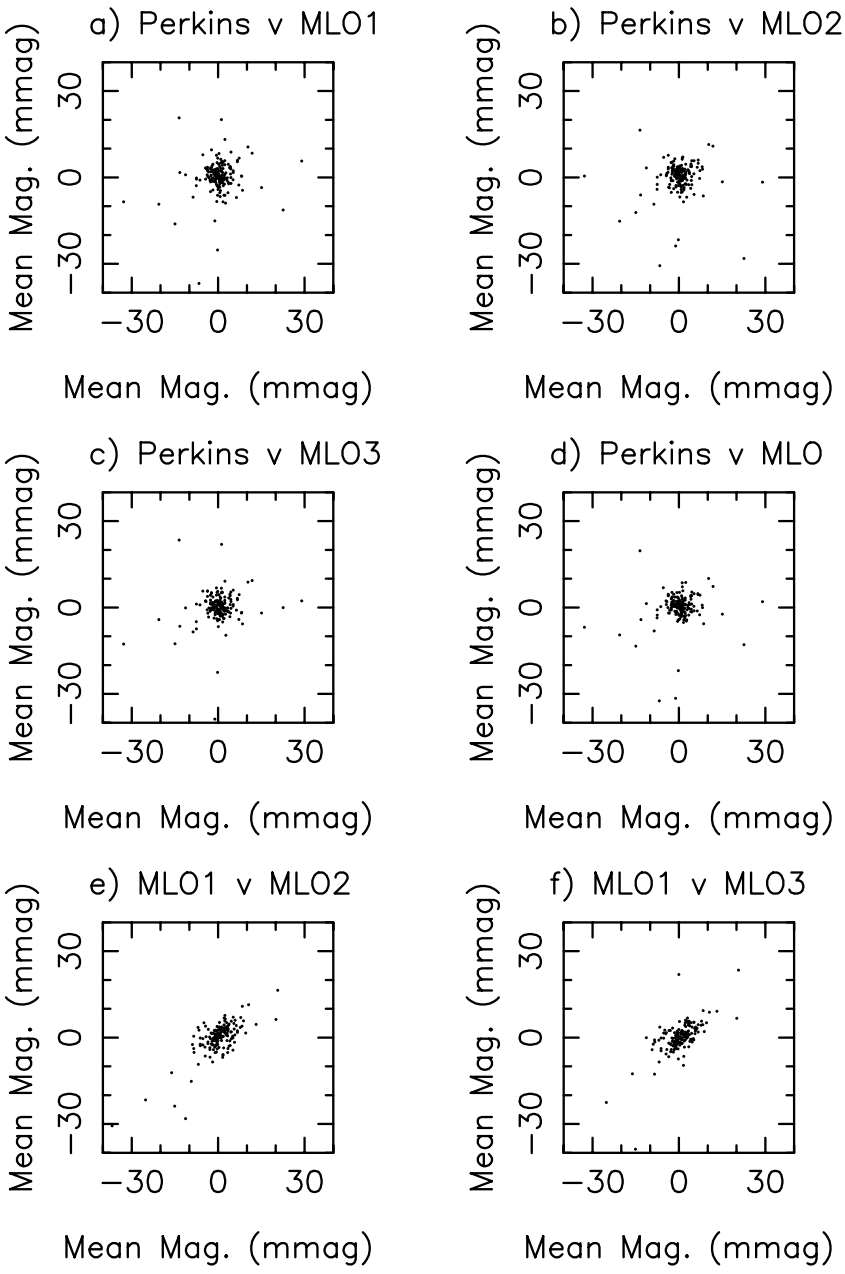


Figure 3.13: Mean differential magnitudes plotted against each other for the datasets listed. The "Perkins" dataset is all the observations taken at the Perkins telescope on UT 1999 Sep 13. The "MLO" dataset is all the observations taken at the Mt. Laguna Observatory 1 m telescope on that date. The "MLO1" dataset is the observations taken when the telescope pointed at the center of the cluster at the beginning of the night at Mt. Laguna. The "MLO2" data is the observations taken when the telescope was pointed at a position offset from the cluster center, and the "MLO3" data set is the observations taken when the telescope was re-pointed at the cluster center at the end of the night. Table 3.6 lists statistical quantities for the distributions.

in these stars at a very low level. Table 3.6 shows that the standard deviations along the $x = y$ line for the data on these two plots are only about half as large as that for the other plots.

The comparison of the Perkins and MLO data, both as a whole and in subsets, for the night of UT 1999 Sep 13 shows that the telescope and CCD do not significantly affect the photometric calibrations *a priori*. The mean differential magnitudes determined for stars observed simultaneously with the two telescopes agree within about 5 mmag. I have also verified that stars with $12 < V < 16$ do not vary at a level below 5 mmag.

#### Summary of Errors

I have demonstrated that the V filter nightly mean differential magnitudes have an ensemble error of 3 mmag. I determined it by examining $\sigma_{rms}$ and $\sigma_{mean}$ (Figure 3.9).

Finally, the comparison of the data taken simultaneously on two telescopes shows that the calibration of the photometry between data from the two telescopes and the internal calibration of the photometry from one telescope is comparable. The zero points of the photometry are the same.

Any method used to search for activity in the stars in NGC 7789 must compensate for the ensemble error. Since the contribution to the ensemble error from stellar activity for individual stars cannot be quantified, the standard for what constitutes an active star must be stringent.

### 3.3.2 An Activity Index: The Nightly Mean Differential Magnitudes

Now that I have assessed the errors in our dataset, I must find a quantitative measure of real variability. First I must identify the candidate variable stars - those stars whose fluctuations are significantly larger than the errors. Then I must verify that these fluctuations have a physical origin by examining the correlation of the fluctuations between colors.

I have created an activity index, $A_v(p)$, which sums nightly mean differential magni-

tudes in the V filter for each star $p$:

$$A_v(p) = \left( \frac{1}{N_p} \sum_{k=1}^{N_p} \overline{D}^2(k,p) \right)^{\frac{1}{2}}, \tag{3.13}$$

where $\overline{D}(k,p)$ is the mean differential magnitude of star $p$ on night $k$, defined in Equation 3.7. Thus $A_v(p)$ is the RMS amplitude of the brightness fluctuations in magnitudes. I have calculated it using V data for stars with $N_p \geq 5$. $A_v(p)$ is identical to the $\sigma_{rms}$ statistic calculated earlier in Equation 3.9.

The RMS error of the activity index is:

$$\sigma_{A_v}(p) = \left[ \frac{1}{N_p} \sum_{k=1}^{N_p} \frac{\sum_{j=1}^{N_{k,p}} (D(j,k,p) - \overline{D}(k,p))^2}{N_{k,p}(N_{k,p}-1)} + \sigma_{ens}^2 \right]^{\frac{1}{2}}, \tag{3.14}$$

The first term inside the brackets is just the standard deviation of the mean differential magnitude $\overline{D}(k,p)$ of star $p$ on night $k$. The additional term $\sigma_{ens}$ is the ensemble error of 3 mmag determined in the previous section. If the ensemble error is set to zero, $\sigma_{A_v} = \sigma_{mean}$ from Equation 3.10.

Finally, I compare $A_v(p)$ to its RMS error for each star, calling the ratio $\alpha_v(p)$ the significance index:

$$\alpha_v(p) = \frac{A_v(p)}{\sigma_{A_v}(p)}. \tag{3.15}$$

Any star with $\alpha_v \geq 3$ is a candidate variable star, since its brightness fluctuations are three times as large as its error.

Before calculating the significance index, I first selected the main sequence stars from the data in order to remove the field stars from consideration; the field stars have unknown ages and compositions and thus are not suited to this study. My method is completely photometric; by examining the color-magnitude diagram of NGC 7789, I constructed a main sequence curve. Then for each magnitude I selected the stars within a B-V color range determined by typical magnitude errors at that V magnitude. I also purposely expanded the range redward to include the binary sequence. In addition, I only selected stars between $13.5 < V < 18.5$; stars brighter than $V < 13.5$ could have saturation effects

and stars fainter than $V > 18.5$ have a poor signal-to-noise ratio. Known periodic variables have been removed from the list of main sequence stars (see Chapter 5). Figure 3.14 shows color-magnitude diagrams for NGC 7789; panel a shows all stars observed, and panel b shows the more than 2000 main sequence stars.

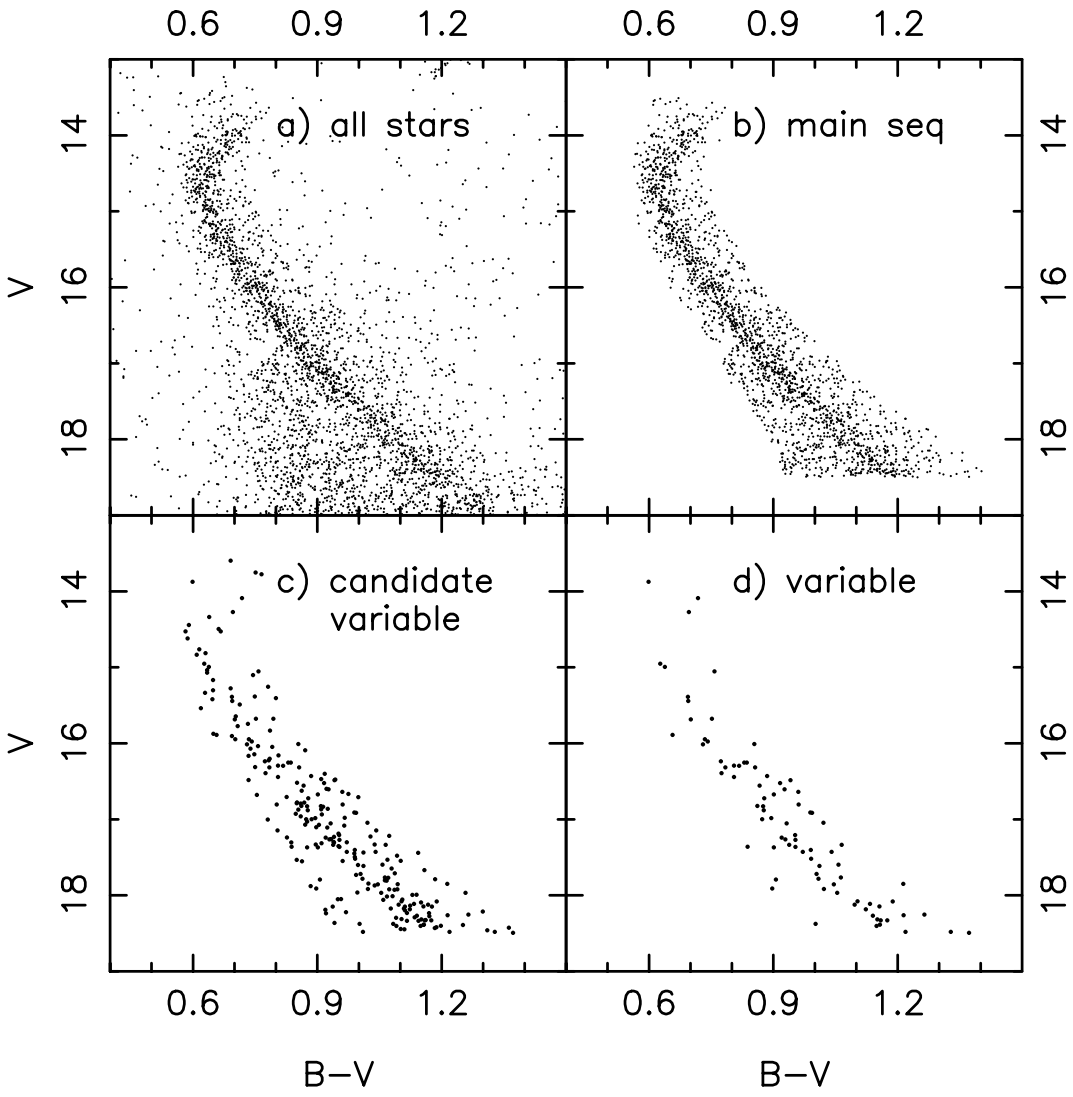


Figure 3.14: Color-magnitude diagrams for NGC 7789. Panel a shows all stars observed. Panel b shows the stars photometrically chosen as the main sequence. Panel c shows the candidate variable stars. Panel d shows the variable stars, with $\alpha \geq 3$ and whose colors are correlated at a 99% significant level.

To find the candidate variable stars, I calculate $\alpha_v$ for each star with at least five nights of observations through the V filter. I set $\sigma_{ens} = 3$ mmag for the V filter, following the § 3.3.1. In NGC 7789, over 3100 stars had at least five nights of observations; over 1500 of these stars fell on the main sequence. The fewest nights a star was observed was five, and the most was 58; the median number of nights was 21. Figure 3.15 shows how the median values $\alpha_v$, $A_v$, and $\sigma_{A_v}$ vary with magnitude for the main sequence stars. Panel a shows the significance index. Panel b shows the activity index and its error. The typical star has $1.5 < \alpha_v < 2$ and consequently is not considered a candidate variable. $A_v$ increases for stars fainter than $V \sim 17$. The error in the activity index is the smallest for the brightest stars, where it is dominated by the ensemble error, and then increases for the fainter stars. The definitions of the variability classification scheme are in Table 3.7.

| Classification Name | $\alpha_v$ Requirement | $r$ Requirement |
|---|---|---|
| candidate variable | $\geq 3$ | none |
| variable | $\geq 3$ | 99% significant, positive |
| active | $\geq 3$ | 99% significant, positive |

Table 3.7: Classification scheme for variability. Variable stars and active stars have the same requirements for the significance index and correlation coefficient, however, a star could be variable but not active if the variability is attributable to another cause, such as pulsations or eclipses.

Now that I have identified the candidate variable main sequence stars, I verify which stars are variable by comparing their fluctuations in different colors. In any thermal process that causes brightness changes in a star, the variations in brightness are correlated in each color. I have calculated the linear correlation coefficient $r$ between the V and B nightly mean differential magnitudes and the V and R nightly mean differential magnitudes for the stars that have at least five nights with observations in B and V and/or V and I; a night where B, V and I were observed would count as two nights. Figure 3.16, panel a, shows the variation of $r$ with magnitude for all the main sequence stars. While there are

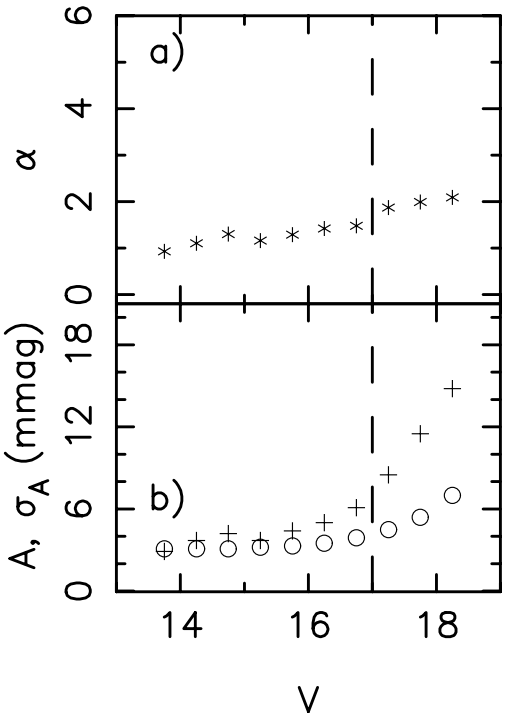


Figure 3.15: The median values of the significance index ($\alpha_v$), activity index ($A_v$), and the error in the activity index ($\sigma_{A_v}$) as a function of magnitude for NGC 7789, taken in half-magnitude bins. Panels a shows the significance index. Panel b shows the activity index (crosses) and the error in the activity index (circles). The dashed line indicates the Sun's magnitude at the distance of the cluster.

many anti-correlated stars, the brightness fluctuations are correlated in different colors; this indicates that a large fraction of stars are variable at the millimagnitude level. Panel b shows the ∼250 main sequence stars considered to be candidate variable stars; the brightness fluctuations in these stars are also positively correlated.

The result is that 80 stars of approximately 1500 main sequence stars (5%) with at least five nights' observations through at least two filters are found to be variable compared to their errors and significantly correlated. Panel d of Figure 3.14 shows these stars; few bright stars are variable. Figure 3.17 shows the mean V differential magnitudes versus the mean B or I differential magnitudes for the nights with observations through two or more of the B, V, or I filters. Each star has more than one point on the plot, since all

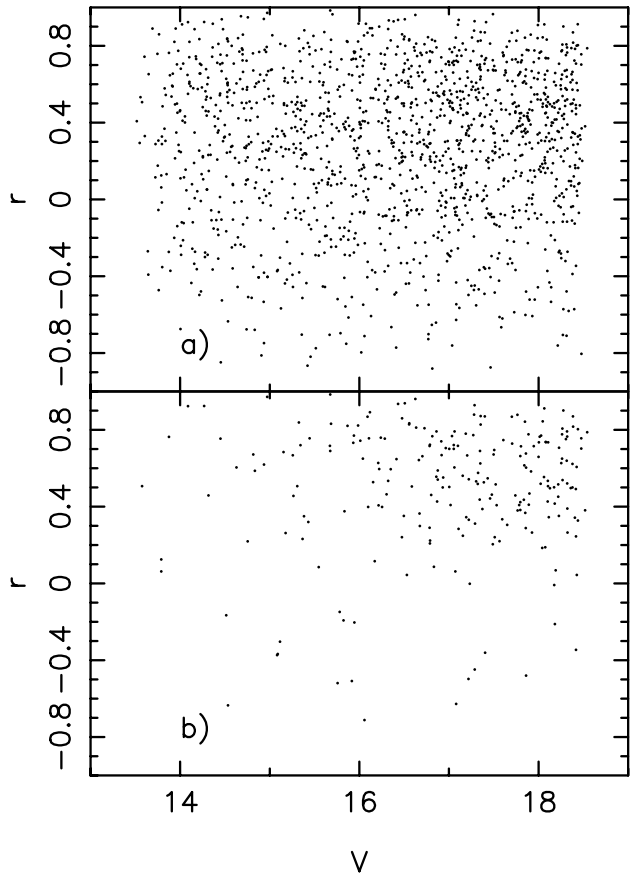


Figure 3.16: The correlation coefficient ($r$) as a function of magnitude. Panel a shows all main sequence stars. Panel b shows the candidate variable stars.

qualifying nights are displayed. The left panel shows all of the main sequence stars; very little correlation between the colors can be seen. The right panel shows the variable stars, which have a much more obvious correlation. The correlation between the colors of these variable stars is what would be expected of brightness changes due to stellar activity or any other thermal process on the star. I designate these stars as "active".

### Comments

The number of stars with sufficient observations for this analysis is severely limited by the field of view. The field of view of the Mt. Laguna telescope was adequate to observe the

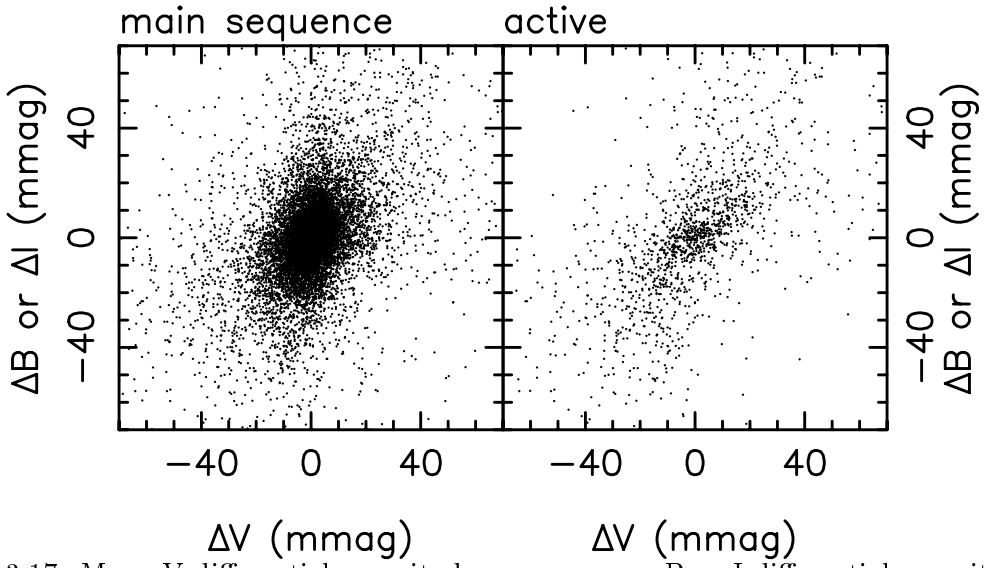


Figure 3.17: Mean V differential magnitudes versus mean B or I differential magnitudes for all main sequence stars in the left panel and for the active stars in the right panel.

entire cluster, but when the observing program began at the Perkins telescope, the field of view was decreased to five arcminutes with the SITe and Navy CCDs and then to three arcminutes with the Loral1 and Loral2 CCDs. Consequently, only the stars in the central section of the cluster were imaged over the entire six years of observations. Many stars included in the analysis have fewer than a dozen nights of observations taken through the V filter. Does this affect the number of active stars I determine? The above analysis was repeated for stars with more than the median number of nights (21); in this case, we found 78 of the same active stars, but in a main sequence population of approximately 830 stars. The stars with few nights of observations do not seem to be inappropriately inflating the number of active stars.

Because the field was too crowded to perform aperture photometry at the high level of precision required, I performed PSF photometry on the data (as described in the previous section). Neighboring stars whose PSFs blend together could cause spurious fluctuations in the measured magnitudes. I examined the contribution of this effect by performing the above analysis on stars isolated from their neighbors by ten arcseconds, which decreased

the number of main sequence stars in the analysis to approximately 500. I found that 4% of these stars were active, which is a similar fraction of active stars as when I included all the main sequence stars.

The expected fluctuations for photospheric activity in old stars are not very different from the photometric errors. I have selected a subset of stars that were chosen photometrically to be main sequence stars, within $13.5 < V < 18.5$ to minimize photometric errors. I have previously identified an ensemble error of the order $\sim 3$ mmag in the magnitude errors for the V data. However, using the activity index and its error, I have shown that $\sim 5\%$ of stars in NGC 7789 are variable at a 99% level of confidence and that the fluctuations in the active stars are due to thermal phenomena. Possible causes of this type of variability includes eclipses, reflections, or ellipticity effects of close binary systems, and stellar activity. As I will show below, the power spectra of these stars do not show any periodicity expected close binaries. Consequently, I believe these stars vary due to stellar activity.

### 3.3.3 Power Spectra

As demonstrated in the previous sections, many of the stars are variable. Consequently, it was natural to search for periodicities in each star's lightcurve. Although there are at most fifty-eight nights of data per star scattered across a six year period, stars with well-defined periodicities might be identifiable. I have taken the power spectra of the nightly mean differential magnitude data for both our variable and non-variable stars. The power spectrum routine for unevenly-spaced data, taken from *Numerical Recipes in C* (Press et al. 1993), includes the subtraction of the window power spectrum from the data's power spectrum.

First, I considered an "easy" power spectrum, that of the binary star 2055 (see Table 5.1); this spectrum was taken of the differential magnitude data from the $\sim$ 1500 individual frames. Searching periods of 0.5 - 2.0 d yielded the period 0.585 d with the

highest power with a significance of 1.0; the actual period is twice this period: 1.170 d. As is common with double-peaked signals where the maxima are of similar amplitudes, half the period has the most significant power. Figure 3.18 shows the power spectrum for star 2055 as well as the power spectrum of the data window. In this case, the power in the spectrum of the data window is insignificant compared to that of the signal itself.

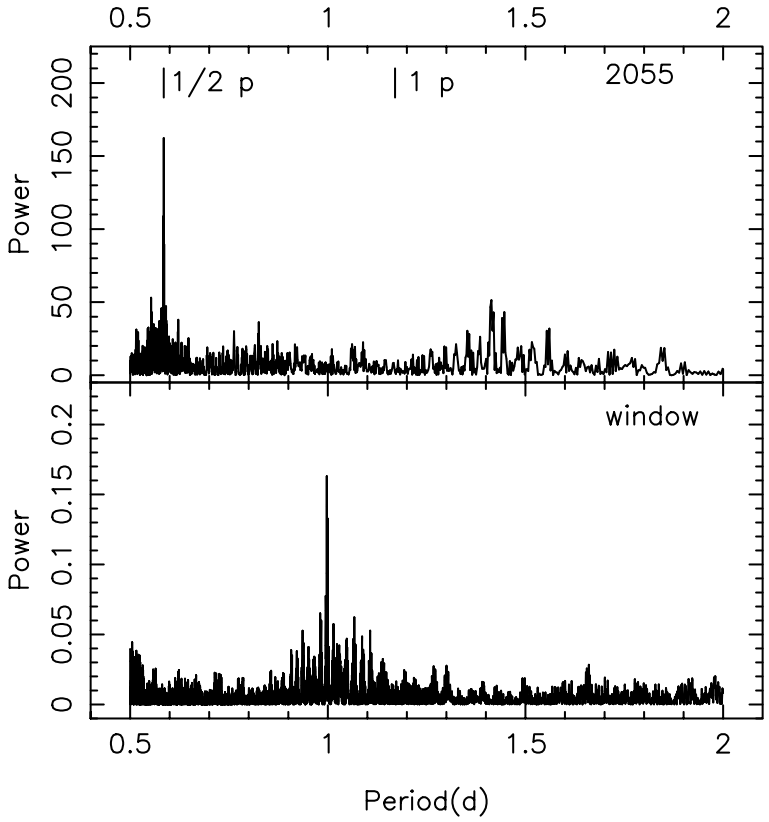


Figure 3.18: Power spectrum for Star 2055. The locations of the period and half of the period are marked. Note the differing y-axes.

Identification of signals in the nightly mean differential magnitude data is much more difficult when there is no single strong period as with a binary star. Figure 3.19, panel a, shows the distribution of periods of maximum power for the 248 candidate variable main sequence stars identified with the activity index calculation. Panel b shows the distribution of periods of maximum power for 327 non-variable main sequence stars with $\alpha_v < 1.0$. The distributions are virtually identical, with a small peak at approximately

30 d and a large peak at 40 d; the power spectra were calculated between 1 and 40 d. The distributions are filled in more between the 30 and 40 d peaks. The 30 d peak is a typical length of time between the observing runs in one season. Neither group of stars shows any evidence of periodic variability.

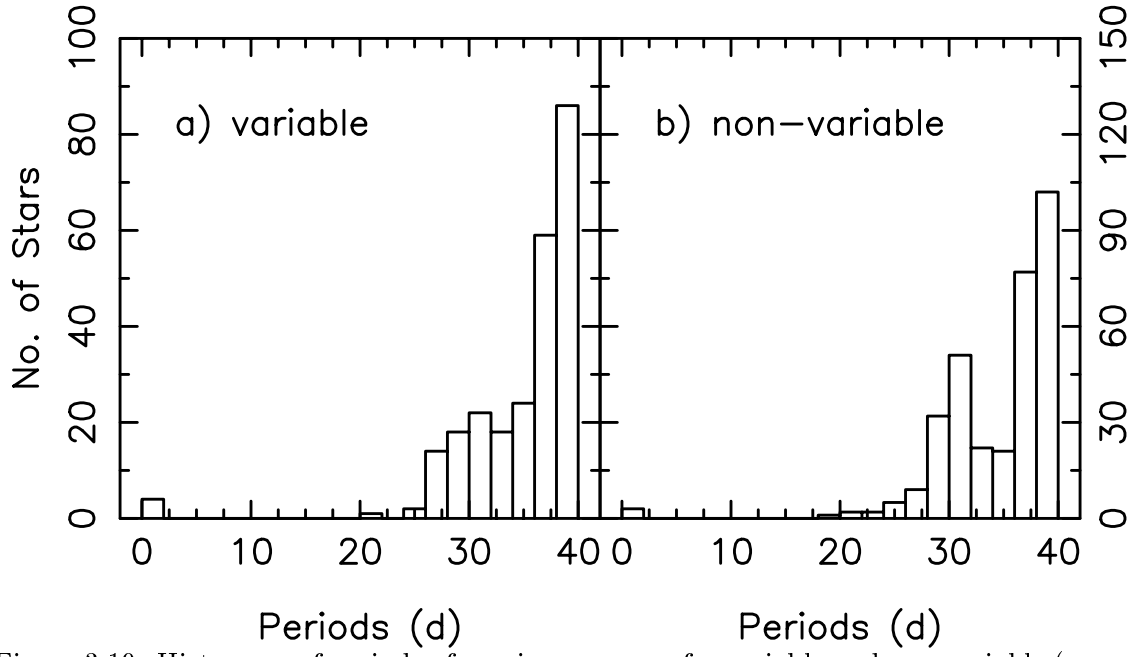


Figure 3.19: Histogram of periods of maximum power for variable and non-variable ($\alpha_v < 1.0$) stars in NGC 7789. Note the differing Y scales.

The individual power spectra did yield one interesting star, star 3105. Figure 3.20 shows this star's power spectrum and data window power spectrum. Star 3105 has $V = 14.6270$ and $B - V = 0.620$. Searching for periods in the nightly mean differential magnitude data around the peaks in the power spectrum yields a period of 19.688 d. When the BVI data are phased to this period, the result is a low-amplitude periodic light curve shown in Figure 3.21.

What could cause this small, periodic brightness change? Star 3105 is likely to be a binary star. The magnitude change could be due to the reflection of the companion upon each star. Assuming that the de-reddened color of each star is $B - V \sim 0.4$ and

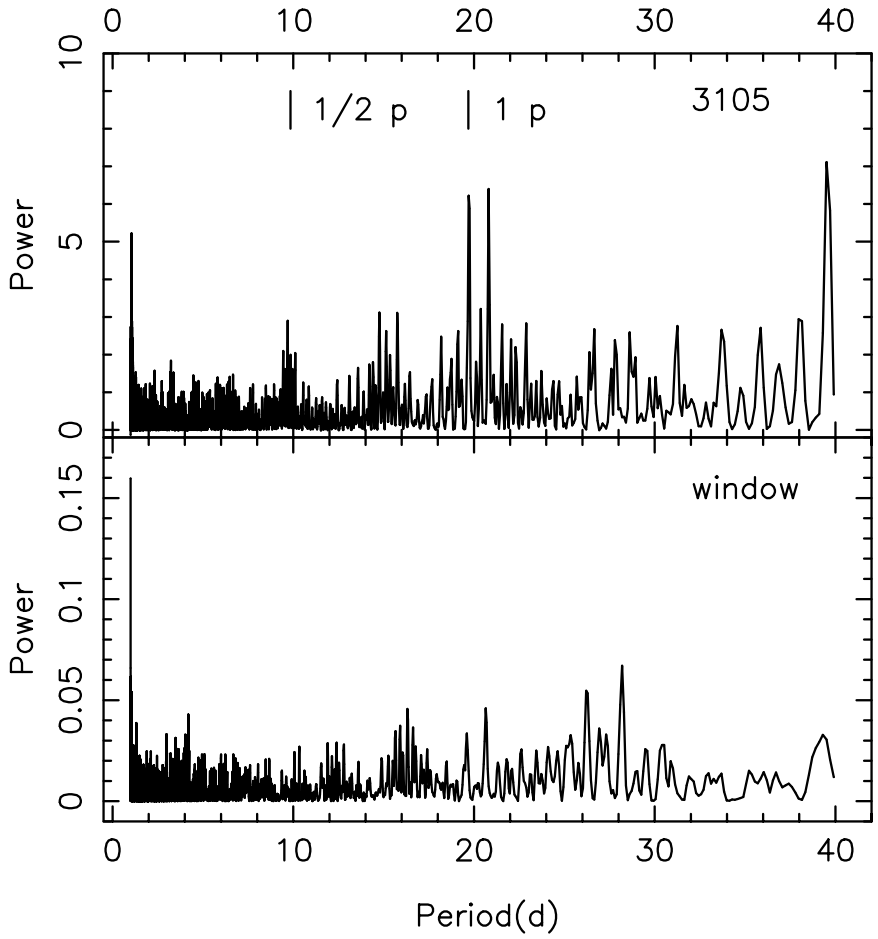


Figure 3.20: Power spectrum for Star 3105, $V = 14.270$ and $B - V = 0.620$. The locations of the period and half of the period are marked. Note the differing Y scales.

the distance is 2.75 kpc, each star is approximately type F2. Assuming that the binary system is composed of two stars of mass $1.5 M_{\odot}$ and a period of 19.688 d, then the distance between the components is $\sim 0.2$ AU. Further assuming for simplicity that one half of each star is heated and the other half is "cold", a temperature change of 0.12% is required to change the total brightness by 10 mmag in V. In an F2 star, this means an increase of 8 K to the photospheric temperature of $\sim 6890$ K. Each star receives 0.03% of the flux from the other star, or $5.33 \times 10^{23}$ W. Obviously one entire hemisphere of each star will not be uniformly heated by the other star, and this smaller size of the heated area will require a larger temperature difference to produce the same brightness change. This scenario is the

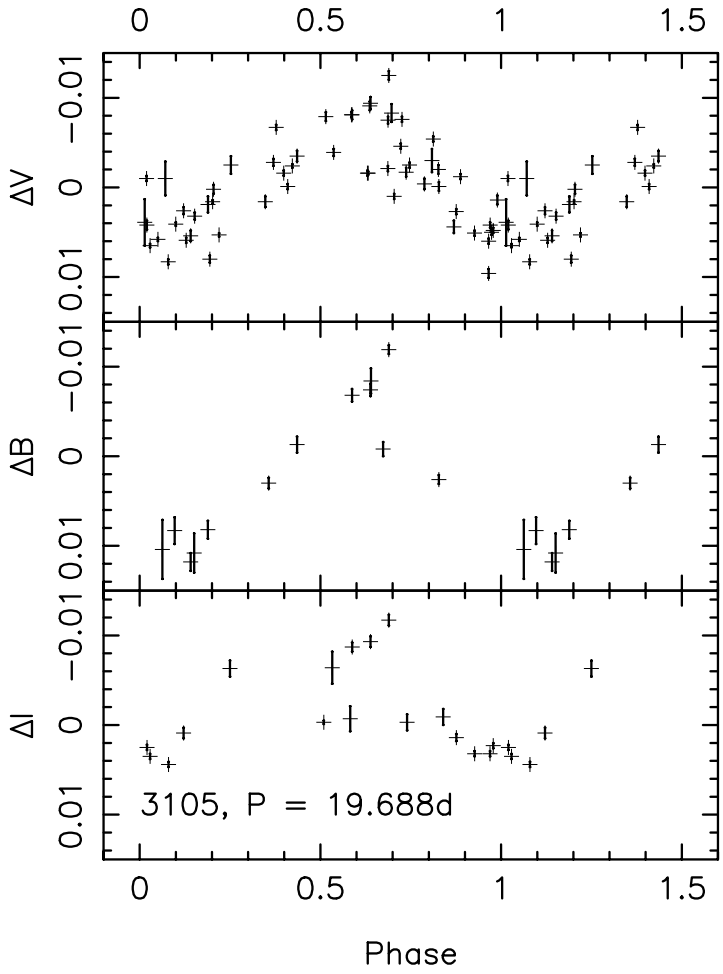


Figure 3.21: Phased BVI nightly mean differential magnitude data for Star 3105 with $P = 19.688d$.

likely explanation for the variability of Star 3105.

### 3.3.4 Solar Analogs

The main thrust of the search for stellar activity is to determine the range of behavior of Sun-like stars so that we can better understand the Sun's behavior. At the distance of NGC 7789 solar-type stars will be approximately $17^{th}$ magnitude in V. We have selected all stars with $17.0 < V < 17.5$ and $0.8 < B - V < 1.1$ that have been observed at least fifty nights through the V filter. Figures 3.22 and 3.23 show the nightly mean V magnitude data for these stars; an arrow indicates the direction of a point that is off the plot. The

day number starts from our first night of observations in August 1996 and runs through October 2001. The stars are numbered according to an internal analysis scheme and are ordered by their significance index. Information about the stars, such as V magnitude and color, may be found in Table 3.8. The table also includes the activity index for the nightly mean differential magnitudes through each filter.

| Star | V | B-V | $\alpha_v$ | r | 99%? | # V | $A_v$ | $A_b$ | $A_i$ |
|---|---|---|---|---|---|---|---|---|---|
| 2930 | 17.398 | 0.977 | 1.73 | 0.71 | Y | 58 | 11.8 | 38.8 | 7.4 |
| 3245 | 17.297 | 0.915 | 1.74 | 0.61 | Y | 58 | 7.6 | 12.4 | 11.8 |
| 3467 | 17.132 | 0.954 | 1.83 | 0.31 | Y | 58 | 7.2 | 15.6 | 7.8 |
| 2486 | 17.350 | 0.938 | 1.93 | 0.68 | Y | 58 | 9.2 | 22.4 | 9.0 |
| 2959 | 17.346 | 0.942 | 2.14 | 0.70 | Y | 58 | 16.8 | 29.8 | 7.3 |
| 2899 | 17.268 | 0.829 | 2.17 | 0.59 | Y | 50 | 10.0 | 17.7 | 6.5 |
| 2915 | 17.252 | 0.933 | 2.59 | 0.84 | Y | 54 | 12.3 | 29.5 | 12.0 |
| 2235* | 17.206 | 0.952 | 3.10 | 0.67 | Y | 56 | 13.6 | 25.1 | 15.2 |
| 2627* | 17.265 | 0.929 | 3.28 | 0.77 | Y | 58 | 13.2 | 36.8 | 30.8 |
| 2732* | 17.335 | 0.938 | 3.43 | 0.87 | Y | 58 | 21.0 | 46.7 | 19.8 |
| 2840* | 17.044 | 1.021 | 5.05 | 0.77 | Y | 57 | 20.1 | 24.3 | 15.8 |
| 2437 | 17.428 | 0.971 | 5.09 | -0.36 | Y | 58 | 21.6 | 10.1 | 5.7 |
| 2965* | 17.369 | 0.901 | 5.74 | 0.83 | Y | 58 | 29.4 | 80.7 | 31.0 |
| 3033* | 17.361 | 0.838 | 6.11 | 0.53 | Y | 58 | 59.4 | 40.4 | 23.0 |

Table 3.8: Solar analogs in NGC 7789. Solar analogs are plotted in Figures 3.22 and 3.23. An asterisk on the star number designates an active star. $\alpha_v$ is the significance index. $r$ is the correlation coefficient, and the "99%?" column indicates whether or not the correlation is significant at the 99% level. Columns 7 lists the number of nights on which the star was observed through the V filter. (All stars have thirteen nights of observations in the B filter, except 2930 and 2915, which have twelve, and 2899, which has nine. All stars have eighteen nights of observations through the I filter, except 2899, which has sixteen). The last three columns are the activity indices of the mean nightly differential magnitudes through each filter in mmags.

These solar analog stars have all been observed over six seasons; many of them display behavior similar to the solar cycle, with comparable brightness changes, although some stars, such as 3467, show almost no variations over six seasons. Many other stars show trends up or down by small but apparently significant amounts. The range of activity seen in these stars is similar to that seen by Baliunas et al. (1995) in nearby solar-type stars in Mt. Wilson Ca II H and K data. The 1998 - 1999 observing season (the cluster of observations around day 750) appears to be of lower quality than the other seasons for

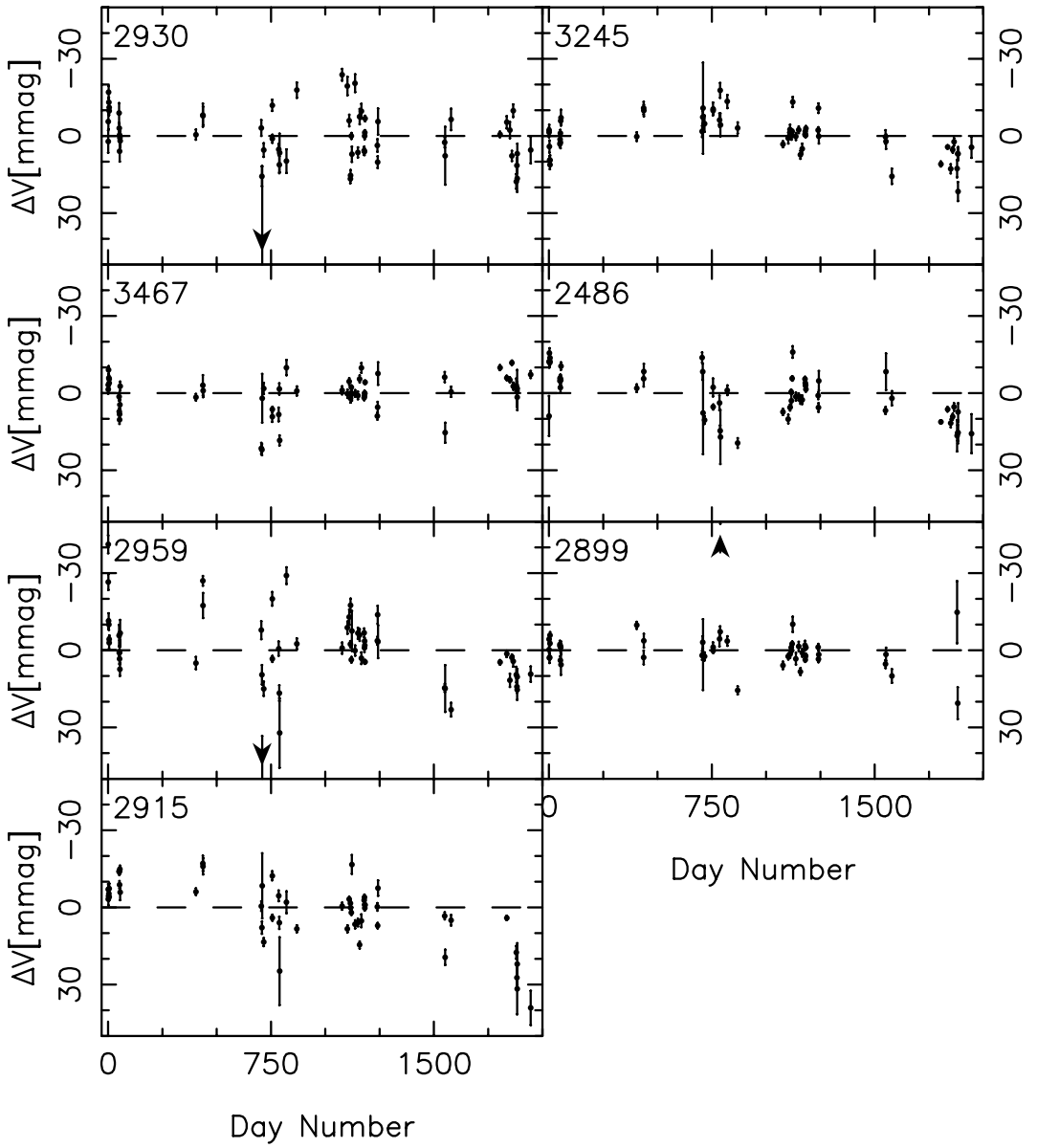


Figure 3.22: Solar analogs with $17.0 < V < 17.5$ in NGC 7789 for individual stars. Stars are ordered by increasing significance index. Star properties are listed in Table 3.8. Units on y-axis are millimagnitudes. Error bars are included on all points. An arrow indicates where a point falls off the plot. More solar analogs are displayed in Figure 3.23.

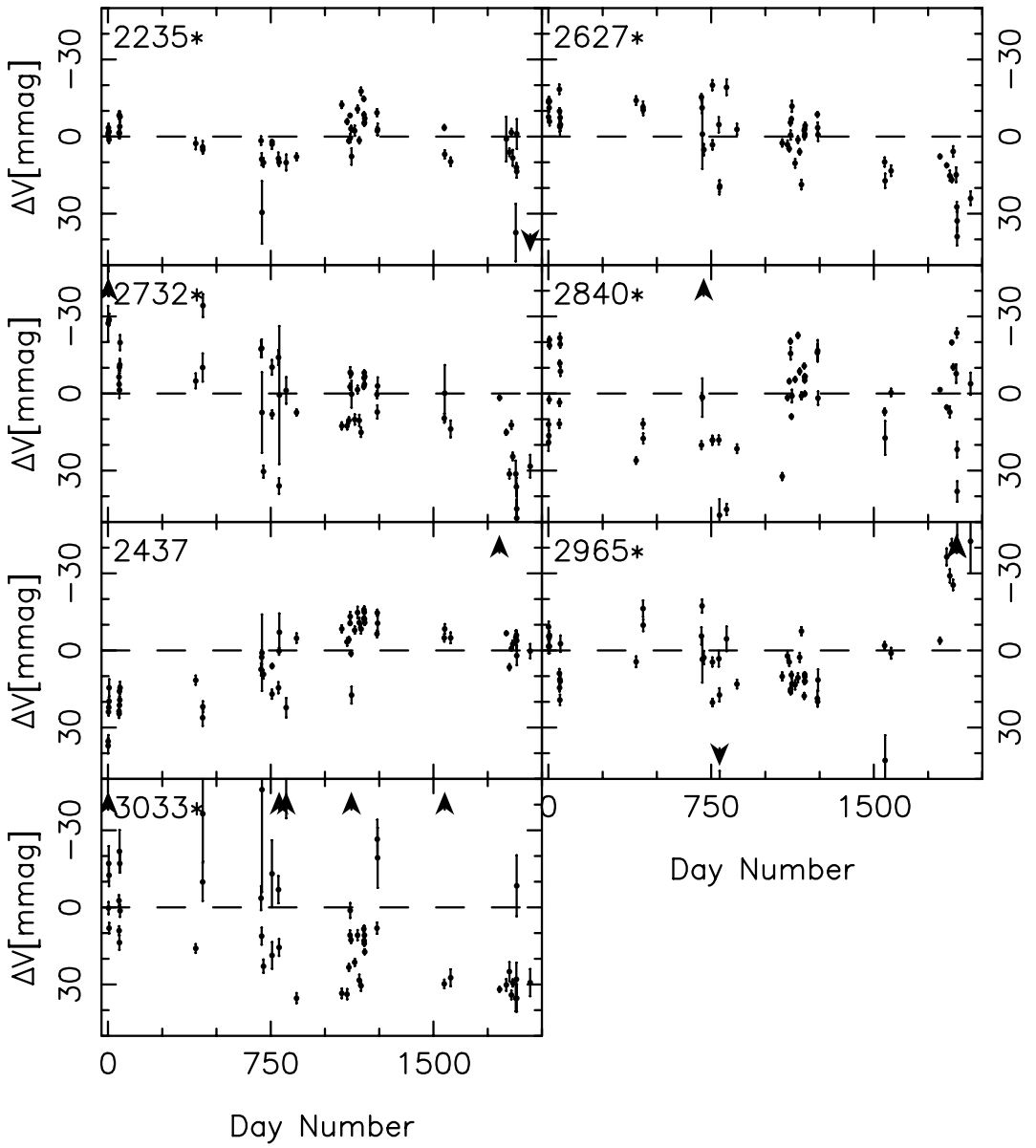


Figure 3.23: Solar analogs with $17.0 < V < 17.5$ in NGC 7789 for individual stars, continued from Figure 3.22. Stars are ordered by increasing significance index. Star properties are listed in Table 3.8. Units on y-axis are millimagnitudes. Error bars are included on all points. An arrow indicates where a point falls off the plot. An asterisk designates an active star.

an undetermined reason.

The combined nightly BVI data are shown for a selection of stars in Figure 3.24. These stars are among those that show the best correlation among the three colors and also give a sampling of inactive and active stars, according to our $\alpha_v$ and $r$ criteria. Stars 3467 and 2486 show few fluctuations and no trend over the nearly 2000-night timescale of our observations. Star 2732 shows a substantial downward trend in over the six seasons which is well-correlated between the three colors. The trend could be part of a solar-cycle-type variation. The B data have noticeably larger errors; fewer B observations were made each night and the stars are fainter in B. Even though the errors are substantial, the B data are well-correlated with V and I and confirm the long-term trend in star 2732.

In Figures 3.22 and 3.23 the nightly mean differential V magnitudes at approximately 750 days appear more scattered than the rest of the magnitudes. These data correspond to observations taken during 1998 and January 1999. The higher amplitude of the scatter could cause some stars to be falsely identified as active. I tested this by removing the 1998 and January 1999 data and re-doing our analysis, beginning from the ensemble photometry stage. Instead of finding that fewer stars are active in the revised data set, I found that 84 of the main sequence stars are active – four more than when the entire data set was used. Clearly, if the data in 1998 and January 1999 are more scattered, the magnitude errors are also larger, so that the stars are not selected incorrectly as active.

### 3.3.5 Activity Index for Annual Mean Differential Magnitudes

The ensemble photometry program also calculated the annual mean differential magnitudes for each star in a manner analogous to the nightly mean differential magnitudes. The Phase I data consist as many as six seasons of data for the V filter, with many frames and several nights of data each year for some stars. The composite record of the Sun's irradiance (from the HF, ACRIM I and II, ERBS, and VIRGO experiments), shows that the Sun's irradiance changes by about 0.1%, or 1 mmag, during the solar cycle (Frohlich &

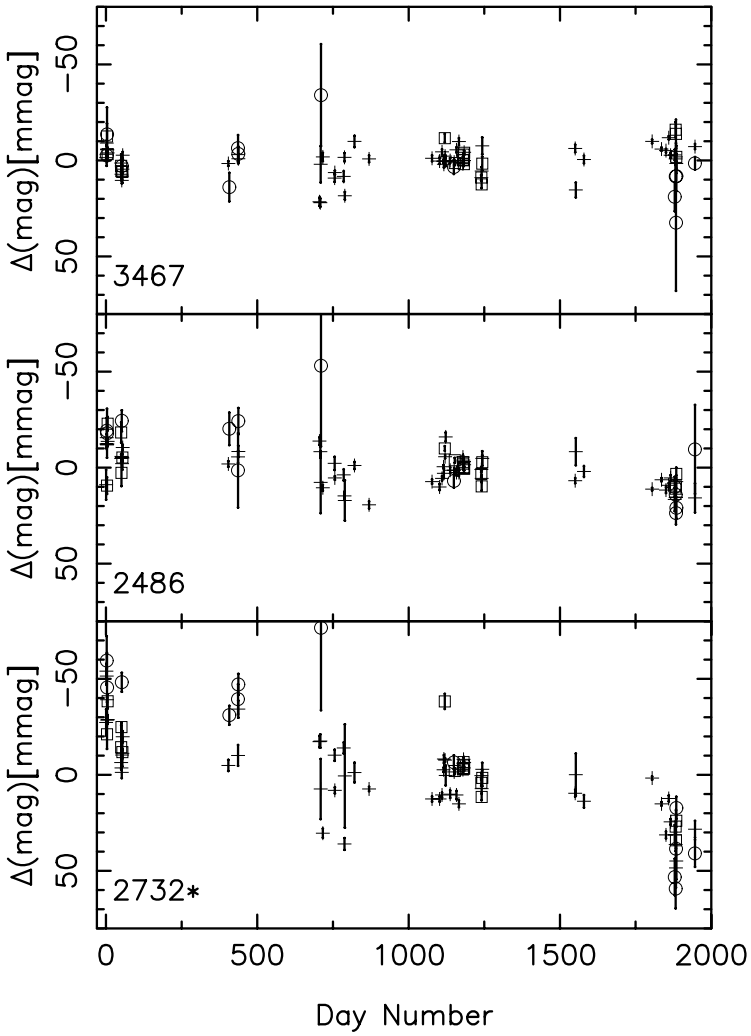


Figure 3.24: Nightly mean BVI data for selected stars in NGC 7789. Properties of each star are listed in Table 3.8. The crosses are V data, the circles are B data, and the boxes are I data. Y-axis units are in millimagnitudes. Error bars are included on all points. An arrow indicates where a point falls of the plot. An asterisk designates an active star.

Lean 1998). Because the nightly mean errors of the better-observed stars in our NGC 7789 data are in a similar range, I could see solar-cycle-type variations in some of the cluster stars.

I calculated the activity index for the yearly mean differential magnitudes in a similar manner to that used for the nightly mean differential magnitudes. I required that each star have at least three years of observations in order to be included in the analysis. The calculation of the activity index using the annual mean differential magnitudes and

comparing the index to its error yielded over 3000 stars, approximately 1550 of which fall on the main sequence. Of these, over 800 stars are candidate variable stars, with $\alpha_v \geq 3$ for the annual means. When I calculate the correlation coefficient of the main sequence stars, requiring at least five pairs of observations through B, V, or I in the same season, 33 stars were found to be both candidate variable stars and to be correlated in color at a 99% significance level; these stars are active. Figure 3.25 shows the color-magnitude diagram of these stars; the crosses are the active stars. A handful of these stars appear to be a binaries, and two are well below the main sequence proper, but within our error criterion for main sequence stars.

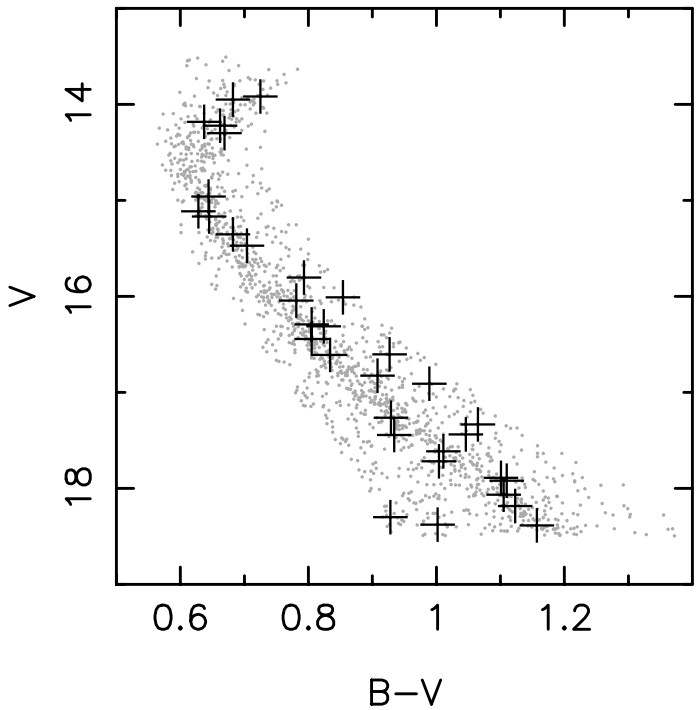


Figure 3.25: Color-magnitude diagram for annual means of stars in NGC 7789. The gray dots are all of the main sequence stars with at least five years' observations through the V filter. The crosses are the stars found to be variable.

Figure 3.26 shows the annual mean V magnitudes plotted versus the annual mean B or I magnitudes. The left panel shows all main sequence stars, and the right panel shows the

variable stars. The main sequence stars show a large amount of scatter. However, in the plot of the variable stars, the positive correlation is clearly seen, even at the 10 mmag level. These 33 active stars out of approximately 1150 main sequence stars constitute 3% of the main sequence population; this percentage is smaller than the number of main sequence stars found to be active in the nightly data. Figure 3.27 plots the V, B, and I annual mean differential magnitudes for fifteen of the stars with six seasons of observations and the highest significance index. Brighter stars, such as 2739 and 2377 show small fluctuations that are very well-correlated between colors. Fainter stars, such as 2323 and 2348 show larger fluctuations in all colors. Table 3.9 lists the properties of these stars as well as their significance indices.

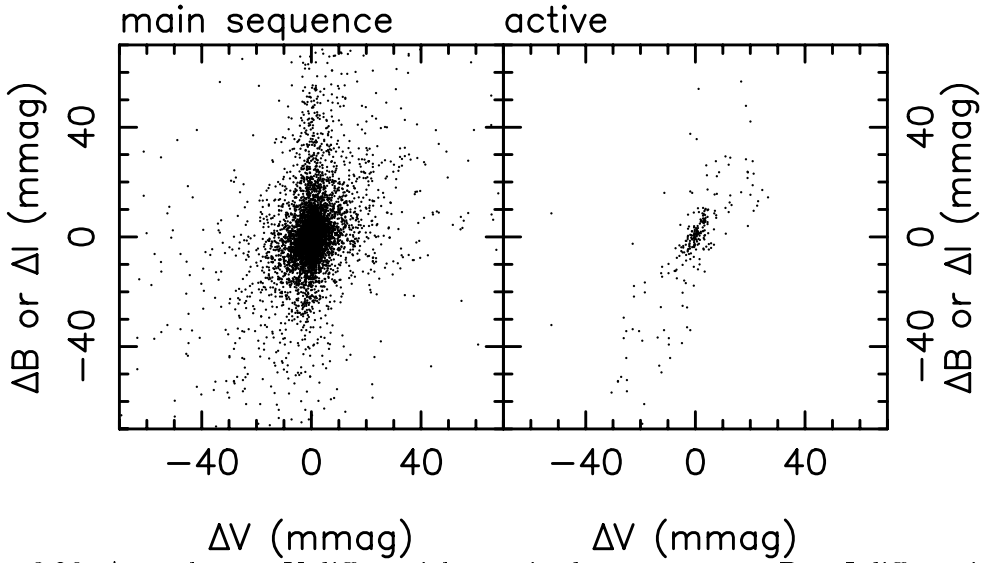


Figure 3.26: Annual mean V differential magnitudes versus mean B or I differential magnitudes for the main sequence stars in the left panel and for the 33 stars found to be active in the right panel.

### 3.3.6 Summary

I have developed an activity index which calculates the amplitude of the brightness fluctuations of each star. I then compare the activity index to its error to compute the significance index of each star; a star with $\alpha_v \geq 3$ is considered a candidate variable star.

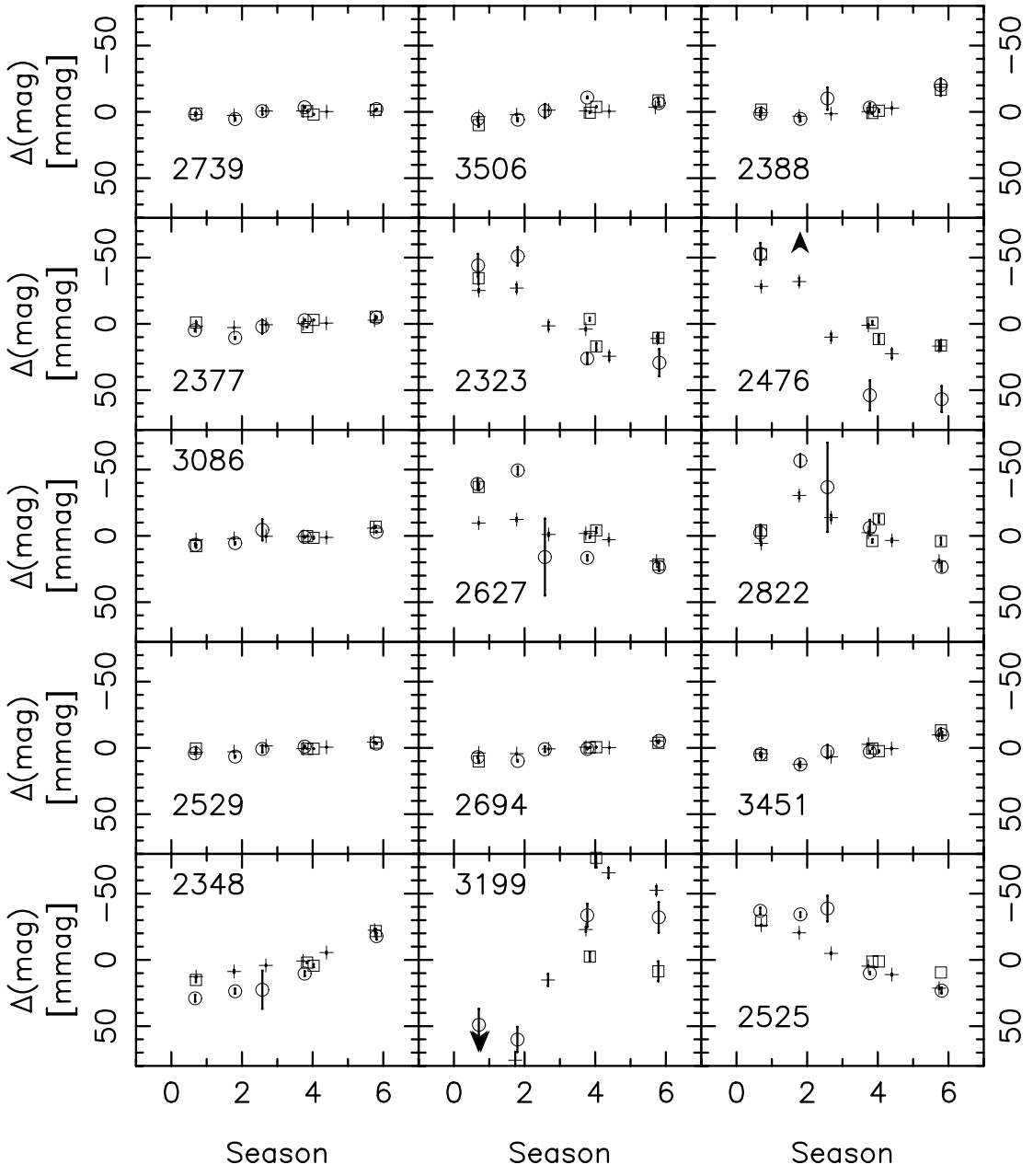


Figure 3.27: Annual mean V, B, and I differential magnitudes versus season for fifteen of the stars with six seasons of V observations and the highest significance index. The stars are ordered by increasing significance index. Crosses represent V, circles are B, and squares are I. Error bars are also plotted. Season 0 is 1996, and thus season 6 is 2001. Parameters about the stars can be found in Table 3.9.

| Star | V | B-V | $\alpha_v$ | $r$ | $A_v$ | $A_b$ | $A_i$ |
|---|---|---|---|---|---|---|---|
| 2739 | 13.919 | 0.725 | 6.89 | 0.81 | 1.4 | 3.2 | 1.4 |
| 3506 | 15.169 | 0.645 | 7.52 | 0.85 | 2.3 | 6.8 | 6.9 |
| 2388 | 16.312 | 0.824 | 7.55 | 0.87 | 7.7 | 10.5 | 8.4 |
| 2377 | 14.182 | 0.637 | 7.87 | 0.84 | 1.8 | 5.8 | 3.3 |
| 2323 | 18.377 | 1.002 | 7.93 | 0.92 | 18.7 | 39.0 | 20.0 |
| 2476 | 18.386 | 1.157 | 8.23 | 0.85 | 21.2 | 69.4 | 28.1 |
| 3086 | 14.960 | 0.655 | 8.25 | 0.82 | 2.8 | 4.6 | 5.3 |
| 2627 | 17.265 | 0.929 | 9.65 | 0.82 | 10.2 | 31.8 | 21.5 |
| 2822 | 17.613 | 1.011 | 10.19 | 0.92 | 16.0 | 32.1 | 7.2 |
| 2529 | 14.222 | 0.662 | 10.25 | 0.82 | 2.6 | 3.8 | 2.0 |
| 2694 | 13.949 | 0.682 | 11.15 | 0.95 | 3.2 | 5.9 | 5.5 |
| 3451 | 16.009 | 0.854 | 11.97 | 0.93 | 7.3 | 7.6 | 7.2 |
| 2348 | 16.445 | 0.805 | 15.09 | 0.95 | 11.5 | 21.6 | 13.5 |
| 3199 | 18.183 | 1.123 | 18.55 | 0.85 | 88.9 | 45.2 | 96.2 |
| 2525 | 16.605 | 0.927 | 26.96 | 0.89 | 17.0 | 30.6 | 15.5 |

Table 3.9: Fifteen of the variables found by analyzing their annual mean differential data and plotted in Figure 3.27. $\alpha_v$ is the significance index based on the annual mean differential magnitudes, and $r$ is the correlation coefficient. The last three columns are the activity indices calculated through each filter. All stars have six seasons in V and four in I. Stars 2323, 2476, and 3199 have four seasons in B, while the rest of the stars have five.

I have also calculated a linear correlation coefficient for each star with at least five pairs of observations with B and V or V and I on a night and chose those stars whose correlation coefficients are significant at a 99% level. Stars which are both variable and significantly positively correlated are deemed variable, and as the stars of interest, "active". These tests demonstrate that I am in fact observing the effects of physical processes on the stars. When I look at stars similar to the Sun, I see behavior on nightly and yearly timescales that closely resembles that seen from nearby solar type stars in the Mt. Wilson HK Project.

The variability I am searching for is at the limit of detection with the current data. The B data suffer from low count rates. The I data have larger than expected errors, probably due to flat fielding problems, including possible night-sky fringing. To resolve these problems, future observing campaigns will concentrate on the BVR filters, with an emphasis on taking well-exposed images in the B filter.

## 3.4 Phase I Results for NGC 6819, M67 and NGC 188

The analysis of the Phase I data for the other three clusters (NGC 6819, M67, and NGC 188) follows the same procedure as described above for NGC 7789. I will make some brief comments on the few differences in the analysis of each cluster, and then present the equivalent figures. For comparison, I will also include the figures from NGC 7789.

### 3.4.1 NGC 6819

The data reduction for the NGC 6819 observations proceeded in a manner similar to that of the NGC 7789 observations. Examination of a preliminary V magnitude check file led to the elimination of the nights UT 2000 Sep 21, UT 2000 Oct 12, and UT 2001 Jul 15 - 18. All of these nights were noted as possibly having fluctuating levels of cloudiness. Once these data were removed, *diffmag* was run again on the remaining data. Figure 3.28 shows a plot of the check file, which is very similar to the check file for NGC 7789 in Figure 3.8. For NGC 6819 we did not eliminate the data taken with the Navy CCD; the median magnitudes for the two usable nights with this CCD can be seen around frame 450 and 730. I also did not eliminate the data taken with the Loral1 CCD; these data can be seen from roughly frame 870 to 1015. While some of these data are somewhat elevated in their median differential magnitudes, they are still within $\sim$10 mmag of the majority of the data. Similarly, in the I data, nights UT 2001 Jul 15 and UT 2001 Oct 16 were removed; the former due to the aforementioned clouds, and the latter due to problems with condensation on the CCD that affected the I data more severely than the B and V. No usable nights were eliminated in the B filter. A log of the observations used in the analysis is in Table 3.10.

### 3.4.2 M67

The data reduction for the M67 observations proceeded in a manner similar to that of the previous clusters' observations. Examination of the V magnitude check file led to the

| Telescope | Dates (UT) | CCD | Usable Nights | Objects | Filters |
|---|---|---|---|---|---|
| MLO | 1996 Aug 18-24 | Loral | 7 | 1, 2, 4 | BVI |
| MLO | 1996 Oct 8-13 | Loral | 6 | 1, 2, 3, 4 | BVI |
| MLO | 1997 Sep 27-30 | Loral | 4 | 1, 2, 4 | UBV |
| MLO | 1998 Jul 24-31 | Loral | 6 | 1, 2, 4, 5 | BVI |
| Perkins | 1998 Aug 3-6 | SITe | 4 | 1, 2, 5 | BV |
| MLO | 1998 Sep 11-14 | Loral | 4 | 1, 2 | V |
| Perkins | 1998 Sep 12-15 | SITe | 2 | 1, 2, 5 | UV |
| MLO | 1998 Oct 13-15 | Loral | 3 | 1, 2, 3, 4, 5 | VR |
| Perkins | 1998 Oct 16-21 | SITe | 6 | 1, 2, 3, 4, 5 | UVR |
| Perkins(Q) | 1998 Nov 21-23 | Navy | 2 | 1, 2, 3, 4 | VI |
| Perkins | 1999 May 17-24 | SITe | 4 | 2, 5 | VRI |
| Perkins(Q) | 1999 Jun 1-3 | SITe | 2 | 2 | V |
| Perkins(Q) | 1999 Jun 24-25 | SITe | 1 | 2 | V |
| Perkins(Q) | 1999 Jul 2-4 | SITe | 2 | 2, 5 | V |
| Perkins(Q) | 1999 Aug 1-2 | SITe | 1 | 1, 2 | V |
| Perkins(Q) | 1999 Aug 26-27 | SITe | 2 | 1, 2, 4 | V |
| Perkins(Q) | 1999 Sep 3 | SITe | 1 | 1, 2, 4 | V |
| Perkins | 1999 Sep 8-14 | SITe | 4 | 1, 2, 4 | V |
| MLO | 1999 Sep 12-15 | Loral | 3 | 1, 2, 4, 5 | VI |
| Perkins(Q) | 1999 Sep 30 | SITe | 1 | 1, 2, 4 | V |
| Perkins | 1999 Oct 11-15 | SITe | 5 | 1, 2, 3, 4, 5 | UBVRI |
| Perkins(Q) | 1999 Oct 21 | SITe | 1 | 1, 2, 3, 4 | V |
| Perkins(Q) | 1999 Oct 29 | SITe | 1 | 1, 2, 3, 4 | V |
| Perkins | 1999 Nov 3-5 | Navy | 1 | 1, 2, 4 | V |
| Perkins | 1999 Nov 11-15 | SITe | 5 | 1, 2, 3, 4, 5 | VI |
| Perkins(Q) | 2000 May 3 | Loral1 | 1 | 2, 3 | V |
| Perkins | 2000 Jun 27 - Jul 3 | Loral1 | 1 | 2 | BVI |
| Perkins(Q) | 2000 Jul 11 | Loral1 | 1 | 1, 2, 5 | V |
| Perkins(Q) | 2000 Jul 18 | Loral1 | 1 | 1, 2, 5 | V |
| Perkins(Q) | 2000 Jul 24 | Loral1 | 1 | 2, 5 | V |
| Perkins(Q) | 2000 Sep 12 | Loral1 | 1 | 1, 2, 4, 5 | VI |
| Perkins | 2000 Sep 19-26 | Loral1 | 4 | 1, 2, 4, 5 | UV |
| Perkins | 2000 Oct 25-30 | Loral1 | 2 | 1, 2, 3, 4, 5 | VR |
| Perkins(Q) | 2000 Nov 16-19 | SITe | 3 | 1, 2, 3, 4, 5 | V |
| Perkins(Q) | 2001 Apr 30 | Loral2 | 1 | 2, 3, 5 | V |
| Perkins | 2001 May 23-29 | Loral2 | 2 | 2, 3, 5 | UVI |
| Perkins | 2001 Jul 14-20 | Loral2 | 7 | 1, 2, 5 | UBRI |
| Perkins(Q) | 2001 Jul 28 | Loral2 | 1 | 1, 2, 5 | VI |
| Perkins | 2001 Aug 22-28 | Loral2 | 7 | 1, 2, 4, 5 | UBV |
| Perkins(Q) | 2001 Sep 11-12 | Loral2 | 2 | 1, 2, 4, 5 | VI |
| Perkins(Q) | 2001 Sep 21 | Loral2 | 1 | 1, 2, 5 | VI |
| Perkins(Q) | 2001 Sep 27 | Loral2 | 1 | 1, 2, 5 | VI |
| Perkins | 2001 Oct 11-16 | Loral2 | 5 | 1, 2, 3, 4, 5 | UBVI |

Table 3.10: Phase I Observations of NGC 6819. "MLO" refers to the 1.0-m Mt. Laguna Observatory telescope. "Perkins" refers to the 1.8-m Perkins Telescope at Lowell Observatory. A Q after the telescope name denotes observations made by the BU Queue observer, as explained in the text. The CCD designations "Loral", "SITe", "Navy", "Loral1", and "Loral2" are explained in the text. The clusters are assigned numbers in order of age: 1 - NGC 7789, 2 - NGC 6819, 3 - M67, 4 - NGC 188.

elimination of all of the data taken using the Navy and Loral1 CCDs for all filters. Night UT 2001 May 24 was discarded for all filters because it was later discovered that the shutter was behaving erratically and not opening for the proper exposure times. Nights UT 2001 Dec 16 - 17 were discarded for all filters due to condensation on the CCD. For the V filter, night UT 1996 Oct 12 was eliminated; no problems or compromising weather conditions were noted for this night, but the median V magnitudes were significantly offset compared to the other nights. Figure 3.28 shows a plot of the check file, with the same scale as the corresponding plots for NGC 7789 and NGC 6819. The median V magnitudes are much lower in M67 than in the previous clusters. A log of the observations used in our analysis is in Table 3.11.

### 3.4.3 NGC 188

The data reduction for NGC 188 proceeded in a similar manner to that of the previous clusters. The data for the reference stars were from Sarajedini (2003), upon which the paper by Sarajedini et al. (1999) was based. Examination of the V magnitude check file led to the elimination of a few images with large deviations: three images from UT 2000 Jan 6 and one from UT 2000 Oct 26. Nights UT 1998 Nov 22-23 were eliminated because of problems with the universal time in the image header. No nights were eliminated from the B and I data. Figure 3.28 shows a plot of the check file, with the same scale as the corresponding plots for the previous three clusters. The median V magnitudes are quite low in NGC 188 compared to the other clusters until about UT 2000 Sep, when the Loral CCDs at the Perkins telescope were used. A log of the observations used in our analysis of NGC 188 is in Table 3.12.

| Telescope | Dates (UT) | CCD | Usable Nights | Objects | Filters |
|---|---|---|---|---|---|
| MLO | 1996 Oct 8-13 | Loral | 5 | 1, 2, 3, 4 | BVI |
| MLO | 1997 Jan 29 - Feb 2 | Loral | 4 | 3, 4 | V |
| MLO | 1998 Jan 22 | Loral | 1 | 3, 4 | V |
| MLO | 1998 Feb 6 | Loral | 1 | 3 | V |
| MLO | 1998 Oct 13-15 | Loral | 3 | 1, 2, 3, 4, 5 | VR |
| Perkins | 1998 Oct 16-21 | SITe | 6 | 1, 2, 3, 4, 5 | UVR |
| Perkins(Q) | 1999 Jan 5-6 | SITe | 1 | 1, 3, 4 | V |
| Perkins(Q) | 1999 Jan 11 | SITe | 1 | 3, 4 | V |
| Perkins(Q) | 1999 Feb 23 | SITe | 1 | 3, 4 | V |
| Perkins | 1999 Mar 5-10 | SITe | 5 | 3, 5 | V |
| Perkins(Q) | 1999 Mar 30 | SITe | 1 | 3 | V |
| Perkins | 1999 Oct 11-15 | SITe | 5 | 1, 2, 3, 4, 5 | UBVRI |
| Perkins(Q) | 1999 Oct 21 | SITe | 1 | 1, 2, 3, 4 | V |
| Perkins(Q) | 1999 Oct 29 | SITe | 1 | 1, 2, 3, 4 | V |
| Perkins | 1999 Nov 11-15 | SITe | 5 | 1, 2, 3, 4, 5 | VI |
| Perkins(Q) | 1999 Nov 21 | SITe | 1 | 1, 3 | V |
| Perkins(Q) | 1999 Dec 1 | SITe | 1 | 3, 4 | V |
| Perkins | 2000 Jan 11-16 | SITe | 6 | 1, 3, 4 | VI |
| Perkins(Q) | 2000 Nov 16-19 | SITe | 3 | 1, 2, 3, 4, 5 | V |
| Perkins(Q) | 2001 Feb 13 | SITe | 1 | 3, 4 | V |
| Perkins(Q) | 2001 Apr 2 | SITe | 1 | 3 | V |
| Perkins(Q) | 2001 Apr 9 | SITe | 1 | 3 | V |
| Perkins(Q) | 2001 Apr 30 | Loral2 | 1 | 2, 3, 5 | V |
| Perkins | 2001 Oct 11-16 | Loral2 | 5 | 1, 2, 3, 4, 5 | UBVI |
| Perkins | 2001 Dec 16-22 | Loral2 | 2 | 1, 3, 4 | BVR |

Table 3.11: Phase I Observations of M67. "MLO" refers to the 1.0-m Mt. Laguna Observatory telescope. "Perkins" refers to the 1.8-m Perkins Telescope at Lowell Observatory. A Q after the telescope name denotes observations made by the BU Queue observer, as explained in the text. The CCD designations "Loral", "SITe", and "Loral2" are explained in the text. The clusters are assigned numbers in order of age: 1 - NGC 7789, 2 - NGC 6819, 3 - M67, 4 - NGC 188.

| Telescope | Dates (UT) | CCD | Usable Nights | Objects | Filters |
|---|---|---|---|---|---|
| MLO | 1996 Aug 18-24 | Loral | 7 | 1, 2, 4 | BVI |
| MLO | 1996 Oct 8-13 | Loral | 6 | 1, 2, 3, 4 | BVI |
| MLO | 1997 Jan 29 - Feb 2 | Loral | 4 | 3, 4 | V |
| MLO | 1997 Sep 27-30 | Loral | 4 | 1, 2, 4 | UBV |
| MLO | 1998 Jan 22 | Loral | 1 | 3, 4 | V |
| MLO | 1998 Jul 24-31 | Loral | 6 | 1, 2, 4, 5 | BVI |
| MLO | 1998 Oct 13-15 | Loral | 3 | 1, 2, 3, 4, 5 | VR |
| Perkins | 1998 Oct 16-21 | SITe | 6 | 1, 2, 3, 4, 5 | UVR |
| Perkins(Q) | 1998 Oct 29 | SITe | 1 | 1, 4 | V |
| Perkins(Q) | 1998 Nov 21-23 | Navy | 2 | 1, 2, 3, 4 | VI |
| Perkins(Q) | 1998 Nov 28 | Navy | 1 | 4 | V |
| Perkins(Q) | 1998 Dec 1-7 | Navy | 4 | 1, 3, 4 | V |
| Perkins(Q) | 1999 Jan 5-6 | SITe | 1 | 1, 3, 4 | V |
| Perkins(Q) | 1999 Jan 11 | SITe | 1 | 3, 4 | V |
| Perkins(Q) | 1999 Feb 23 | SITe | 1 | 3, 4 | V |
| Perkins(Q) | 1999 Aug 26-27 | SITe | 2 | 1, 2, 4 | V |
| Perkins(Q) | 1999 Sep 3 | SITe | 1 | 1, 2, 4 | V |
| Perkins | 1999 Sep 8-14 | SITe | 4 | 1, 2, 4 | V |
| MLO | 1999 Sep 12-15 | Loral | 3 | 1, 2, 4, 5 | VI |
| Perkins(Q) | 1999 Sep 30 | SITe | 1 | 1, 2, 4 | V |
| Perkins | 1999 Oct 11-15 | SITe | 5 | 1, 2, 3, 4, 5 | UBVRI |
| Perkins(Q) | 1999 Oct 21 | SITe | 1 | 1, 2, 3, 4 | V |
| Perkins(Q) | 1999 Oct 29 | SITe | 1 | 1, 2, 3, 4 | V |
| Perkins | 1999 Nov 3-5 | Navy | 1 | 1, 2, 4 | V |
| Perkins | 1999 Nov 11-15 | SITe | 5 | 1, 2, 3, 4, 5 | VI |
| Perkins(Q) | 1999 Dec 1 | SITe | 1 | 3, 4 | V |
| Perkins | 2000 Jan 11-16 | SITe | 6 | 1, 3, 4 | VI |
| Perkins(Q) | 2000 Sep 12 | Loral1 | 1 | 1, 2, 4, 5 | VI |
| Perkins | 2000 Sep 19-26 | Loral1 | 5 | 1, 2, 4, 5 | UV |
| Perkins(Q) | 2000 Oct 3 | Loral1 | 1 | 1, 4 | V |
| Perkins | 2000 Oct 25-30 | Loral1 | 2 | 1, 2, 3, 4, 5 | VR |
| Perkins(Q) | 2000 Nov 9 | Loral1 | 1 | 1, 4 | V |
| Perkins(Q) | 2000 Nov 16-19 | SITe | 3 | 1, 2, 3, 4, 5 | V |
| Perkins(Q) | 2001 Jan 21 | Navy | 1 | 1, 3, 4 | V |
| Perkins(Q) | 2001 Jan 26 | Navy | 1 | 1, 3, 4 | V |
| Perkins(Q) | 2001 Jan 31 | Navy | 1 | 1, 3, 4 | V |
| Perkins(Q) | 2001 Feb 13 | SITe | 1 | 3, 4 | V |
| Perkins | 2001 Aug 22-28 | Loral2 | 7 | 1, 2, 4, 5 | UBV |
| Perkins(Q) | 2001 Sep 11-12 | Loral2 | 2 | 1, 2, 4, 5 | VI |
| Perkins | 2001 Oct 11-16 | Loral2 | 5 | 1, 2, 3, 4, 5 | UBVI |
| Perkins | 2001 Dec 16-22 | Loral2 Navy | 4 | 1, 3, 4 | BVR |

Table 3.12: Phase I Observations of NGC 188. "MLO" refers to the 1.0-m Mt. Laguna Observatory telescope. "Perkins" refers to the 1.8-m Perkins Telescope at Lowell Observatory. A Q after the telescope name denotes observations made by the BU Queue observer, as explained in the text. The CCD designations "Loral", "SITe", and "Loral2" are explained in the text. The clusters are assigned numbers in order of age: 1 - NGC 7789, 2 - NGC 6819, 3 - M67, 4 - NGC 188.

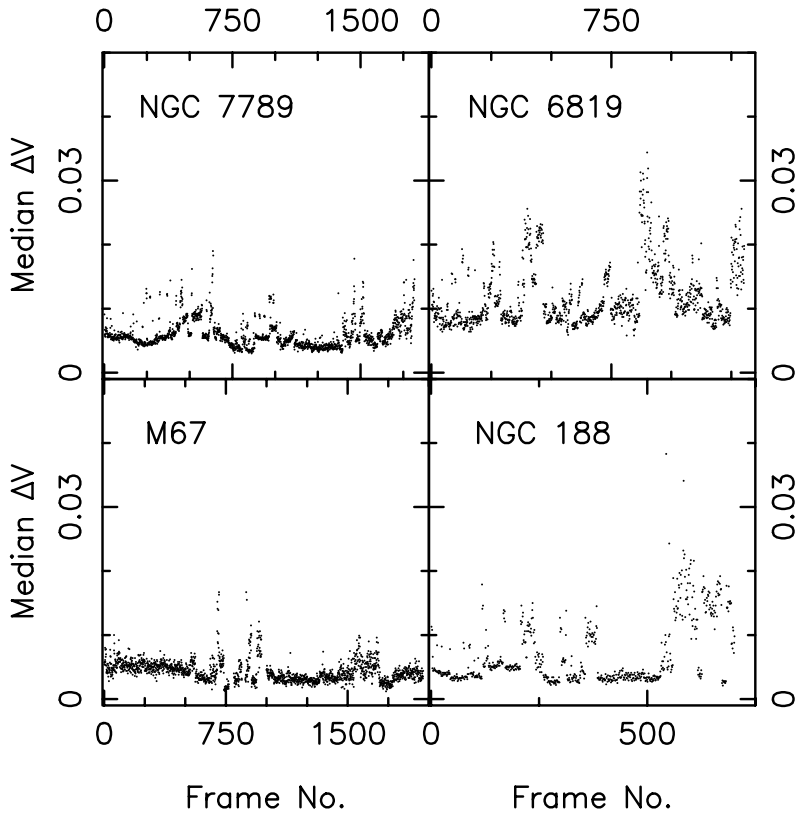


Figure 3.28: Differential ensemble photometry re-check. The x-axis numbers all the frames taken of each cluster. The y-axis is the median V differential magnitude for each frame. These plots contain only the images used in the subsequent analysis; some data have been discarded due to high offsets from the other data, as listed in the text.

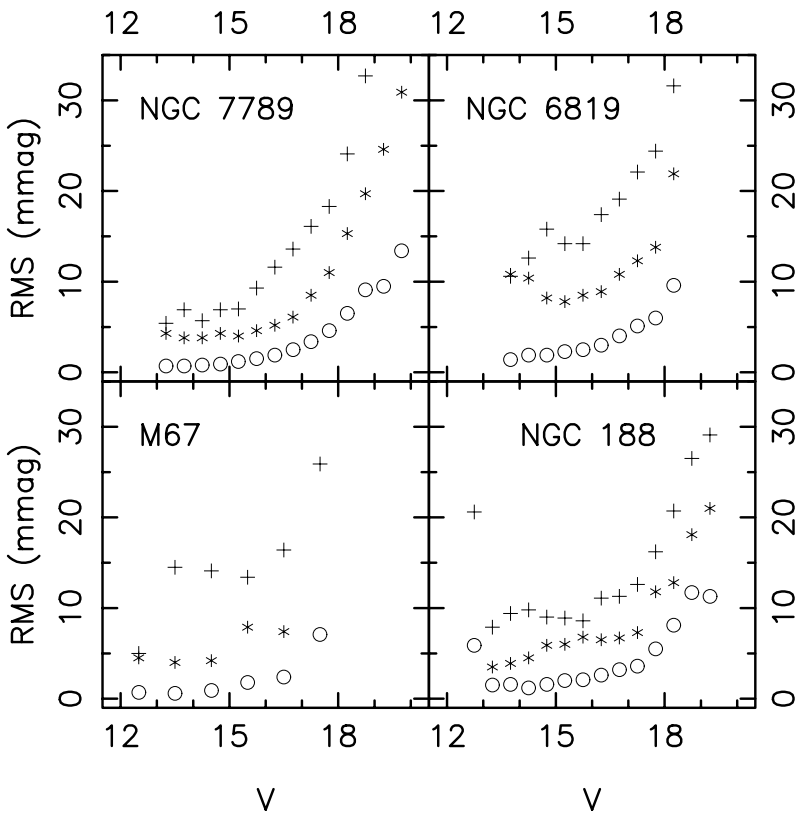


Figure 3.29: V magnitude versus the median value of $\sigma_{rms}$, $\sigma_{mean}$, and $\sigma_{phot}$ for the clusters indicated. In all plots, the crosses are $\sigma_{phot}$, asterisks are $\sigma_{rms}$ and the circles are $\sigma_{mean}$. The offset between $\sigma_{rms}$ and $\sigma_{mean}$ for bright stars was used to determine the ensemble error for each cluster. The ensemble error for NGC 7789 is found to be 3 mmag; the error for NGC 6819 is 6 mmag, 2.5 mmag for M67, and 4 mmag for NGC 188.

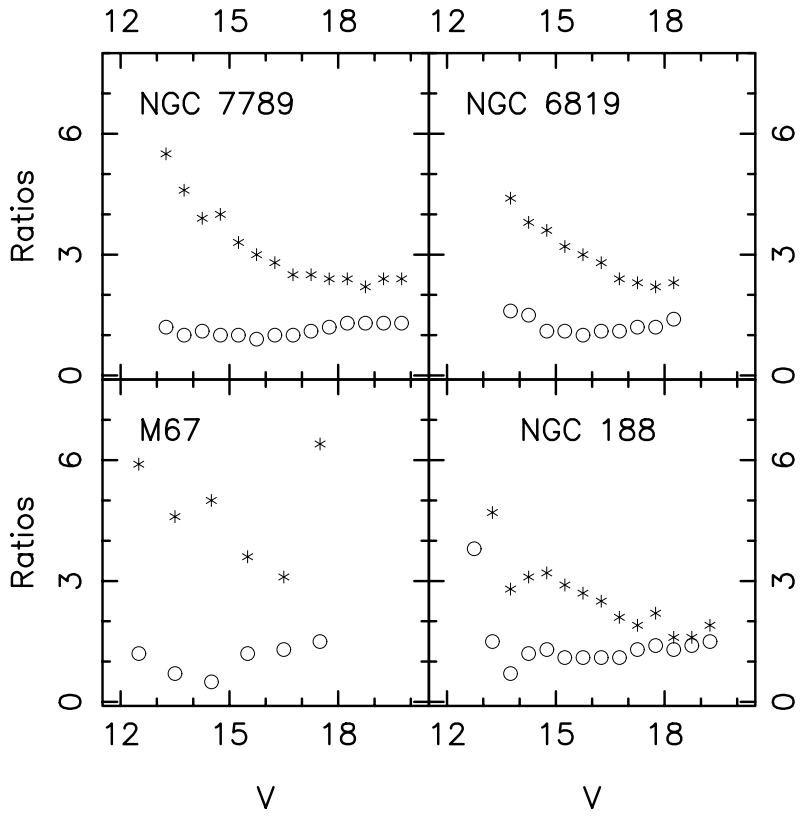


Figure 3.30: Plot of the ratios $\sigma_f/\sigma_{phot}$ (circles) and $\sigma_{rms}/\sigma_{mean}$ (asterisks) for the clusters indicated. The plotted points are the medians of the bins; since there are few stars in some of the bins, the ratios are more biased by a few extreme points, especially in M67. Nevertheless, the ratio $\sigma_f/\sigma_{phot}$ is approximately one, indicating the estimated photometric errors from SPS and *diffmag* are similar to the actual RMS of the differential magnitudes of each star.

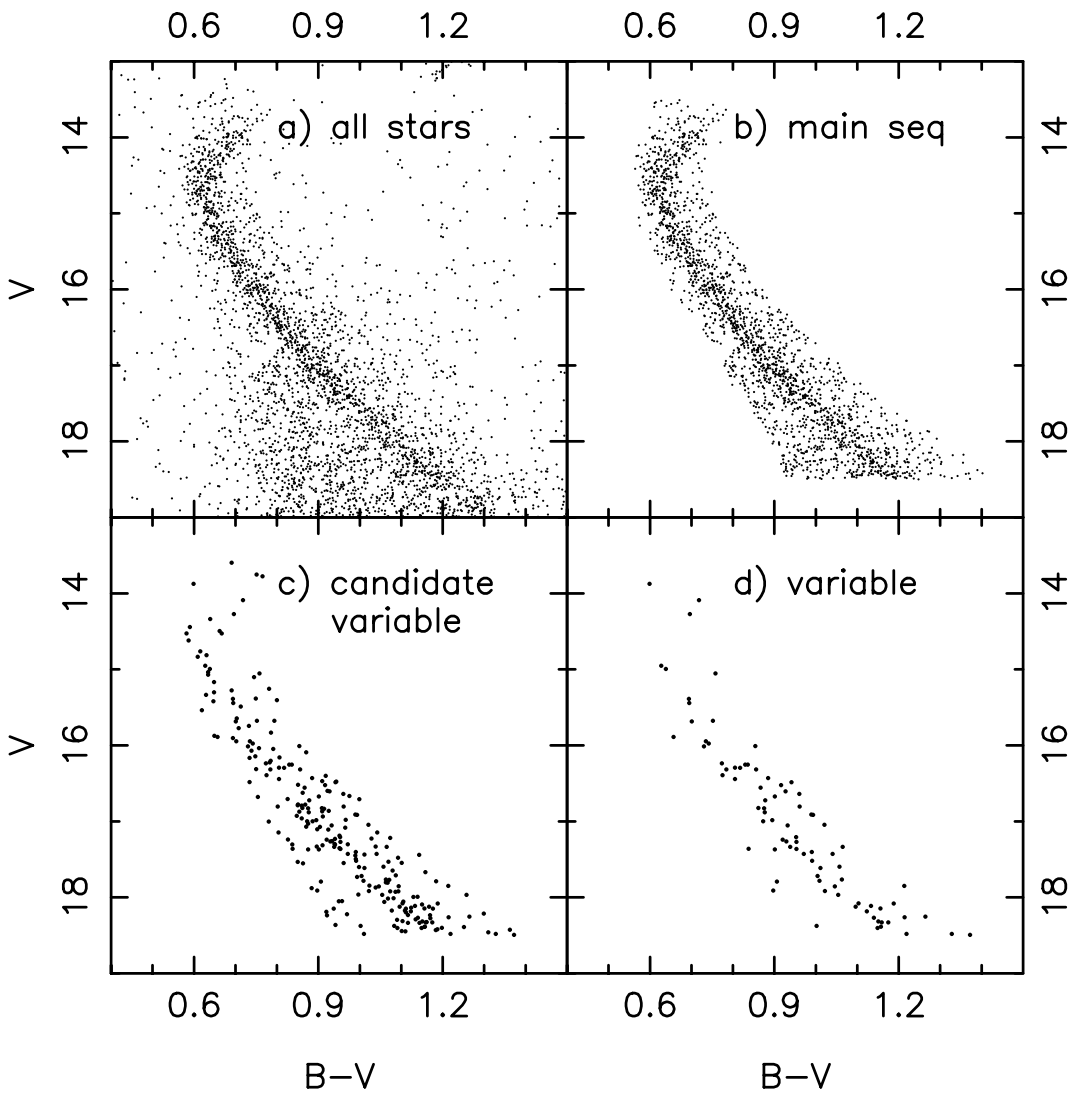


Figure 3.31: Color-magnitude diagrams for NGC 7789. Panel a shows all stars observed. Panel b shows the stars photometrically chosen as the main sequence. Panel c shows the candidate variable stars. Panel d shows the variable stars, with $\alpha_v \geq 3$ and whose colors are correlated at a 99% significant level.

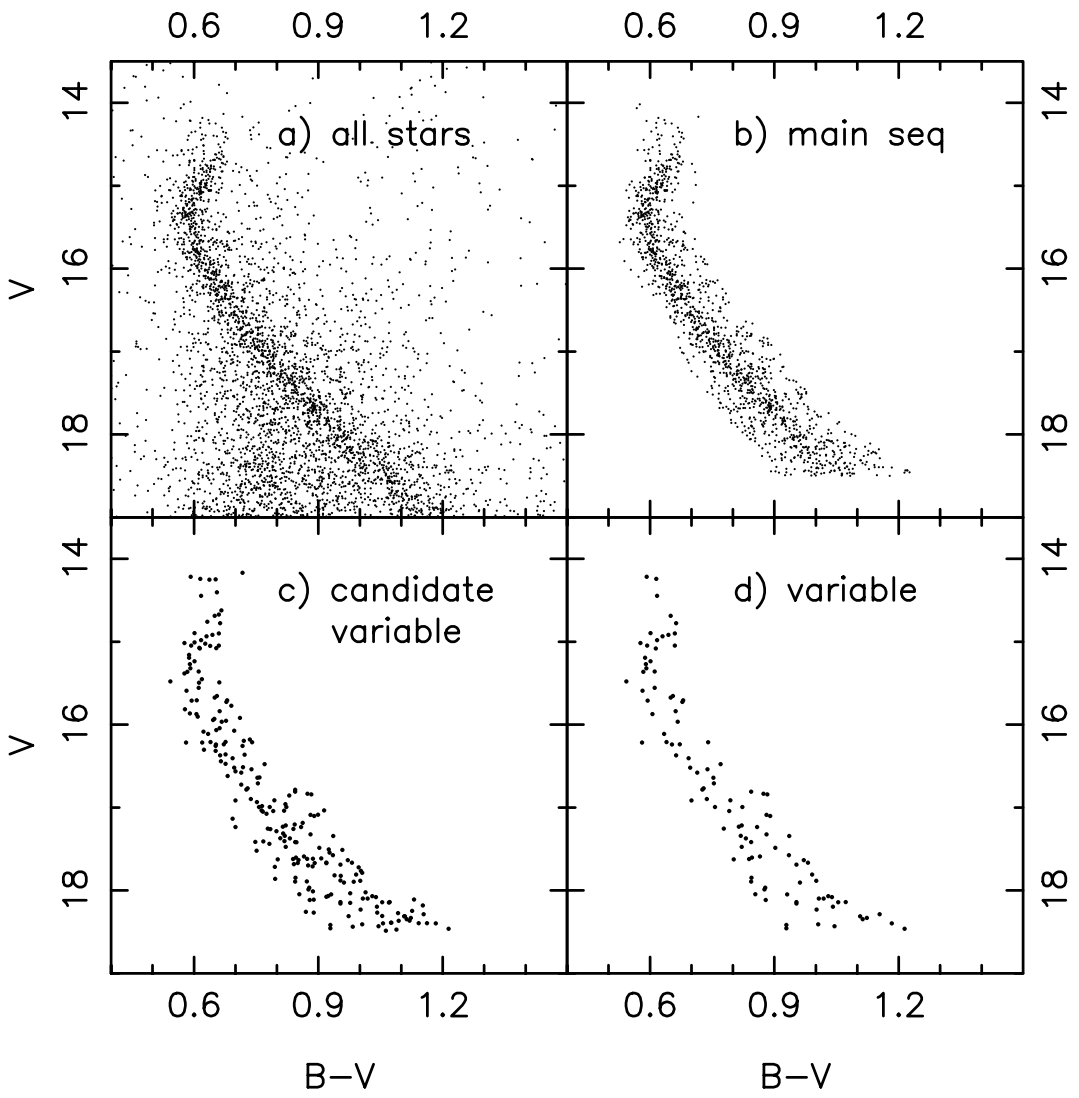


Figure 3.32: CMDs for NGC 6819. Panel a shows all stars observed. Panel b shows the stars photometrically chosen as the main sequence. Panel c shows the candidate variable stars. Panel d shows the variable stars, with $\alpha_v \geq 3$ and whose colors are correlated at a 99% significant level.

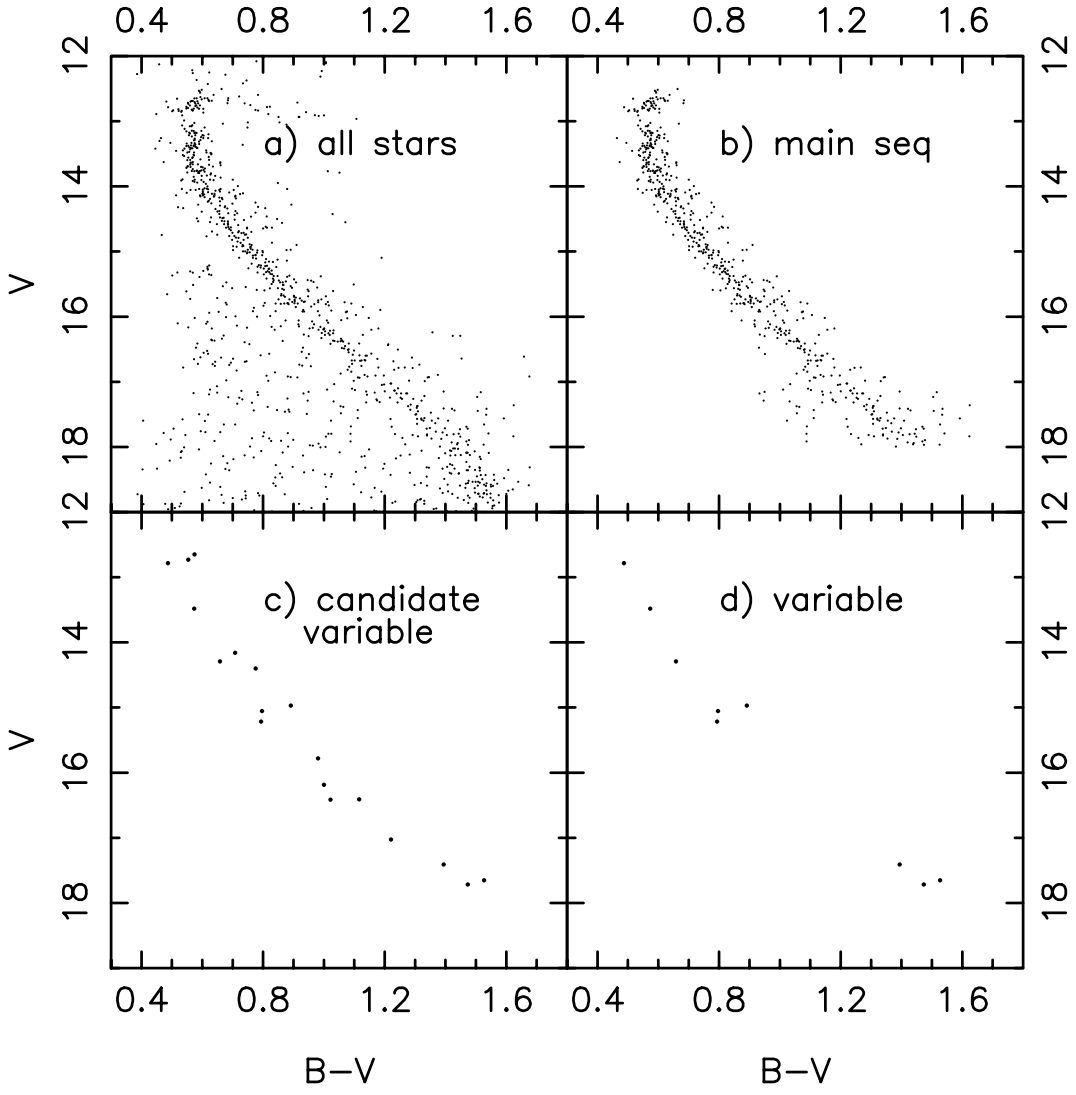


Figure 3.33: CMDs for M67. Panel a shows all stars observed. Panel b shows the stars photometrically chosen as the main sequence. Panel c shows the candidate variable stars. Panel d shows the variable stars, with $\alpha_v \geq 3$ and whose colors are correlated at a 99% significant level.

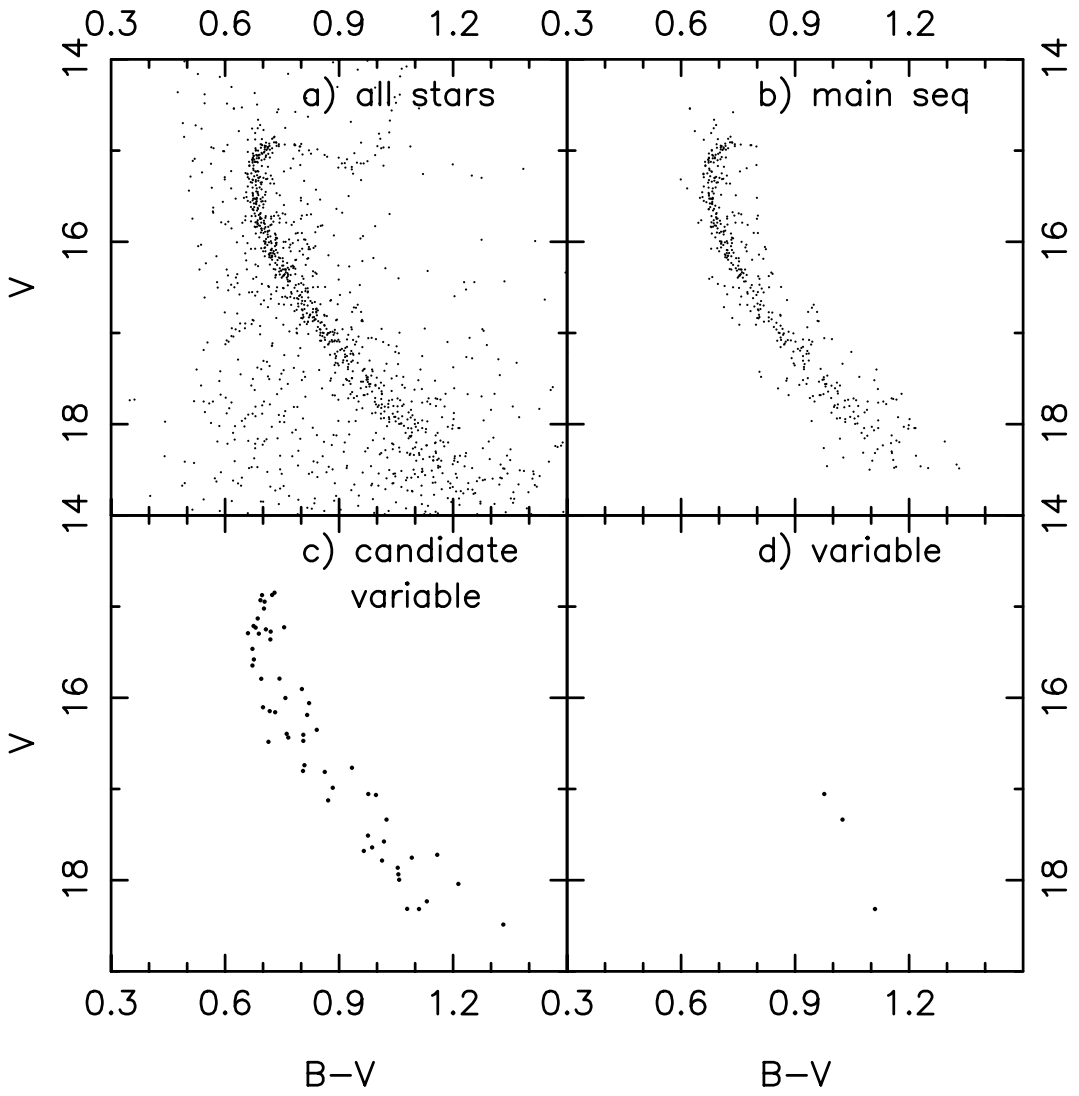


Figure 3.34: CMDs for NGC 188. Panel a shows all stars observed. Panel b shows the stars photometrically chosen as the main sequence. Panel c shows the candidate variable stars. Panel d shows the variable stars, with $\alpha_v \geq 3$ and whose colors are correlated at a 99% significant level.

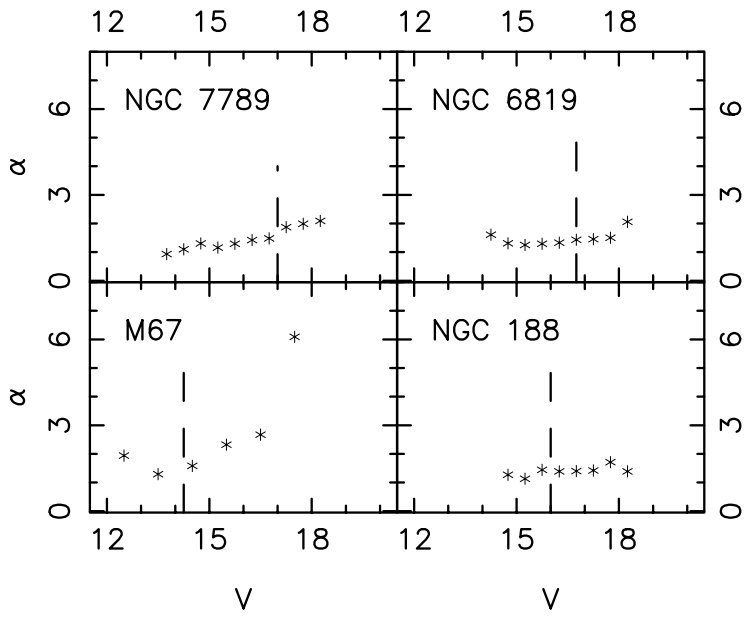


Figure 3.35: The significance index as a function of magnitude for the main sequence stars in the clusters indicated. The Sun's magnitude at the distance of each cluster is indicated by the dashed line.

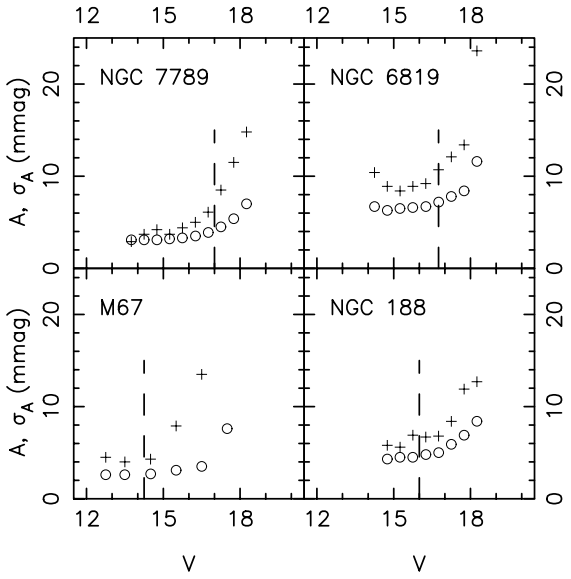


Figure 3.36: The activity index ($A_v$) (crosses), and the error in the activity index ($\sigma_{A_v}$, circles) as a function of magnitude for main sequence stars in the clusters indicated. The Sun's magnitude at the distance of each cluster is indicated by the dashed line.

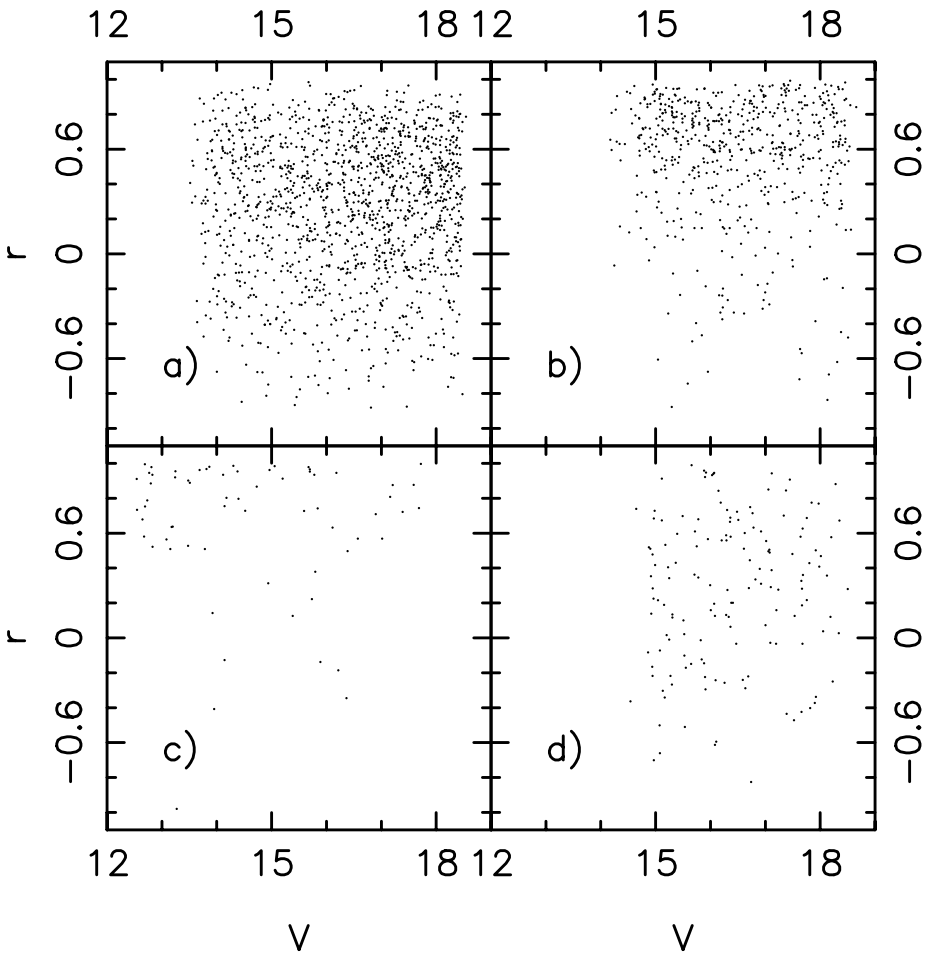


Figure 3.37: The correlation coefficient ($r$) as a function of magnitude for all main sequence stars. Panel a is NGC 7789, panel b is NGC 6819, panel c is M67, and panel d is NGC 188.

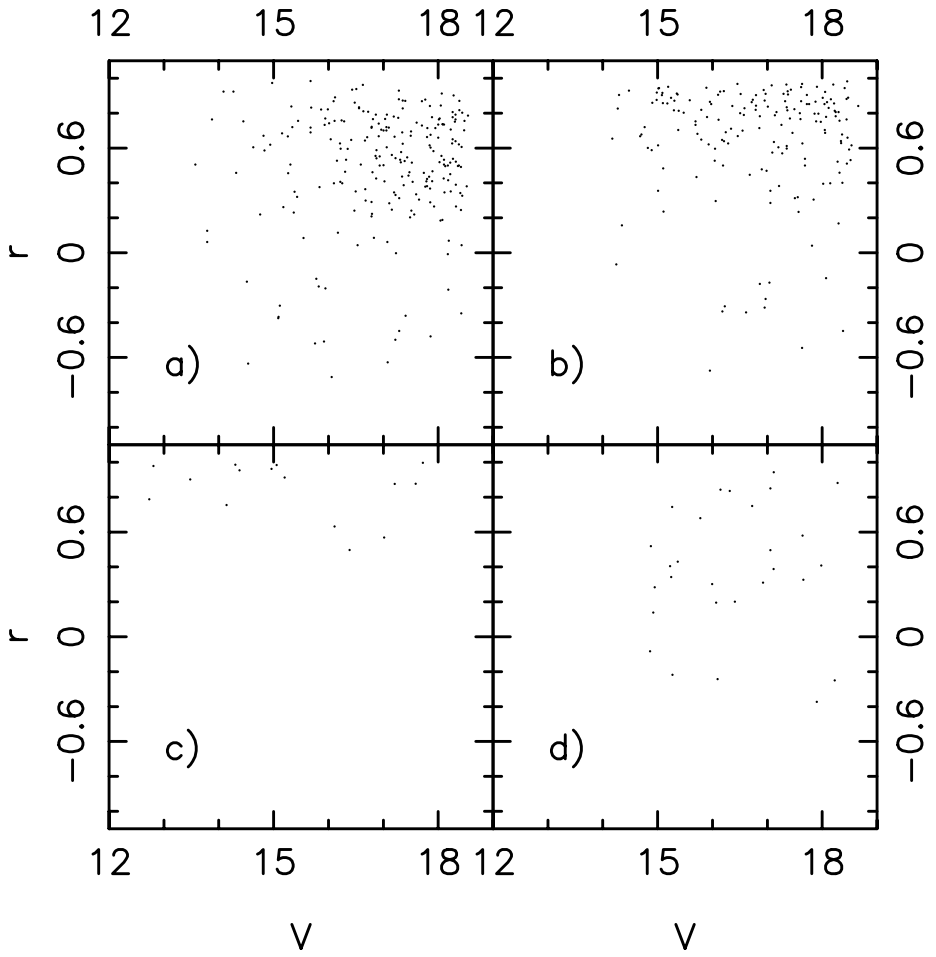


Figure 3.38: The correlation coefficient ($r$) as a function of magnitude for the candidate variable stars in each cluster. These stars were chosen only by their significance indices. Panel a is NGC 7789, panel b is NGC 6819, panel c is M67, and panel d is NGC 188.

| Cluster | $\sigma_{ens}$ | # MS | # Cand. Var. | # MS | # 99% sig. | # Active |
|---|---|---|---|---|---|---|
| NGC 7789 | 3 | 1596 | 248 (16%) | 1445 | 225 (16%) | 80 ± 9 (5%) |
| NGC 6819 | 6 | 1455 | 233 (16%) | 589 | 256 (43%) | 107 ± 10 (18%) |
| M67 | 2.5 | 74 | 18 (24%) | 65 | 29 (45%) | 9 ± 3 (14%) |
| NGC 188 | 4 | 451 | 57 (13%) | 150 | 19 (13%) | 4 ± 2 (3%) |

Table 3.13: Summary of Activity for Phase I. The second column lists the ensemble errors in millimagnitudes that were determined from the plots of $\sigma_{rms}$ and $\sigma_{mean}$. The third column lists the number of main sequence stars with at least five nights of observations in V that were included in the activity index calculation. The fourth column is the number of candidate variable stars found. The fifth column is the number of main sequence stars with at least five pairs of B and V and/or V and I observations on the same night; these stars were included in the correlation coefficient calculation. The sixth column is the number of stars whose correlation coefficients were 99% significant. The last column listing the fraction of active stars uses the lower of the two main sequence star numbers. The uncertainties in the number of active stars are based purely on Poisson statistics, since I have counted the number of active stars.

| Cluster | $\alpha_v$ Limit | # Non-Var. | # Var. |
|---|---|---|---|
| NGC 7789 | 1.0 | 327 | 248 |
| NGC 6819 | 1.0 | 370 | 232 |
| M67 | 1.5 | 24 | 18 |
| NGC 188 | 1.0 | 125 | 57 |

Table 3.14: Summary of the stars used in the power spectra calculations for Phase I, shown in Figure 3.40. The second column lists the upper limit for the significance index for the non-variable main sequence stars used in the power spectrum analysis. The third column lists the number of non-variable stars, and the fourth column lists the number of candidate variable stars used.

| Cluster | E(B-V) | V range | B-V range | Min. # V | # Stars |
|---|---|---|---|---|---|
| NGC 7789 | 0.28 | 17.0 - 17.5 | 0.8 - 1.1 | 50 | 14 |
| NGC 6819 | 0.14 | 16.75 - 17.25 | 0.65 - 0.95 | 65 | 22 |
| M67 | 0.05 | 14 - 15.25 | 0.55 - 0.85 | 30 | 10 |
| NGC 188 | 0.09 | 16.0 - 16.5 | 0.6 - 0.9 | 35 | 18 |

Table 3.15: Summary of solar analogs for Phase I. The range in V and B-V for each cluster was chosen to bracket the Sun's magnitude and color at the distance and reddening of each cluster. Column five lists the minimum number of nights in V required for each star to be included here. Information on the solar analogs in each cluster can be found in Tables 3.8, 3.16, 3.17, and 3.18, for the clusters NGC 7789, NGC 6819, M67, and NGC 188, respectively.

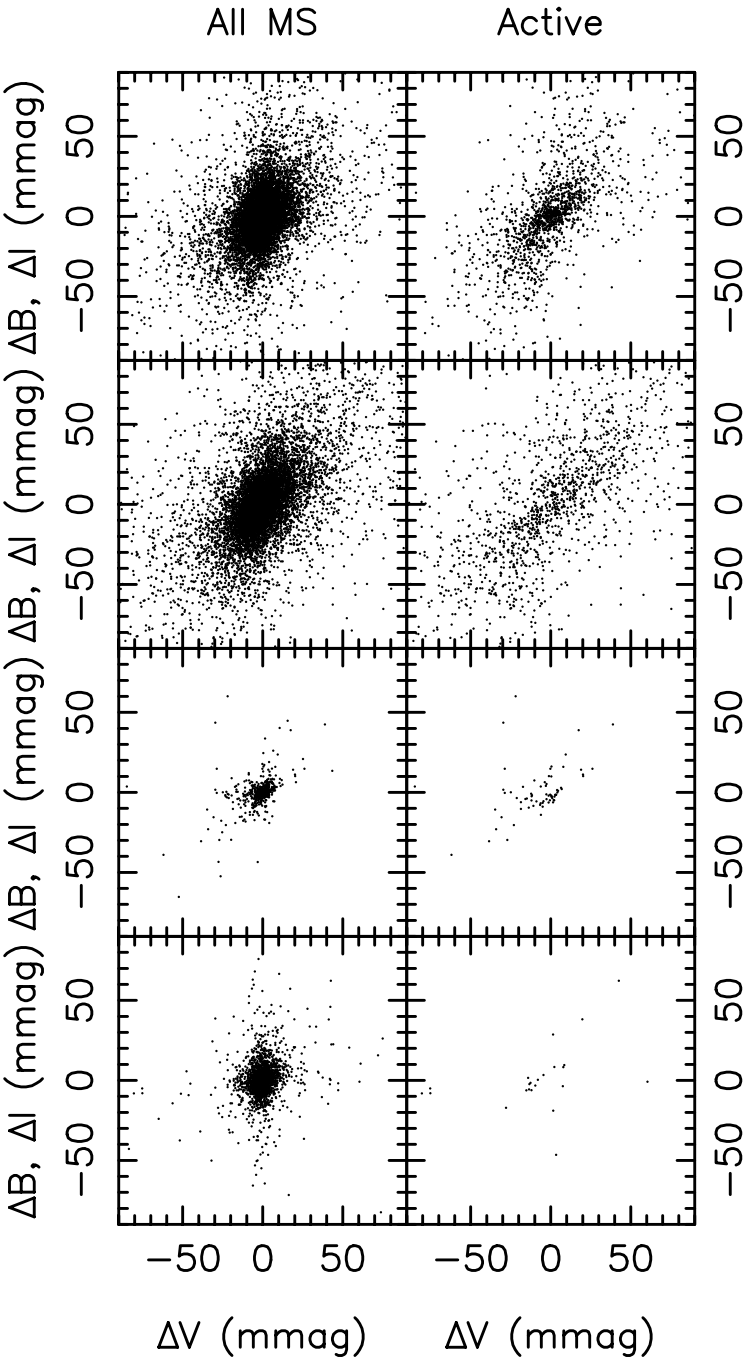


Figure 3.39: Mean V differential magnitudes versus mean B or I differential magnitudes for the main sequence stars in the left column of panels and for the variable stars in the right column of panels. From top to bottom, the rows are: NGC 7789, NGC 6819, M67, and NGC 188. Units are millimagnitudes.

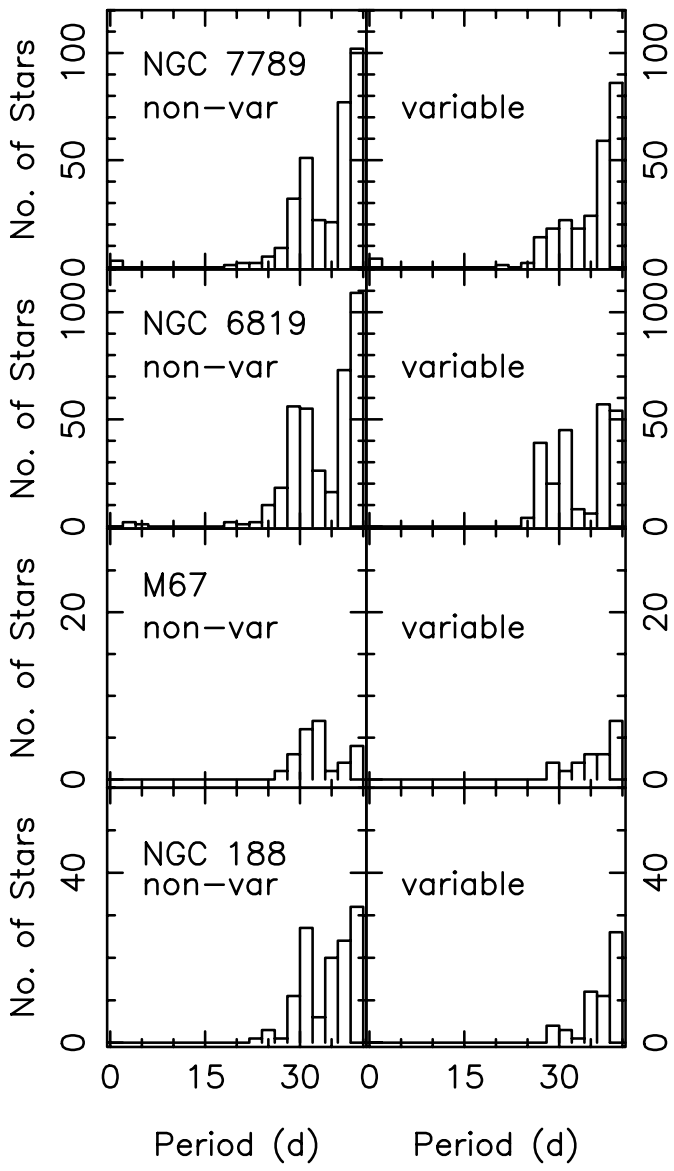


Figure 3.40: Histogram of periods of maximum power for non-variables in the left column and variable stars in the right column for the clusters indicated. Refer to Table 3.14 for a description of each plot. The distributions are nearly identical.

| Star | V | B-V | $\alpha_v$ | $r$ | 99%? | # V | $A_v$ | $A_b$ | $A_i$ |
|---|---|---|---|---|---|---|---|---|---|
| 3043 | 16.773 | 0.740 | 1.64 | 0.86 | Y | 65 | 13.2 | 13.7 | 25.2 |
| 3465 | 16.786 | 0.760 | 1.75 | -0.01 | N | 67 | 19.1 | 8.2 | 38.1 |
| 3128 | 16.866 | 0.790 | 1.80 | 0.72 | Y | 66 | 13.3 | 8.8 | 19.5 |
| 2959 | 16.868 | 0.865 | 1.87 | 0.45 | N | 65 | 14.5 | 9.8 | 27.4 |
| 3605 | 17.217 | 0.820 | 1.89 | 0.84 | Y | 66 | 29.3 | 27.1 | 92.3 |
| 3995 | 17.000 | 0.783 | 2.34 | 0.34 | N | 65 | 19.4 | 22.0 | 19.0 |
| 2939 | 16.764 | 0.741 | 2.37 | 0.72 | Y | 67 | 28.9 | 15.7 | 40.2 |
| 3842 | 16.937 | 0.790 | 2.51 | 0.81 | Y | 65 | 23.3 | 14.1 | 43.9 |
| 3753 | 17.204 | 0.863 | 2.73 | 0.86 | Y | 67 | 46.2 | 40.6 | 44.6 |
| 2945 | 16.870 | 0.772 | 2.75 | 0.59 | Y | 67 | 39.7 | 25.8 | 56.7 |
| 3691 | 16.962 | 0.792 | 2.90 | 0.87 | Y | 67 | 23.3 | 16.0 | 76.8 |
| 3994 | 16.851 | 0.753 | 2.92 | 0.15 | N | 65 | 29.1 | 11.7 | 17.2 |
| 2818 | 17.120 | 0.829 | 2.99 | 0.80 | Y | 67 | 28.1 | 30.0 | 23.3 |
| 3349* | 16.768 | 0.729 | 3.12 | 0.84 | Y | 68 | 27.6 | 8.9 | 28.0 |
| 3885 | 17.204 | 0.843 | 3.15 | 0.38 | N | 66 | 36.2 | 24.3 | 13.4 |
| 3336* | 17.102 | 0.890 | 3.16 | 0.64 | Y | 66 | 32.7 | 34.0 | 42.2 |
| 3214* | 16.842 | 0.883 | 3.31 | 0.72 | Y | 65 | 30.5 | 24.8 | 45.0 |
| 3539* | 16.897 | 0.737 | 3.31 | 0.78 | Y | 65 | 31.4 | 24.2 | 74.5 |
| 3500* | 16.913 | 0.794 | 3.60 | 0.87 | Y | 68 | 46.4 | 19.2 | 134.9 |
| 2906* | 16.994 | 0.823 | 4.83 | 0.84 | Y | 68 | 56.3 | 21.5 | 183.1 |
| 3380* | 17.089 | 0.881 | 5.10 | 0.79 | Y | 67 | 68.6 | 65.9 | 65.7 |
| 3140* | 17.041 | 0.791 | 5.11 | 0.96 | Y | 68 | 68.4 | 50.1 | 54.7 |

Table 3.16: Solar analogs in NGC 6819. An asterisk on the star number designates an active star. $\alpha_v$ is the significance index, and $r$ is the correlation coefficient. "99%?" indicates whether the correlation coefficient is significant at the 99% level. Columns 7 indicates the number of nights on which the star was observed through the V filter. (All stars were observed eleven nights through the B filter, except 2959 and 3605, which had 10 B observations. All stars had eighteen observations through the I filter, except for the following stars, which had seventeen: 3043, 3465, 3691, 3885, 3380.) The last three columns are the activity indices of the nightly mean differential magnitudes through each filter in mmags.

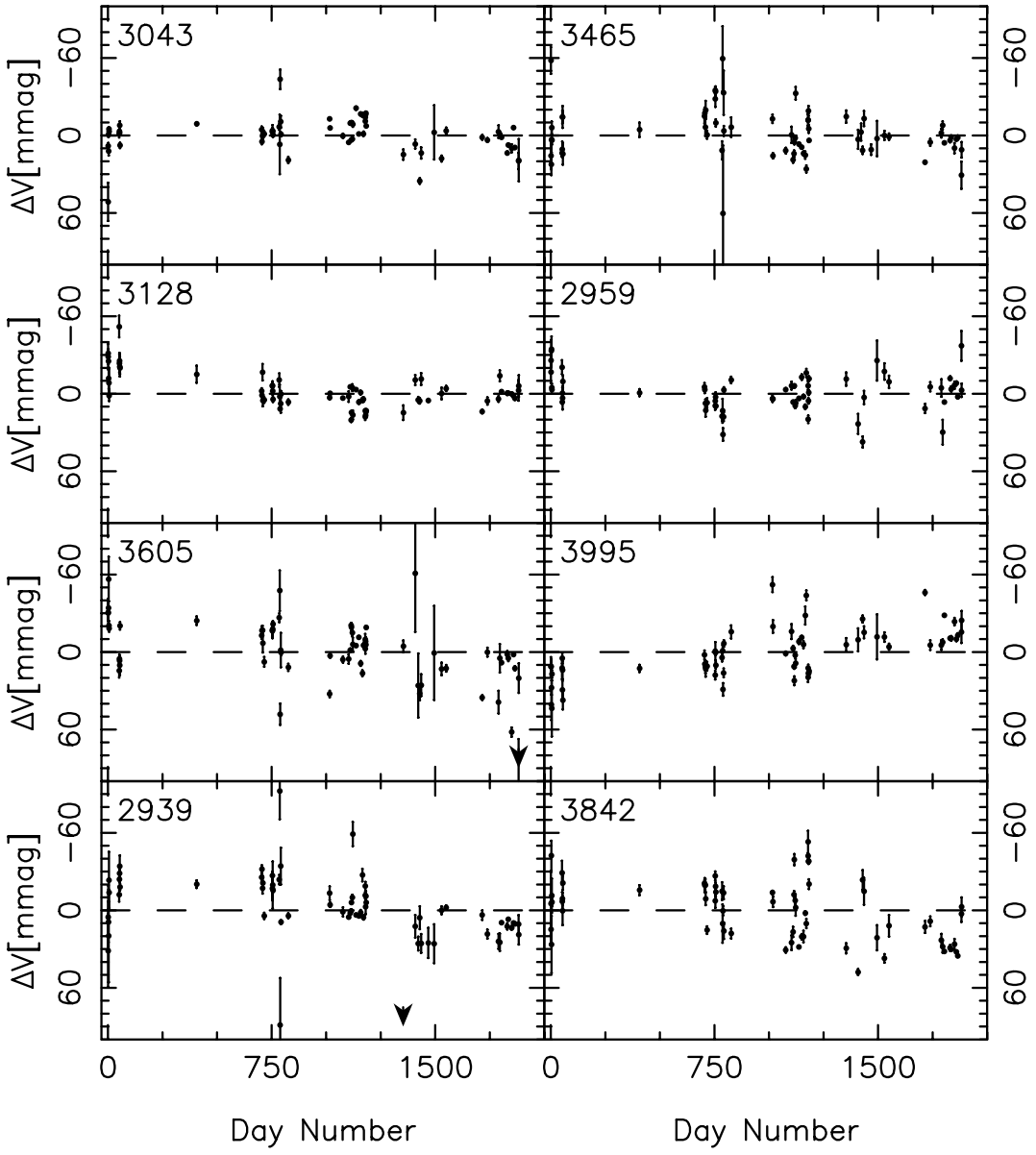


Figure 3.41: Nightly mean V data for solar analogs in NGC 6819. Stars are ordered by increasing significance index. An arrow indicates where a point falls of the plot. More solar analogs can be seen in Figures 3.42 and 3.43. Information about the stars can be found in Table 3.16.

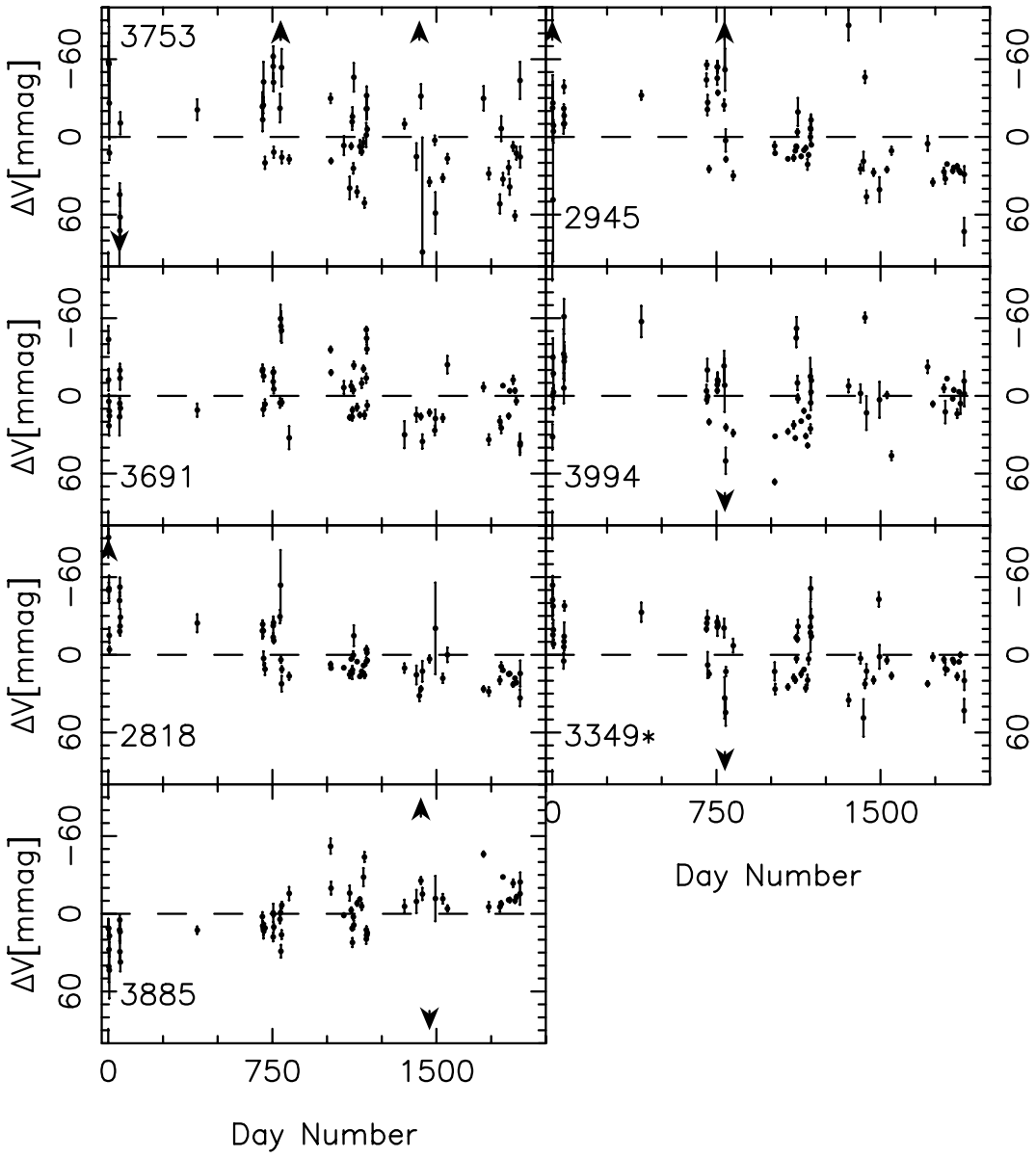


Figure 3.42: Nightly mean V data for solar analogs in NGC 6819, continued from Figure 3.41. Stars are ordered by increasing significance index. An arrow indicates where a point falls of the plot. An asterisk designates an active star. More solar analogs can be seen in Figure 3.43. Information about the stars can be found in Table 3.16.

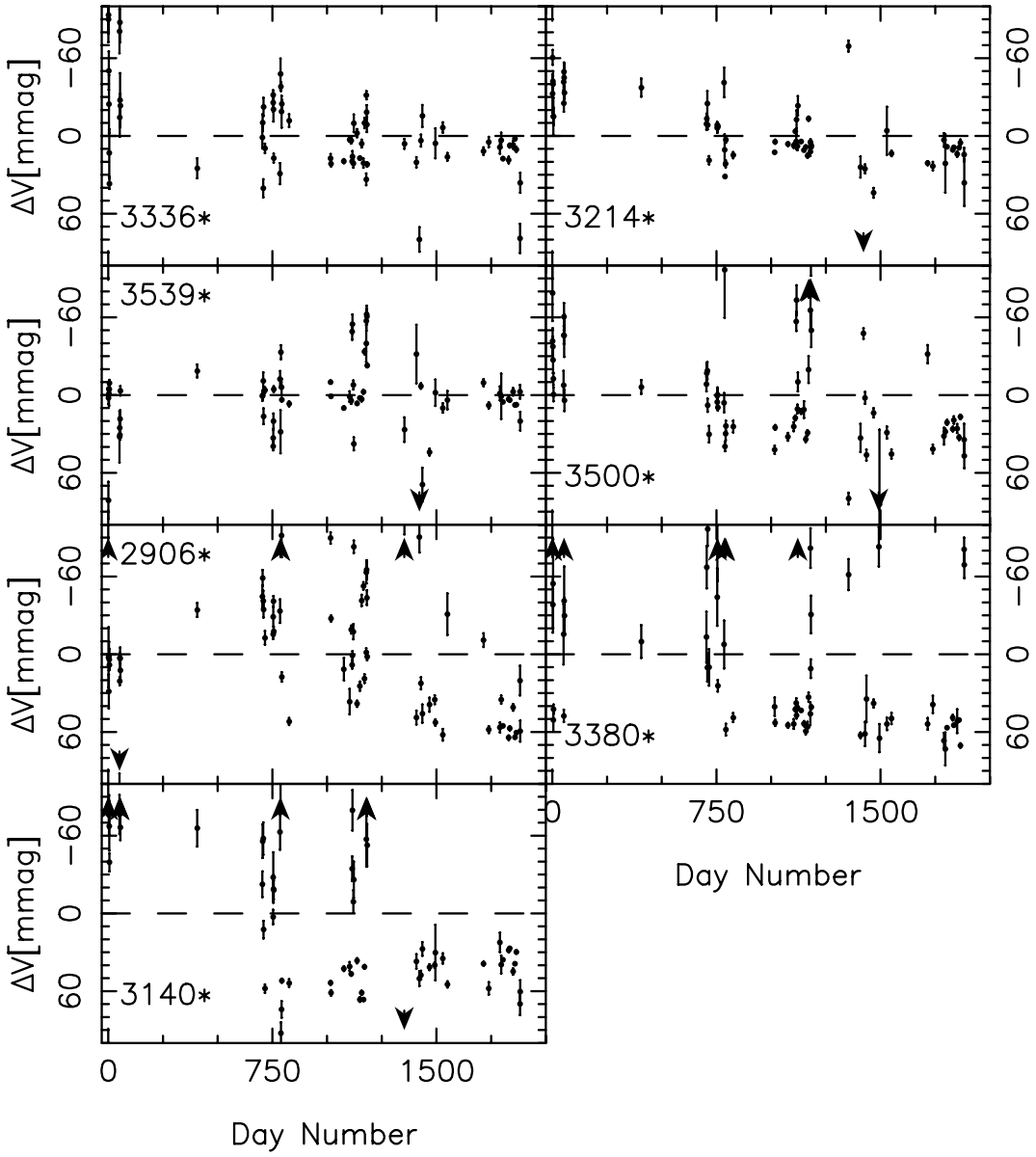


Figure 3.43: Nightly mean V data for solar analogs in NGC 6819, continued from Figure 3.42. Stars are ordered by increasing significance index. An arrow indicates where a point falls of the plot. An asterisk designates an active star. Information about the stars can be found in Table 3.16.

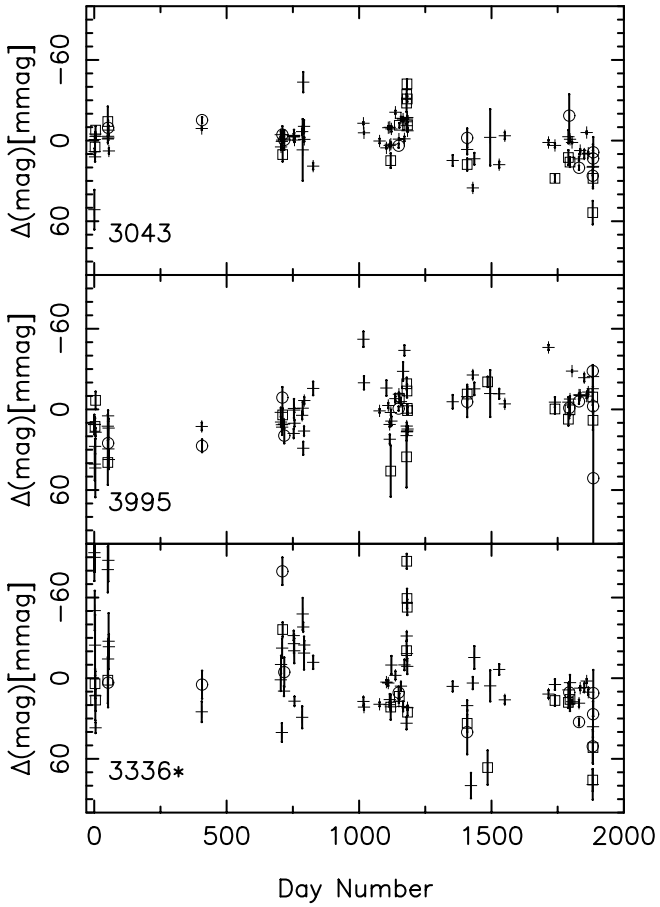


Figure 3.44: Nightly mean BVI data for selected stars in NGC 6819. The crosses are V data, the circles are B data, and the boxes are I data. Y-axis units are in millimagnitudes. Error bars are included on all points. An arrow indicates where a point falls of the plot. Information about the stars can be found in Table 3.16.

| Star | V | B-V | $\alpha$ | r | 99% sig? | # V | # B | #I | $A_v$ | $A_i$ |
|---|---|---|---|---|---|---|---|---|---|---|
| 5567 | 14.164 | 0.608 | 1.00 | -0.126 | N | 31 | 1 | 9 | 2.5 | 1.4 |
| 5777 | 14.516 | 0.737 | 1.08 | 0.728 | N | 34 | 2 | 10 | 2.8 | 2.7 |
| 5807 | 14.718 | 0.729 | 1.32 | 0.867 | Y | 31 | 1 | 10 | 3.5 | 3.7 |
| 5776 | 14.122 | 0.606 | 1.54 | 0.935 | Y | 32 | 2 | 10 | 4.0 | 6.5 |
| 5788 | 14.183 | 0.711 | 1.57 | 0.803 | Y | 34 | 2 | 11 | 4.2 | 4.4 |
| 5768 | 14.928 | 0.759 | 1.74 | 0.313 | N | 34 | 2 | 10 | 4.8 | 2.0 |
| 5709* | 15.214 | 0.793 | 3.09 | 0.913 | Y | 30 | 1 | 9 | 8.1 | 3.0 |
| 5594 | 14.160 | 0.708 | 3.12 | 0.755 | N | 31 | 2 | 9 | 8.1 | 6.8 |
| 5770* | 15.055 | 0.797 | 4.61 | 0.983 | Y | 31 | 1 | 10 | 14.3 | 13.3 |
| 5748* | 14.335 | 0.807 | 11.37 | 0.935 | Y | 35 | 1 | 12 | 43.6 | 22.8 |

Table 3.17: Solar analogs in M67. Solar analogs are plotted in Figure 3.45. An asterisk by the star number designates an active star. "99%?" indicates whether the correlation coefficient is significant at the 99% level. Columns 7 - 9 indicate the number of nights on which the star was observed through each filter. The last three columns are the activity indices of the nightly mean differential magnitudes through each filter in mmags. We did not have the required five observations through the B filter in order to calculate $A_b$.

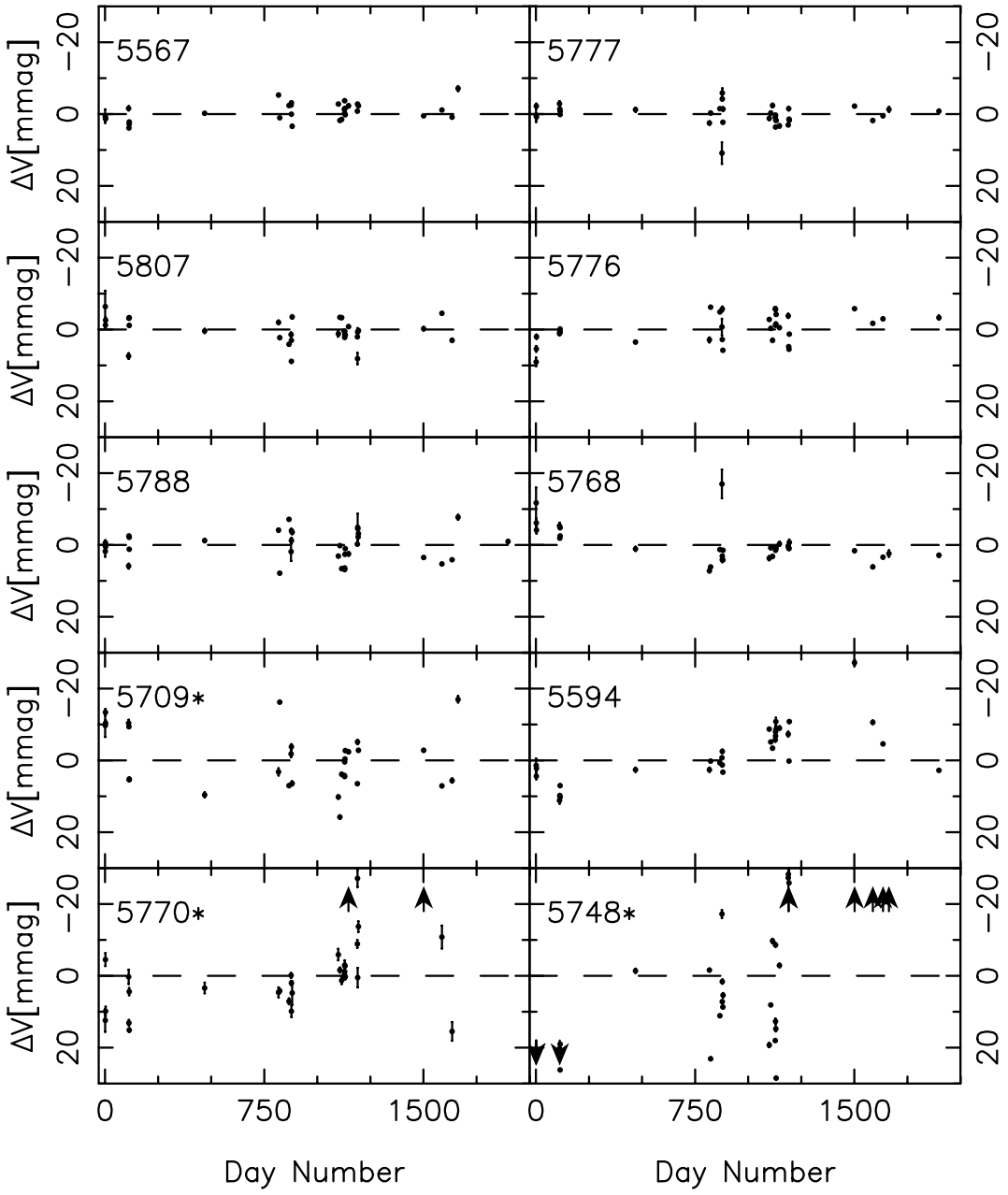


Figure 3.45: Solar analogs in M67. Stars are ordered by increasing significance index. Star properties are listed in Table 3.17. Units on y-axis are millimagnitudes. Error bars are included on all points. An arrow indicates where a point falls off the plot. An asterisk designates an active star. Note the scale on the x-axis is considerably smaller than the previous plots.

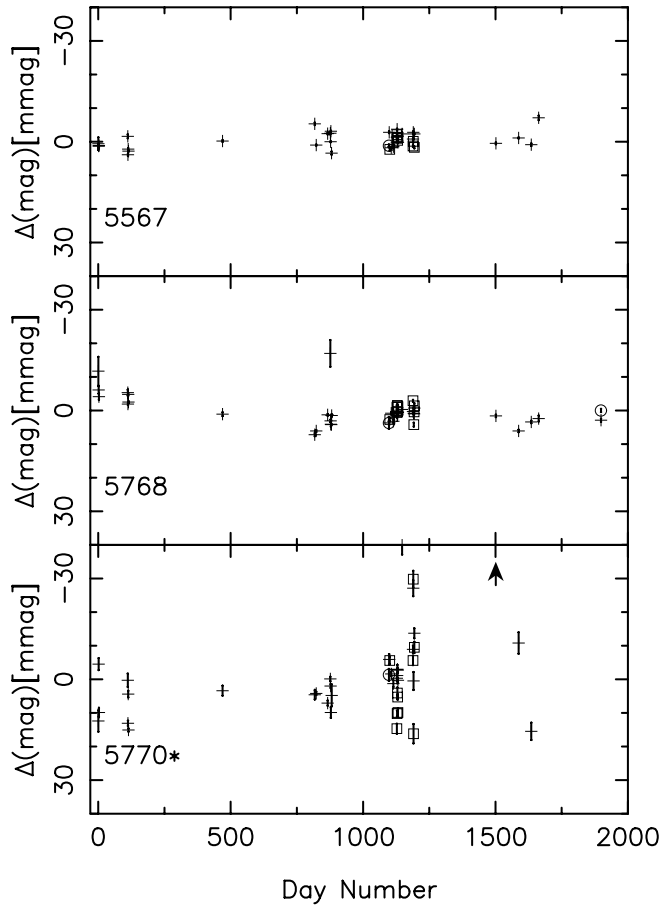


Figure 3.46: Nightly mean BVI data for selected stars in M67. The crosses are V data, the circles are B data, and the boxes are I data. Y-axis units are in millimagnitudes. Error bars are included on all points. An arrow indicates where a point falls of the plot. An asterisk designates an active star. Information about the stars can be found in Table 3.17.

| Star | V | B-V | $\alpha_v$ | r | 99%? | # V | # B | $A_v$ | $A_b$ | $A_i$ |
|---|---|---|---|---|---|---|---|---|---|---|
| 549 | 16.354 | 0.757 | 1.05 | 0.664 | N | 41 | 6 | 5.1 | 10.0 | 2.3 |
| 669 | 16.010 | 0.706 | 1.16 | 0.158 | N | 41 | 6 | 6.3 | 8.0 | 6.8 |
| 447 | 16.462 | 0.697 | 1.17 | -0.034 | N | 35 | 5 | 5.3 | 5.2 | 7.6 |
| 655 | 16.394 | 0.749 | 1.18 | 0.201 | N | 38 | 6 | 5.3 | 6.6 | 14.7 |
| 513 | 16.366 | 0.754 | 1.39 | 0.064 | N | 41 | 6 | 6.4 | 9.8 | 7.9 |
| 452 | 16.362 | 0.734 | 1.43 | 0.723 | N | 35 | 5 | 6.9 | 7.8 | 6.7 |
| 611 | 16.093 | 0.722 | 1.47 | 0.126 | N | 40 | 6 | 6.7 | 6.5 | 4.4 |
| 632 | 16.307 | 0.759 | 1.51 | 0.274 | N | 35 | 6 | 7.4 | 3.0 | 3.6 |
| 577 | 16.090 | 0.720 | 1.53 | -0.594 | N | 42 | 7 | 7.2 | 13.3 | 2.1 |
| 478 | 16.254 | 0.737 | 1.87 | -0.257 | N | 41 | 6 | 8.6 | 8.6 | 5.0 |
| 679 | 16.196 | 0.787 | 1.87 | 0.559 | N | 45 | 7 | 13.2 | 6.3 | 4.0 |
| 668 | 16.291 | 0.744 | 2.05 | 0.132 | N | 36 | 6 | 9.5 | 4.7 | 6.1 |
| 574 | 16.377 | 0.803 | 2.34 | 0.689 | N | 43 | 7 | 10.6 | 8.2 | 3.0 |
| 645 | 16.335 | 0.760 | 2.70 | 0.121 | N | 45 | 7 | 12.8 | 9.0 | 22.8 |
| 472 | 16.304 | 0.768 | 2.77 | 0.733 | N | 40 | 6 | 13.2 | 9.6 | 23.1 |
| 648 | 16.436 | 0.766 | 3.04 | 0.201 | N | 43 | 6 | 16.5 | 8.3 | 4.3 |
| 709 | 16.059 | 0.821 | 3.08 | 0.196 | N | 43 | 7 | 22.6 | 8.6 | 9.3 |
| 742 | 16.188 | 0.816 | 8.52 | ... | ... | 43 | 7 | 67.1 | 20.9 | ... |

Table 3.18: Solar analogs in NGC 188. Solar analogs are plotted in Figures 3.47 and 3.48. An asterisk by the star number designates an active star. "99%?" indicates whether the correlation coefficient is significant at the 99% level. Columns 7 and 8 indicate the number of nights on which the star was observed through the V and B filters, respectively. (All stars were observed twelve nights through the I filter, except 447 and 452, which were observed eight nights, star 679, which was observed eleven nights, and star 742, which had no I observations.) The last three columns are the activity indices of the nightly mean differential magnitudes through each filter in mmags. Star 742 did not have enough simultaneous observations to qualify for our correlation coefficient calculation.

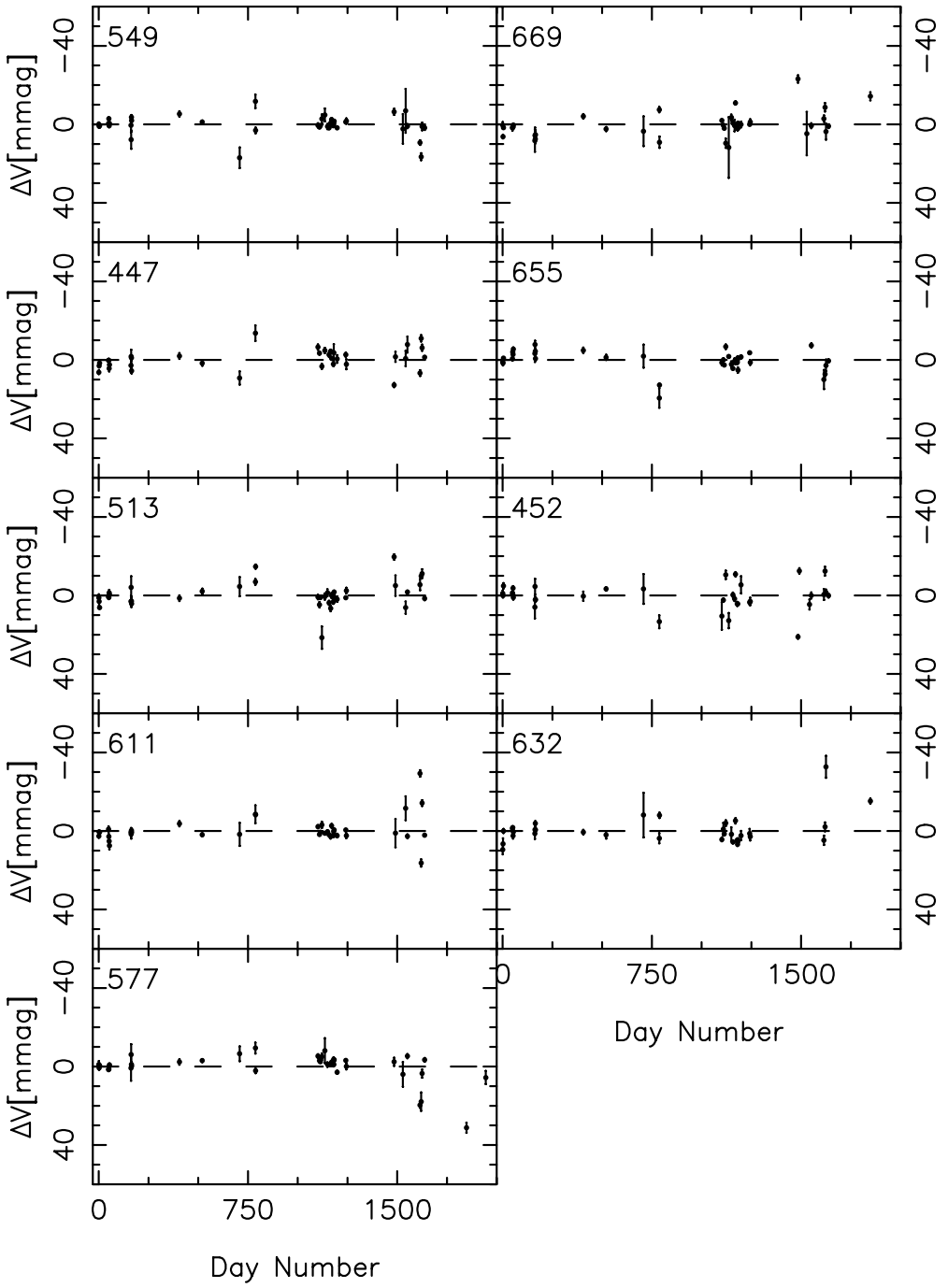


Figure 3.47: Solar analogs with $16.0 < V < 16.5$ in NGC 188 for individual stars. Stars are ordered by increasing significance index. Star properties are listed in Table 3.18. Units on y-axis are millimagnitudes. Error bars are included on all points. An arrow indicates where a point falls off the plot. More solar analogs are shown in Figure 3.48.

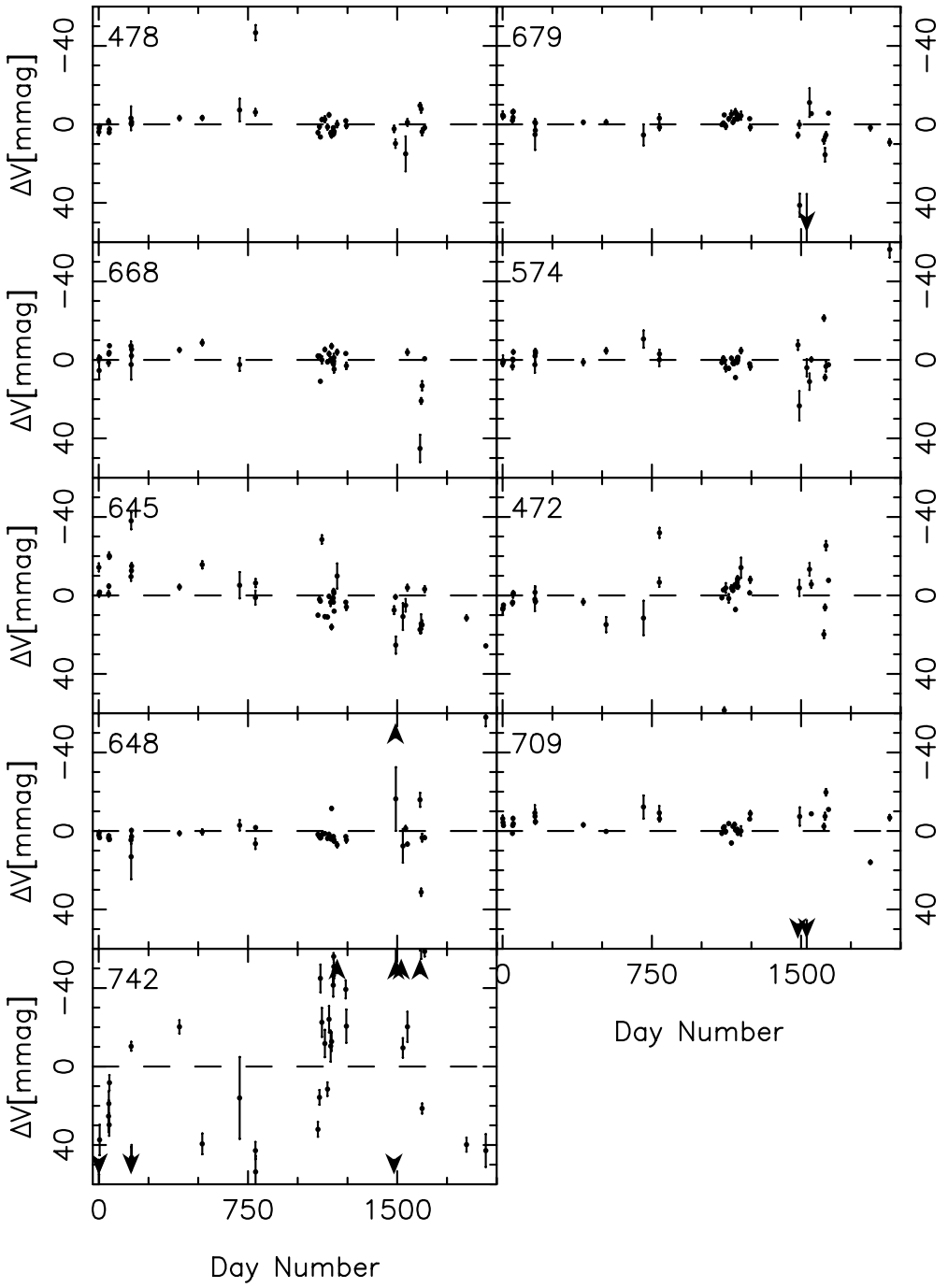


Figure 3.48: Solar analogs with $16.0 < V < 16.5$ in NGC 188 for individual stars, continued from Figure 3.47. Stars are ordered by increasing significance index. Star properties are listed in Table 3.18. Units on y-axis are millimagnitudes. Error bars are included on all points. An arrow indicates where a point falls off the plot.

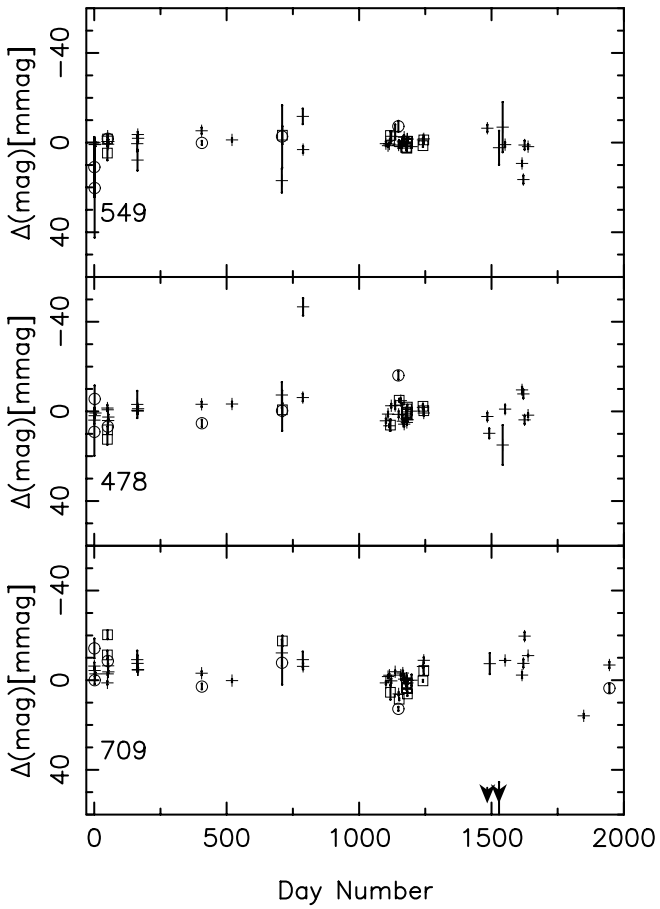


Figure 3.49: Nightly mean BVI data for selected stars in NGC 188. The crosses are V data, the circles are B data, and the boxes are I data. Y-axis units are in millimagnitudes. Error bars are included on all points. An arrow indicates where a point falls of the plot. Information about the stars can be found in Table 3.18.

| Cluster | # MS | # Cand. Var. | # MS | # 99% sig. | # Active |
|---|---|---|---|---|---|
| NGC 7789 | 1558 | 822 (53%) | 1151 | 47 (4%) | 33 ± 6 (3%) |
| NGC 6819 | 1414 | 682 (48%) | 1401 | 96 (7%) | 79 ± 9 (6%) |
| M67 | 74 | 63 (85%) | ... | ... | ... |
| NGC 188 | 444 | 151 (34%) | 379 | 1 (0%) | 0 |

Table 3.19: Summary of Annual Activity for Phase I. The second column lists the number of main sequence stars with at least three seasons of observations in V that were included in the activity index calculation. The third column is the number of candidate variable stars found. The fourth column is the number of main sequence stars with at least five pairs of B and V and/or V and I observations on the same season; these stars were included in the correlation coefficient calculation. The fifth column is the number of stars whose correlation coefficients were 99% significant. The last column listing the fraction of active stars uses the lower of the two main sequence star numbers; as for the nightly data, the uncertainty in the number of active stars is simply the square root. M67 did not have enough seasons of B and I measurements to fulfill the correlation coefficient requirement.

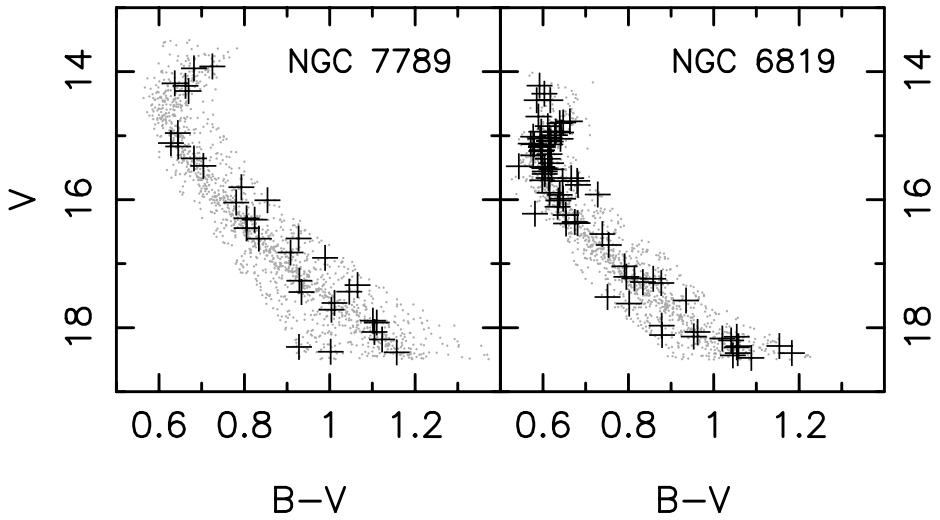


Figure 3.50: Color-magnitude diagram for annual means of stars in NGC 7789 and NGC 6819. The gray dots are all of the main sequence stars with at least three years' observations through the V filter. The crosses are the stars found to be active.

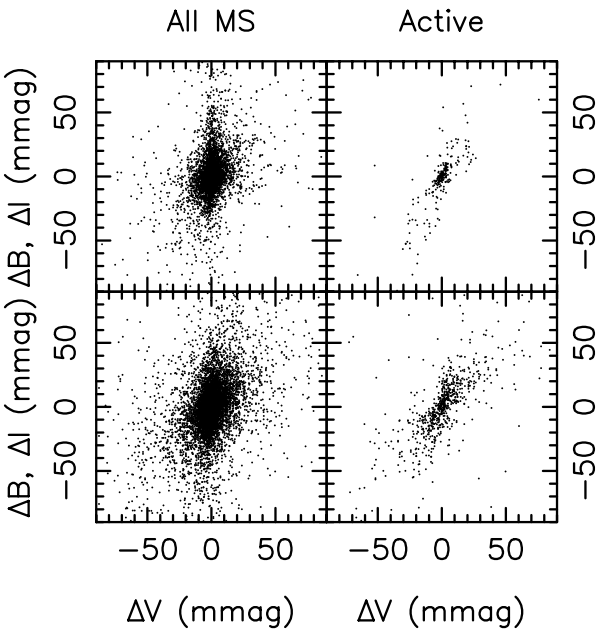


Figure 3.51: Annual mean V differential magnitudes versus mean B or I differential magnitudes for NGC 7789 and NGC 6819. The top row shows the main sequence and variable stars in NGC 7789, and the second row shows the main sequence and variable stars in NGC 6819.

| Star | V | B-V | $\alpha_v$ | $r$ | $A_v$ | $A_b$ | $A_i$ |
|---|---|---|---|---|---|---|---|
| 2848 | 15.136 | 0.617 | 9.79 | 0.79 | 16.0 | 14.2 | 17.5 |
| 3721 | 15.706 | 0.680 | 9.86 | 0.83 | 20.1 | 27.3 | 29.0 |
| 3085 | 14.445 | 0.585 | 10.01 | 0.82 | 14.8 | 27.6 | 16.5 |
| 3912 | 14.445 | 0.617 | 10.17 | 0.79 | 31.5 | 33.5 | 44.9 |
| 3474 | 16.112 | 0.634 | 10.78 | 0.83 | 21.2 | 25.9 | 22.6 |
| 3840 | 14.804 | 0.639 | 10.89 | 0.88 | 15.5 | 22.2 | 17.1 |
| 3576 | 18.198 | 1.041 | 11.21 | 0.74 | 102.1 | 110.5 | 210.4 |
| 3304 | 15.016 | 0.577 | 11.64 | 0.90 | 41.7 | 35.3 | 46.9 |
| 4248 | 18.472 | 1.088 | 11.67 | 0.81 | 100.8 | 124.7 | 28.9 |
| 3764 | 15.046 | 0.593 | 12.46 | 0.84 | 21.7 | 24.7 | 28.9 |
| 3270 | 17.967 | 0.878 | 13.15 | 0.82 | 189.6 | 168.3 | 98.5 |
| 3183 | 16.218 | 0.581 | 13.43 | 0.82 | 38.4 | 29.7 | 56.8 |
| 3212 | 18.432 | 1.045 | 14.02 | 0.78 | 279.8 | 310.1 | 161.7 |
| 4236 | 17.231 | 0.814 | 14.07 | 0.83 | 106.9 | 81.7 | 53.0 |

Table 3.20: Fifteen variables in NGC 6819 with the largest significance indices found by analyzing their annual mean differential data, which are plotted in Figure 3.53. $\alpha_v$ is the significance index based on the annual mean differential magnitudes, and $r$ is the correlation coefficient. The last three columns are the activity indices through each filter. Each star has six seasons of observations in V and B. All stars have five seasons of observations in I, except 4248, which has four.

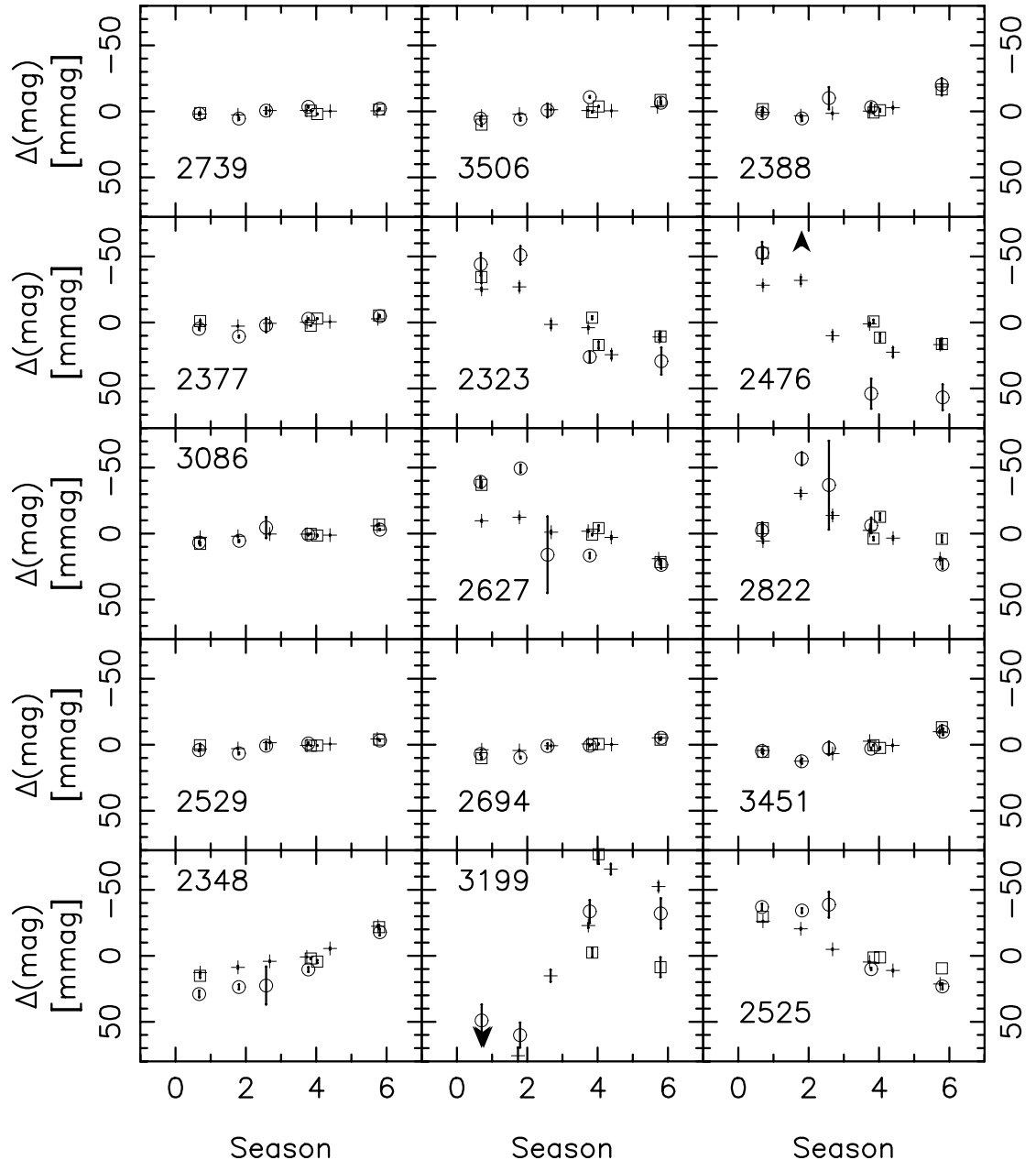


Figure 3.52: Annual mean V, B, and I differential magnitudes versus season for fifteen of the stars in NGC 7789 with six seasons of V observations and the highest significance index. Stars are ordered by increasing significance index. Crosses represent V, circles are B, and squares are I. Error bars are also plotted. Season 0 is 1996, and thus season 6 is 2001. Information about the stars can be found in Table 3.9.

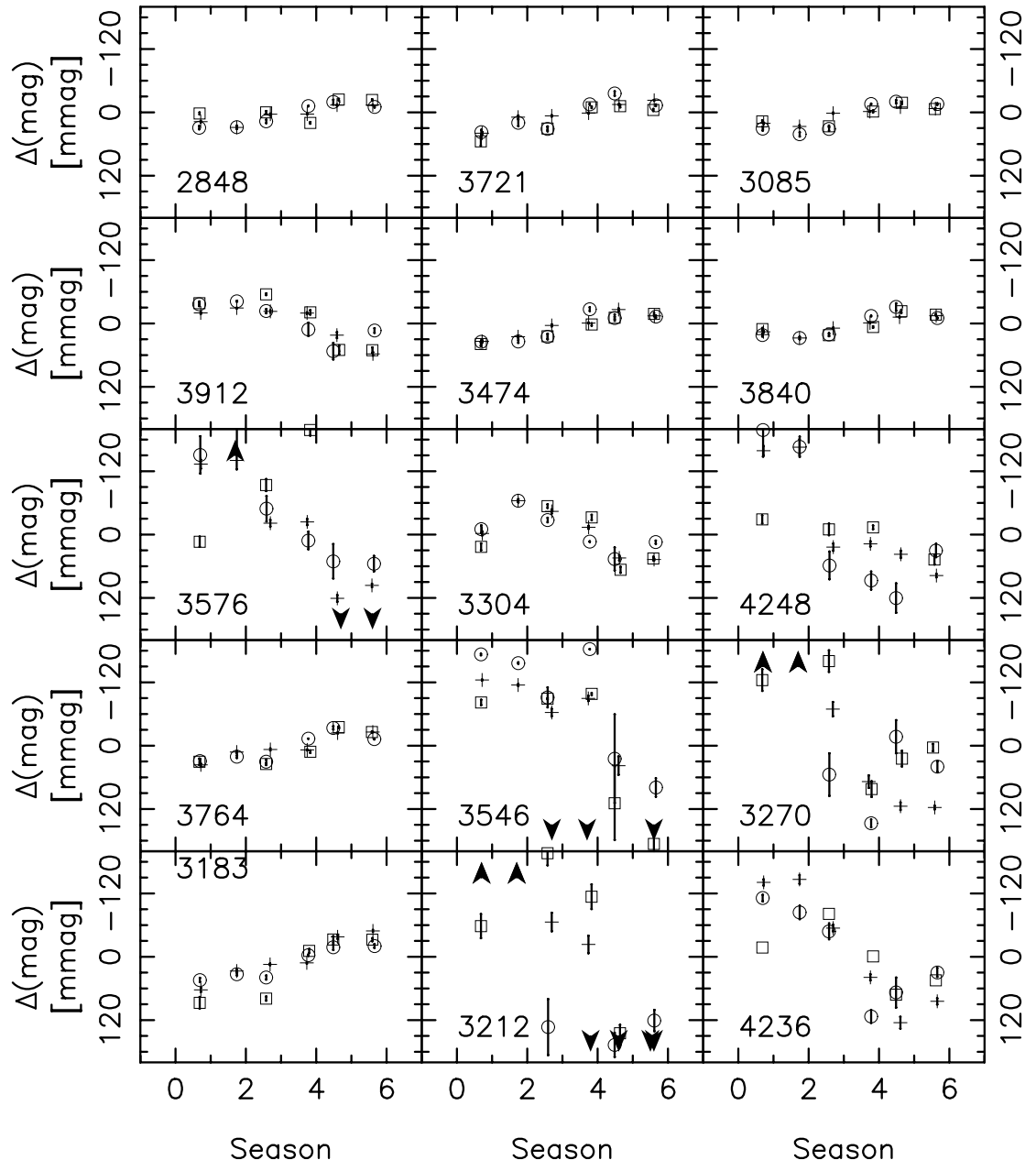


Figure 3.53: Annual mean V, B, and I differential magnitudes versus season for the fifteen variable stars in NGC 6819 with the largest significance index found by analyzing the annual mean differential magnitude data. Stars are ordered by increasing significance index. Crosses represent V, circles are B, and squares are I. Error bars are also plotted. Season 0 is 1996, and thus season 6 is 2001. The stars are ordered in increasing significance index. Parameters about the stars can be found in Table 3.20.

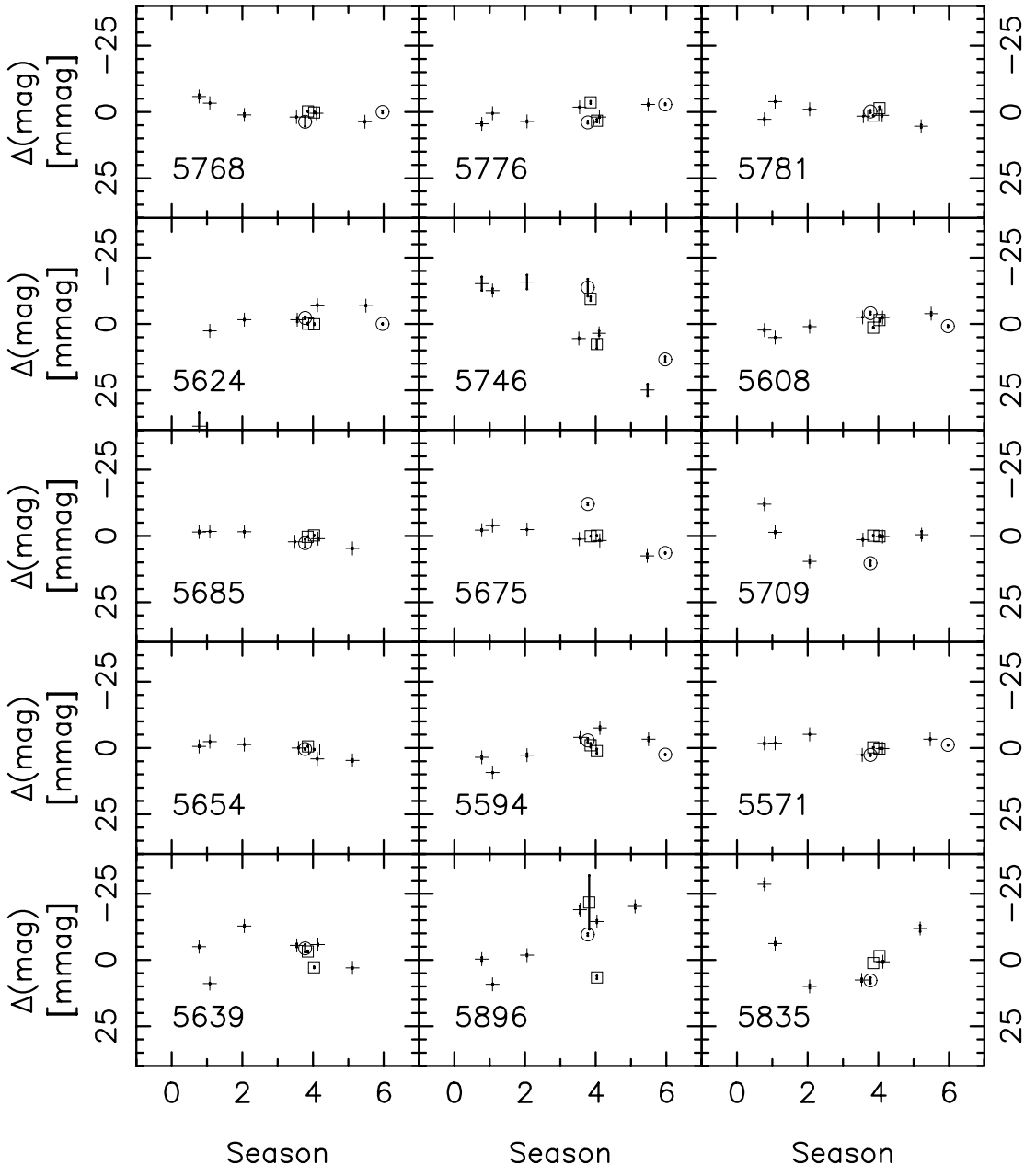


Figure 3.54: Annual mean V, B, and I differential magnitudes versus season for the fifteen candidate variable stars in M67 with the largest significance indices found by analyzing the annual mean differential magnitude data and at least six seasons of observations in V. Stars are ordered by increasing significance index. Crosses represent V, circles are B, and squares are I. Error bars are also plotted. Season 0 is 1996, and thus season 6 is 2001. The stars are ordered in increasing significance index. Information about the stars can be found in Table 3.21.

| Star | V | B-V | $\alpha_v$ | # B | $A_v$ |
|---|---|---|---|---|---|
| 5768 | 14.928 | 0.759 | 7.23 | 2 | 3.2 |
| 5776 | 14.122 | 0.606 | 7.53 | 2 | 2.8 |
| 5781 | 13.242 | 0.596 | 7.66 | 1 | 3.1 |
| 5624 | 12.730 | 0.554 | 7.68 | 2 | 16.3 |
| 5746 | 16.417 | 1.022 | 7.97 | 2 | 14.7 |
| 5608 | 13.928 | 0.574 | 8.09 | 2 | 3.1 |
| 5685 | 13.933 | 0.605 | 8.28 | 1 | 2.4 |
| 5675 | 12.755 | 0.559 | 8.99 | 2 | 3.8 |
| 5709 | 15.214 | 0.793 | 9.03 | 1 | 6.3 |
| 5654 | 12.540 | 0.591 | 9.22 | 1 | 2.8 |
| 5594 | 14.160 | 0.708 | 10.55 | 2 | 5.6 |
| 5571 | 12.651 | 0.517 | 11.93 | 2 | 2.9 |
| 5639 | 14.929 | 0.658 | 16.93 | 1 | 7.5 |
| 5896 | 12.650 | 0.574 | 16.98 | 1 | 13.3 |
| 5835 | 14.972 | 0.891 | 17.42 | 1 | 13.9 |

Table 3.21: Fifteen candidate variables in M67 with the largest significance indices found by analyzing their annual mean differential data, which are plotted in Figure 3.54. $\alpha_v$ is the significance index based on the annual mean differential magnitudes. The number of seasons of B observations is listed for each star. All stars were observed six seasons in V and two seasons in I. The last column is the activity index for the V filter; the B and I filters did not have the requisite three seasons of observations.

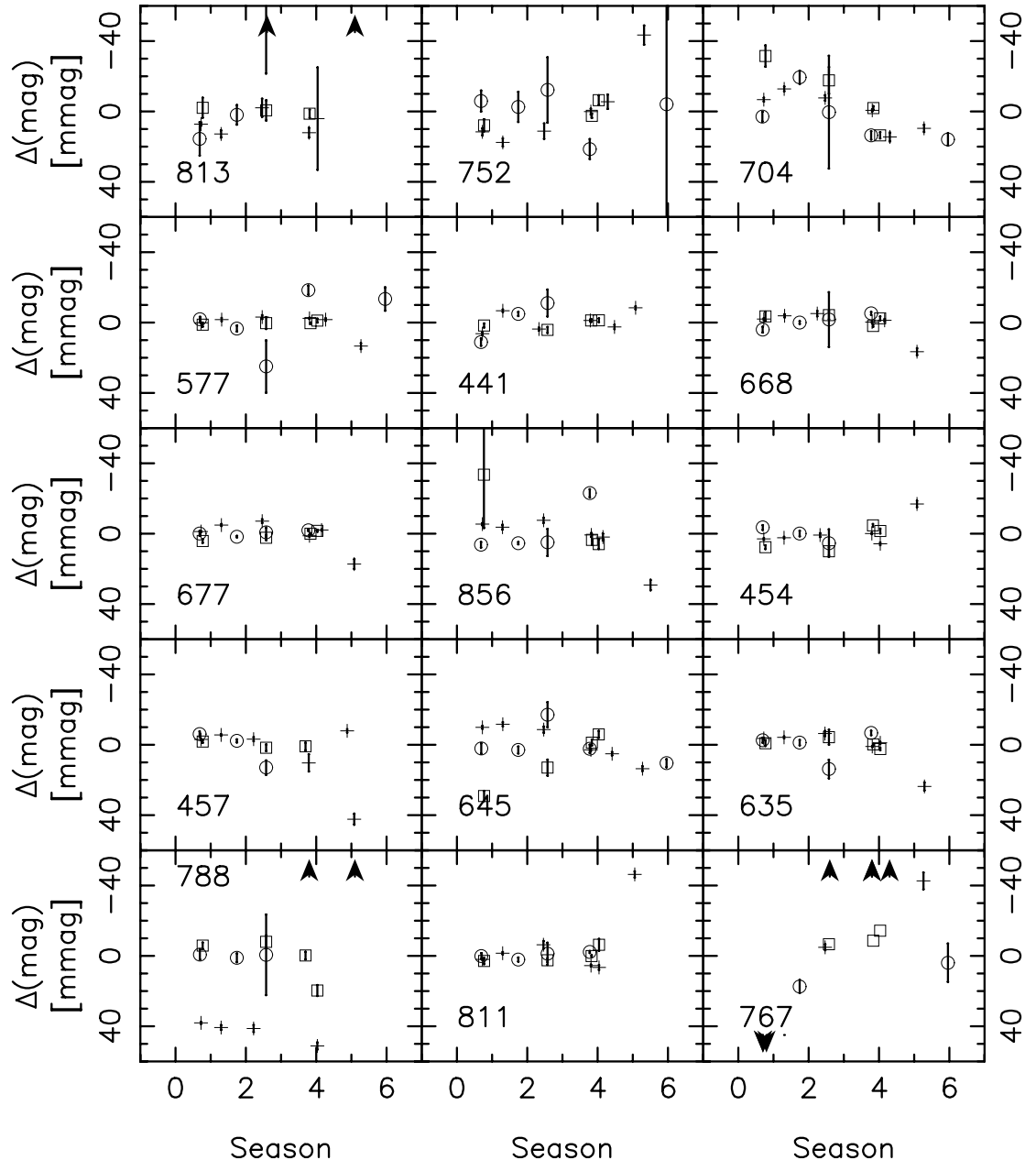


Figure 3.55: Annual mean V, B, and I differential magnitudes versus season for the fifteen candidate variable stars in NGC 188 with the largest significance indices found by analyzing the annual mean differential magnitude data and at least six seasons of observations in V. Stars are ordered by increasing significance index. Crosses represent V, circles are B, and squares are I. Error bars are also plotted. Season 0 is 1996, and thus season 6 is 2001. The stars are ordered in increasing significance index. Information about the stars can be found in Table 3.22.

| Star | V | B-V | $\alpha_v$ | $r$ | # B | # I | $A_v$ | $A_b$ | $A_i$ |
|---|---|---|---|---|---|---|---|---|---|
| 813 | 17.936 | 1.056 | 5.45 | 0.60 | 3 | 3 | 78.8 | 37.5 | 1.5 |
| 752 | 17.997 | 1.058 | 5.62 | 0.04 | 5 | 3 | 20.3 | 11.5 | 6.0 |
| 704 | 17.335 | 0.896 | 5.75 | 0.72 | 5 | 4 | 9.8 | 12.8 | 19.3 |
| 577 | 16.090 | 0.720 | 5.88 | -0.44 | 5 | 4 | 5.8 | 15.2 | 0.8 |
| 441 | 15.903 | 0.791 | 6.06 | 0.46 | 3 | 4 | 5.4 | 9.5 | 2.4 |
| 668 | 16.291 | 0.744 | 6.15 | 0.13 | 4 | 4 | 7.3 | 3.4 | 3.1 |
| 677 | 14.974 | 0.724 | 6.17 | -0.26 | 4 | 4 | 8.0 | 1.3 | 2.5 |
| 856 | 15.765 | 0.686 | 7.18 | 0.01 | 4 | 3 | 12.6 | 12.5 | 19.7 |
| 454 | 15.552 | 0.660 | 7.39 | -0.19 | 3 | 4 | 7.5 | 3.7 | 6.8 |
| 457 | 15.003 | 0.681 | 7.42 | 0.03 | 3 | 3 | 18.3 | 8.4 | 1.5 |
| 645 | 16.335 | 0.760 | 7.69 | -0.10 | 5 | 4 | 9.4 | 9.2 | 16.2 |
| 635 | 15.308 | 0.711 | 8.61 | -0.41 | 4 | 4 | 10.3 | 7.8 | 2.5 |
| 788 | 16.985 | 0.883 | 8.81 | 0.10 | 3 | 4 | 95.4 | 0.9 | 11.0 |
| 811 | 15.315 | 0.708 | 14.31 | -0.52 | 4 | 4 | 19.4 | 1.6 | 3.7 |
| 767 | 17.337 | 1.025 | 34.61 | 0.74 | 5 | 4 | 100.9 | 108.2 | 69.8 |

Table 3.22: Fifteen candidate variables in NGC 188 with the largest significance indices found by analyzing their annual mean differential data, which are plotted in Figure 3.55. $\alpha_v$ is the significance index based on the annual mean differential magnitudes, and $r$ is the correlation coefficient, which is not significance at the 99% level for any of these stars. All stars have six seasons of observations in V. Columns 6 - 7 lists the number of seasons of observations in B and I. The last three columns are the activity indices through each filter.

## 3.5 Results of Phase I

The beginning of the search for stellar activity in old open clusters is promising. The fundamental difficulty in determining which stars are active is due to the fact that both the variability of the stars due to stellar activity and the photometric errors are stochastic phenomenon. To further compound the problem, the amplitude of both the variability and the photometric errors is expected to increase with magnitude within the cluster. I believe that I have conservatively selected the stars that are variable due to stellar activity by ensuring that their photometric fluctuations are significant compared to the photometric errors and that the fluctuations in different colors are correlated at a high level. Using the activity index and correlation coefficient, which is based on two colors, I have selected stars with stellar activity on both a nightly timescale and a yearly timescale. For each of the cluster, I have separated a subset of active stars from the main sequence population. The amplitudes of variability, as well as the seasonal trends, seen in the nightly mean differential magnitude data are on the same order as the fluctuations observed in nearby stars' Ca II H and K lines by Baliunas et al. (1995). The proportion of active stars in each cluster is listed in Table 3.23. Although I have uncovered an offset error (the ensemble error) in the nightly data ranging from 2.5 - 6 mmag per star in the V data in the clusters, the correlation between colors is clearly seen when comparing V and B or I at amplitudes larger than this error. The proportion of active stars in each category is smaller for NGC 188; whether this is an age-related effect or simply due to the relatively small numbers of stars in M67 and NGC 188 is unclear.

A significant fraction of stars show the same type of color correlation in the annual mean data of six seasons. For bright stars ($V \sim 14$), I consider annual fluctuations of $\sim 1$ mmag to be significantly above the typical measurement errors. For fainter stars ($V \sim 17$), this level rises to $\sim 6$ mmag. The Sun's solar cycle variation of $\sim 1$ mmag (Frohlich & Lean 1998) falls at the detection limit. Plots of individual stars from NGC 7789 and NGC 6819 show solar-cycle-type variations that are well-matched in the BVI colors.

| Cluster | %, Nightly | #, Nightly | %, Seasonal | # Seasonal |
|---|---|---|---|---|
| NGC 7789 | 5% | 80 ± 9 | 3% | 33 ± 6 |
| NGC 6819 | 18% | 107 ± 10 | 6% | 79 ± 9 |
| M67 | 14% | 9 ± 3 | ... | ... |
| NGC 188 | 3% | 4 ± 2 | 0% | 0 |

Table 3.23: Summary of the activity of main sequence stars in the clusters for the Phase I observations. The table shows the percentage and number of active stars in each cluster on the timescale indicated.

The situation is less clear in M67 where there were few observations in B and I over this period. NGC 188 stars show very little variation on the seasonal timescale.

I have demonstrated the feasibility of studying stellar activity in open clusters. The next step will be to repeat this analysis to the BVR observations begun in late 2001. The observations strategy for Phase II has concentrated on reducing the photon noise, especially in the B filter, by taking longer exposures. An attempt was made to place the fields on the same pixels on the CCD throughout each observing run in order to minimize flat-fielding problems. The resulting reduction of errors should clarify the issues mentioned above.

## 3.6 Instrumental Limitations

The Phase I analysis has revealed approaches to maximize the signal-to-noise. The B data generally suffer from low count rates, so the Phase II observations must include longer exposures through this filter. The I data have larger than expected errors, which likely stem from unresolved flat fielding problems. Consequently, the I filter will be abandoned.

The sought-after variability is at the limit of detection. Noise levels must be kept as low as possible. In Phase II of the program, the strategy will be to emphasize longer exposures through the B filter. The R filter will also be substituted for the I filter in order to lower the noise level of the data. It will still be important to accumulate as many sky flat fields as is possible to lower the flat fielding noise. To aid in minimizing flat field

noise, an attempt will be made to place the same stars on the same pixels of the CCD throughout an observing run.